Electronic Structure Measurements Of Metal-Organic Solar Cell Dyes Using X-ray Absorption Spectroscopy

by

Phillip S. Johnson

A dissertation submitted in partial fulfillment of

the requirements for the degree of

Doctor of Philosophy

(Physics)

at the

University of Wisconsin – Madison

2014

Defended on 8 August, 2014

Dissertation approved by the following members of the Final Oral Committee:

Franz Himpsel · Professor of Physics

Mark Rzchowski · Professor of Physics

Michael Winokur · Professor of Physics

James Lawler · Professor of Physics

Padma Gopalan · Associate Professor of

Materials Science and Engineering

Abstract

The focus of this thesis is twofold: to report the results of X-ray absorption studies of metal-organic dye molecules for dye-sensitized solar cells and to provide a basic training manual on X-ray absorption spectroscopy techniques and data analysis. The purpose of our research on solar cell dyes is to work toward an understanding of the factors influencing the electronic structure of the dye: the choice of the metal, its oxidation state, ligands, and cage structure.

First we study the effect of replacing Ru in several common dye structures by Fe. First-principles calculations and X-ray absorption spectroscopy at the C 1s and N 1s edges are combined to investigate transition metal dyes in octahedral and square planar N cages. Octahedral molecules are found to have a downward shift in the N 1s-to-π^* transition energy and an upward shift in C 1s-to-π^* transition energy when Ru is replaced by Fe, explained by an extra transfer of negative charge from Fe to the N ligands compared to Ru. For the square planar molecules, the behavior is more complex because of the influence of axial ligands and oxidation state.

Next the crystal field parameters for a series of phthalocyanine and porphyrin dyes are systematically determined using density functional calculations and atomic multiplet calculations with polarization-dependent X-ray absorption spectra. The polarization dependence of the spectra provides information on orbital symmetries which ensures the determination of the crystal field parameters is unique. A uniform downward scaling of the calculated crystal field parameters by 5-30% is found to be necessary to best fit the spectra.

This work is a part of the ongoing effort to design and test new solar cell dyes. Replacing the rare metal Ru with abundant metals like Fe would be a significant advance for dye-sensitized solar cells. Understanding the effects of changing the metal centers in these dyes in terms of optical absorption, charge transfer, and electronic structure enables the systematic design of new dyes using less expensive materials.

Acknowledgments

This thesis and the degree it represents could not have been completed without the guidance, influence, and efforts of many collaborators and scientists at UW-Madison, the ALS, and the sadly departed SRC. First and foremost I must thank my advisor, Prof. Franz Himpsel, whose teaching, experience, and perhaps most of all patience were essential in my development of skills and ways of thinking, and in broadening my knowledge of fields both inside and outside of physics. I have always greatly appreciated his open door for discussion of new experiments and research topics, input on experimental and analytical difficulties, and ample feedback on my writing, and his experience in both academia and industry have been immensely useful in my decision on my career. Franz has been an exemplar for me on how to think about problems and manage working relationships and collaborations, and has been a model of what it is to be a scientist on a fundamental level. I hope that I can measure up to even a small part of the example that Franz has been for me during my tenure as his student.

I would be remiss in not acknowledging the support of the SRC and ALS staff, who were instrumental in ensuring that the limited time available for our experiments had minimal issues and in quickly solving any problems that arose. I owe thanks to Franz's previous graduate student, Peter Cook, for much of my training in the experimental and analysis techniques I use, and for continuing to be a valuable collaborator. Likewise I extend thanks to many collaborators at the ALS, San Sebastian, and in the departments of materials science and engineering and biological and chemical engineering at UW-Madison. The projects on which I have worked with them have expanded my knowledge beyond just a narrow part of the field of solar cell dyes that is presented in this thesis, and their assistance in sample preparation and complementary experiments has been invaluable. I thank also my thesis committee, Prof. Mark Rzchowski, Prof. Michael Winokur, Prof. James Lawler, and Prof.

Padma Gopalan, for their time in reviewing this thesis and the final portion of my graduate work.

I doubt I could have completed this thesis and my work as a graduate student without the support of my family and friends. My parents have been an outlet for my frustrations, doubts, and fears and have given much needed brief retreats from life in a research environment. My brother and his wife have given me support and advice from their own experiences as graduate students and postdoctoral scholars which have helped me decide on my career path and have been a reassurance for me as I worked through my time in graduate school. My friends at UW-Madison throughout my graduate career have likewise supported me and, through discussions of their own research, broadened my knowledge in various fields. In September I will take a position as a production and yield engineer at Intel in Hillsboro, Oregon, and I owe particular thanks to a friend, Tomas Hernandez, who recommended the position to me.

Contents

List of Figures

List of Tables

Chapter 1

Introduction

1.1 Motivation

The world faces a growing energy and environmental problem as the contributions to the greenhouse effect of burning fossil fuels become increasingly apparent and remaining fossil fuel resources become more expensive, environmentally damaging, and resource-intensive to exploit. The solution to this growing issue will not be a single source of energy, but a combination of multiple sources of renewable and non-renewable energy and improved energy storage and efficiency. The most prominent renewable energy technologies are biofuels, wind, tidal, and solar, with wind and solar having the two largest shares of U.S. and global investment.[1] Each of these sources is actively researched, but the fastest growing is solar energy. In particular, the U.S. Department of Energy launched the SunShot Initiative in 2011, with the aim of making solar energy cost competitive by 2020. This work focuses on a specific facet of solar energy: dye-sensitized solar cells.

The key obstacles to widespread usage of solar cells are cost, reliability, and energy storage. Reliability is a function of the construction, manufacturing, and location of the cells. The cost of solar cells comes mainly from the materials used, manufacturing process,

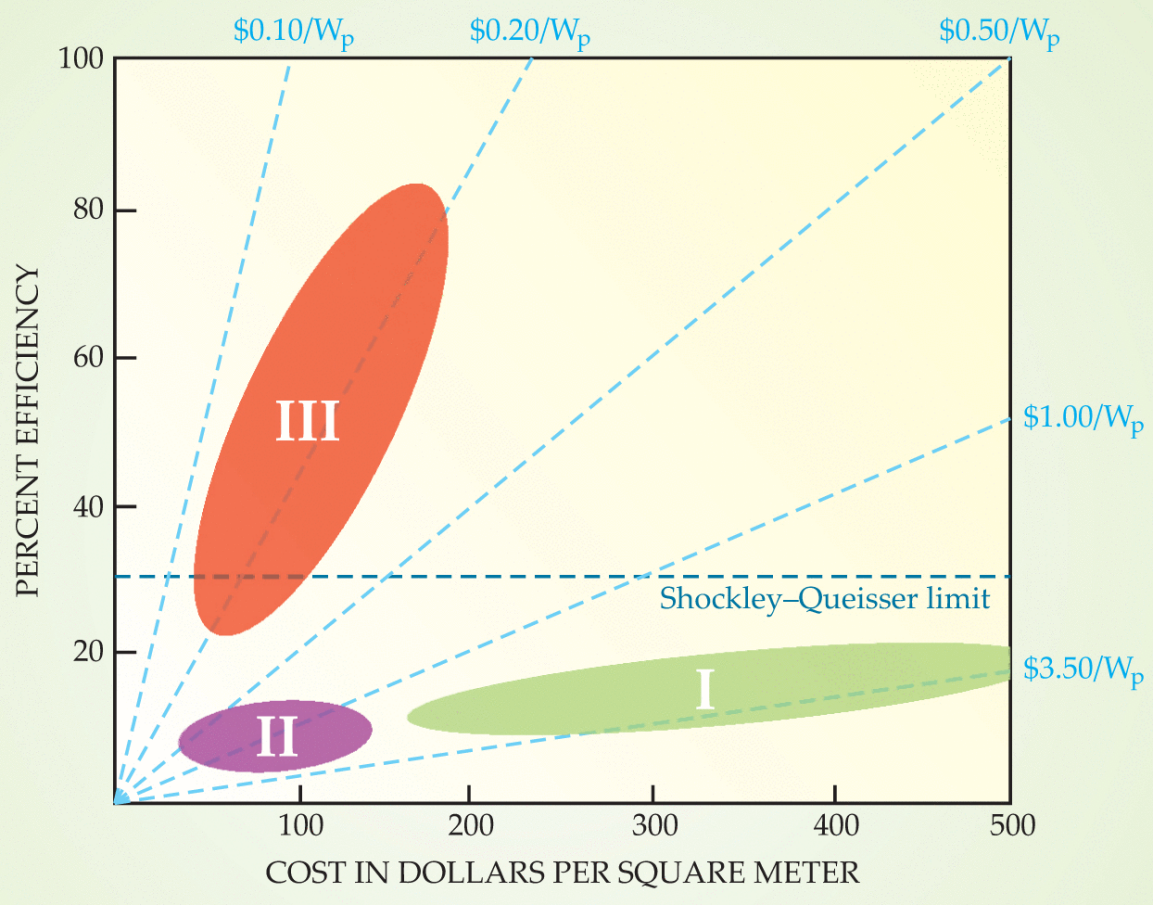

Figure 1.1: *Diagram of the cost efficiency of three generations of solar cells.*

Group I are those based on Si wafers and comprise the majority of the market. Group II includes dye-sensitized solar cells, thin film cells, amorphous Si, and other inexpensive materials. Their efficiency is currently lower than the ideal, but they are an active area of research and are recently seeing greater commercial use. The eventual goal of research on second generation solar cells is to reach group III, cells which would use inexpensive materials, but take advantage of better control over charge transfer, carrier multiplication, or multiple junction structures. Chart from Ref. [2].

and support infrastructure, which are all fundamentally linked to the cells' photoconversion efficiency.[3] Improved photoconversion efficiency is thus a primary objective in the pursuit of broad scale usage of solar cells. Improved energy storage is particularly important if solar is to become a major power source because of the need to cover the night and other low light situations, which is not an issue for current power sources. Energy storage materials and techniques are active areas of research, but will not be discussed here.

One avenue for improving the cost efficiency of solar cells is to focus on high efficiency photovoltaic materials to further increase photoconversion efficiency or reduce production cost. Since these materials typically have high material and production costs and more restrictive operating conditions, they are less suitable for widespread usage. Instead they have potential for use in applications such as utility scale solar concentrators, in which sunlight is reflected and focused from a large area onto a relatively small cell. These types of solar cells would require much more support infrastructure such as mirrors, cooling, and a large area of available land.

Another avenue is to take what is in principle the opposite approach: use materials with relatively low photoconversion efficiencies and compensate for the lower efficiency by having a much larger surface area using existing support structures, e.g., rooftop solar, greenhouse shades, and incorporating solar into large buildings. These cells would be much more cheaply produced due to using simpler prodution methods and less expensive materials such as organic dyes, carbon nanotubes, and perovskites. The primary objective in their research is increasing their efficiency while keeping their cost low. This work focuses on the electronic structure of metal-organic dyes, an established category of dyes which have yielded photoconversion efficiencies over 12%.[4]

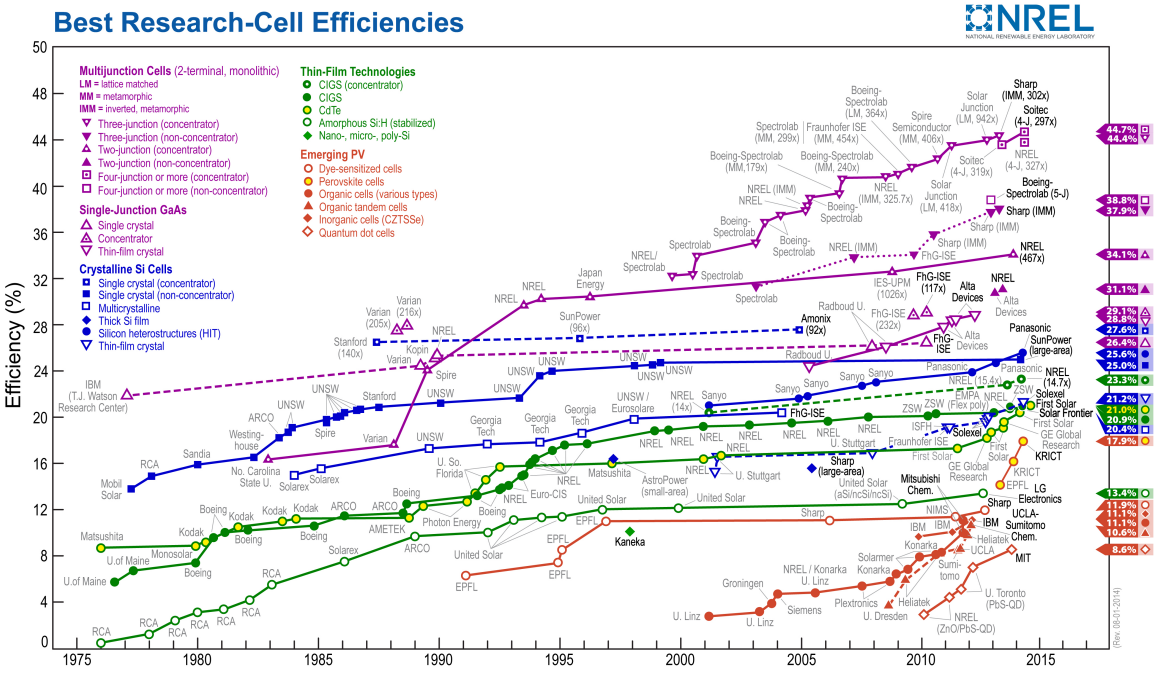

Figure 1.2: *Record research solar cell efficiencies from mid-70s to present.*

The current best cells use multijunction architecture and solar concentration to achieve such high efficiency, but are prohibitively expensive for most uses. Organic and dye-sensitized solar cells, which take the opposite approach of lower efficiency with much lower cost, have a relatively short history of development but have seen rapid improvements in efficiency during that time. Chart is updated by the National Renewable Energy Laboratory and available at http://www.nrel.gov/ncpv/

1.2 Semiconductor vs. Dye-Sensitized Solar Cells

The most common commercial solar cells currently on the market are made of mono- or polycrystalline Si, with thin film Si, CdTe, and copper indium gallium selenide (CIGS) making up a growing portion of the market. These cells have 10-20% efficiency and are typically used for rooftop power generation. However, such cells require the installation of infrastructure which limits where they can be used and constitute a large initial cost for the user. CIGS and CdTe cells additionally use materials with relatively low abundance. These factors limit the potential for current commercial solar technologies to see widespread use.

The limitations of conventional solar cells spurred interest in solar cell materials which are lightweight, easily produced, can be used with little to no modification of existing structures, and use abundant, easily synthesized materials. Dye-sensitized solar cells (DSSCs) using purely organic or metal-organic dyes with molecular structures resembling those found in nature (e.g., chlorophyll in photosystem II, hemes in hemoglobin) have emerged in recent decades as compelling choices for mass produced solar cells. DSSCs can be produced using roll-to-roll printing techniques to create thin, lightweight sheets which can be laid over windows and other surfaces where conventional solar cells are not feasible.[5, 6, 7, 8] Since little to no specialized supporting infrastructure is needed, the initial cost is much lower, and while the efficiency of DSSCs is lower by almost a factor of two due to reasons which will be discussed later, their lower cost per square foot and greater potentially usable area could compensate for their decreased efficiency. Efforts to improve the efficiency of these cells have gone in many different directions, but in this work we will focus on the electronic structure of the dye itself.

Before discussing the electronic structure of DSSCs, it is first necessary to discuss the electronic structure of a typical semiconductor solar cell (Fig. 1.3). Semiconductor solar cells possess a band gap slightly smaller than the visible portion of the solar spectrum (for example, Si has a band gap of 1.1 eV and CdTe has a nearly ideal band gap at about 1.5 eV). An absorbed photon excites an electron from the valence band to the conduction band, leaving a hole in the valence band. The electron and hole then separate to different electrodes, generating a current. If the electron and hole recombine, no current is generated. Recombination can can be caused by low carrier mobility, grain boundaries in polycrystalline or amorphous cells, and poor charge separation within the absorber. These problems can be reduced by improvements in materials, device architecture, and production techniques. The band gap of a semiconductor cell is crucial to its efficiency, as it determines the cutoff energy for the cell's absorption, which influences the quantum efficiency of the cell.

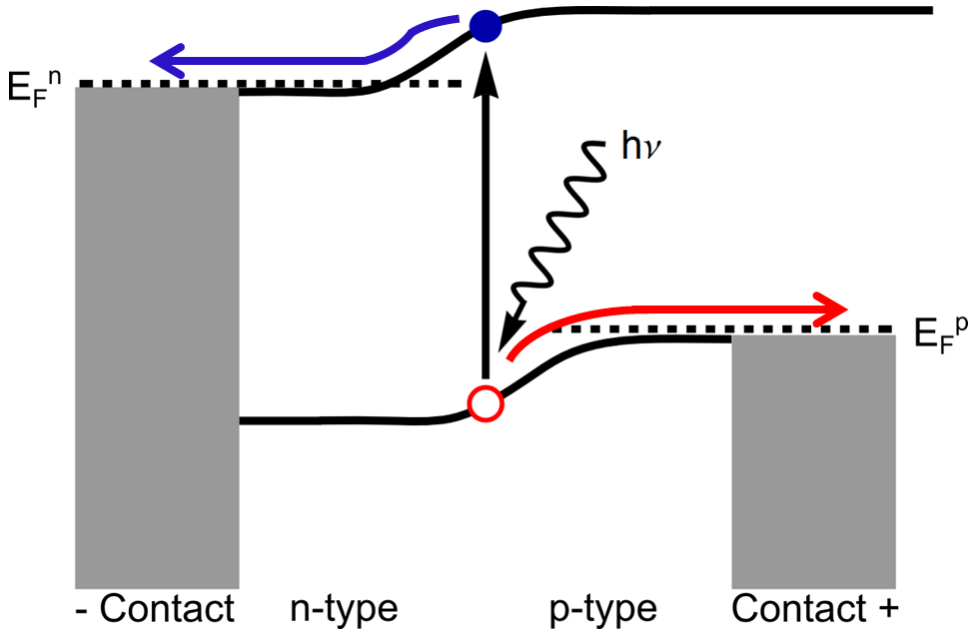

Figure 1.3: *Simplified open circuit energy level diagram of a semiconductor solar cell under illumination.*

An electron in the valence band is excited by a photon into the conduction band, leaving a hole. The electrons and holes follow the electrostatic potential of the p-n junction and build up on opposite sides of the junction. This buildup of charge creates a photovoltage at the electrodes which counteracts the junction potential until the system reaches a dynamic equilibrium. The open circuit voltage is given by $e \cdot V_{oc} = E_f^n - E_f^p$.

DSSCs (Fig. 1.4) operate in a similar way to semiconductor solar cells, however rather than using valence and conduction bands, DSSCs use the orbitals of a dye molecule, namely the highest occupied molecular orbital (HOMO) and lowest unoccupied molecular orbital (LUMO). Unlike semiconductor solar cells where the bulk of the semiconductor is also the charge transport medium, electrons and holes remain bound to an isolated dye molecule in a DSSC after separation. To avoid recombination, the electrons and holes must be separately removed from the absorber, which requires a donor to fill the hole in the HOMO and an acceptor to remove the excited electron in the LUMO. The donor and acceptor thus add another two energy levels which must be considered in the design of the cell: the LUMO or conduction band minimum (CBM) of the acceptor and the HOMO or valence band maximum

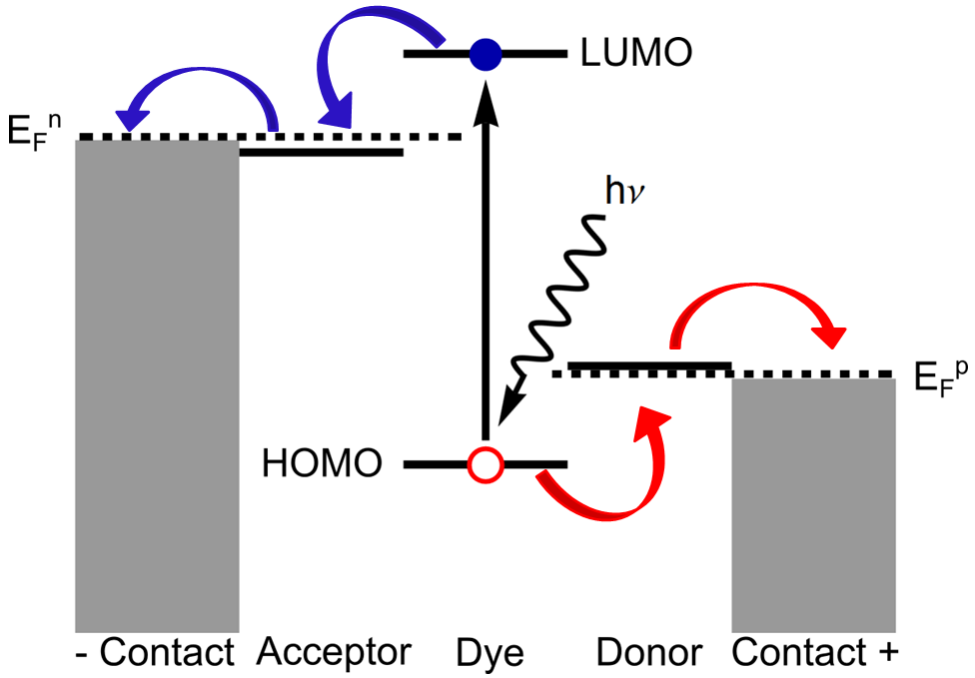

Figure 1.4: *Simplified energy level diagram of a dye-sensitized solar cell.*

While semiconductor solar cells have conduction and valence bands with the band gap determining the UV-visible absorption of the cell, DSSCs' absorption is determined by the HOMO-LUMO gap of the dye molecule. Additionally, while a semiconductor acts as both the absorber and charge transport medium, a dye can act only as an absorber. Acceptor and donor molecules are required to transport the electrons and holes away from the dye before they recombine. As with semiconductor solar cells, the open circuit voltage is given by $e \cdot V_{oc} = E_f^n - E_f^p$. This figure is shown for doping higher than the semiconductor to metal transition in the acceptor and donor (typically $> 10^{20}$ cm^{-3}).

(VBM) of the donor.

Efficient electron transfer from the dye to the acceptor (and hole transfer from the dye to the donor) requires a relatively large energy difference between both the dye LUMO and acceptor and the dye HOMO and donor. A larger energy difference reduces electron-hole recombination because charge transfer will occur more quickly, thus increasing photocurrent. However, this increased photocurrent comes at the cost of reduced photovoltage and thus reduced power generation. Conversely, a high photovoltage comes at the cost of reduced photocurrent. The choice of dye, donor, and acceptor is then a problem of optimizing their

energy levels to maximize both photovoltage and photocurrent, which requires knowledge of the electronic structure of each part of the cell. These insights can be gained from X-ray absorption spectroscopy.

1.3 Previous Work on Common Solar Cell Dyes

Polypyridyl-Based Dyes

Polypyridyl-based dyes with transition metal centers have a long history of development, including some of the most widely known dyes being modifications of a tris(bipyridine) structure. In a seminal 1991 paper by O'Regan and Grätzel [9], a trimeric ruthenium complex with bipyridine ligands was deposited on a TiO_2 nanoparticle substrate to achieve a higher efficiency than previous attempts to use dye-sensitized solar cells. One of the most efficient dyes currently in use is the dye molecule N3, which is similar to Ru^{2+}tris(bipyridine), but with one of the bipyridines replaced by two isothiocyanato (-NCS) groups. The N3 molecules bond to the TiO_2 substrate via carboxylic acid groups on the bipyridine ligands, which allows transfer of excited electrons from the ligands to the acceptor. A number of modifications on the basic design of N3 dye exist which change the attachment groups, but the Ru^{2+} ion and its nearest neighbors are typically kept the same.

While N3 dye and similar molecules have the potential issue of using relatively low abundance Ru, polypyridyl-based molecules using other, more abundant transition metals are seeing potential use in solar cells in capacities other than as the absorber. For example, tris(bipyridine) molecules with transition metal centers tend to have useful redox properties. In particular, $Co^{2+/3+}$tris(bipyridyl) complexes have higher reduction potentials which could make them an option for replacing the corrosive iodide/triiodide electrolyte that has been commonly used as a donor.[4, 10, 11, 12] Other potential electrolytes are metallic redox complexes [13, 14, 15, 16, 17] and organic hole conductors.[18, 19, 20, 21]

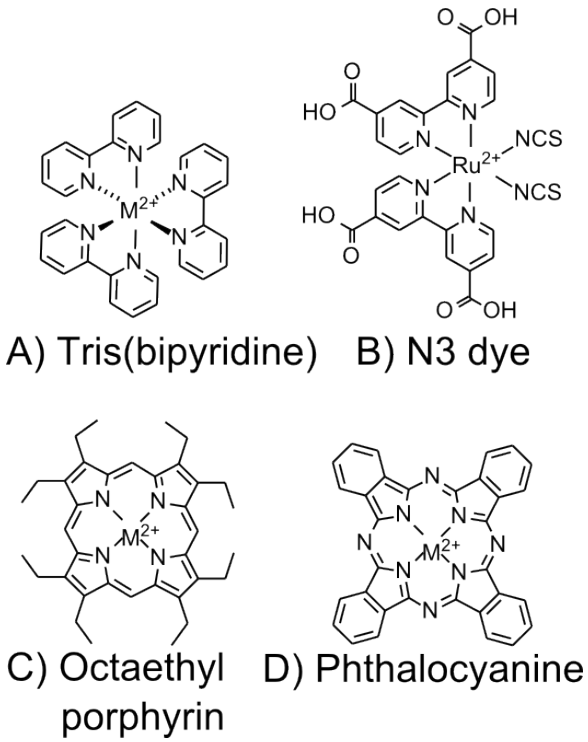

Figure 1.5: *Molecular structures of common solar cell dyes.*

A) The basic structure of tris(bipyridine) molecules with transition metal ion centers are a foundation for many solar cell dyes with reltively high efficiency. B) N3 dye is a modification of the tris(bipyridine) structure and is currently one of the most efficient sensitizers. C) Porphyrins with transition metal ion centers are commonly found in nature, and modified porphyrins have received much attention recently for higher efficiency solar cells. D) Phthalocyanines have a similar central structure to porphyrins, but are stable at higher temperatures and have different electronic structure.

Porphyrins and Phthalocyanines

Much of recent solar cell dye research and development has begun to focus on phthalocyanines and porphyrins with transition metal centers. Transition metal phthalocyanines and porphyrins are heteorcylic molecules with 4 N atoms bonded to the metal ion in the center. Compared to porphyrins, phthalocyanines have additional N atoms in the ring surrounding the metal and additional aromatic rings on their corners, giving them increased temperature stability. These molecules are convenient choices for solar cell dyes because they have a simi-

lar structure to many molecules found commonly in nature, in particular in heme (which has a porphyrin with an Fe^{2+} center) and chlorophyll (which has a porphyrin with an Mg^{2+} center). Additionally, they are a well known, stable set of dyes with a relatively simple synthesis process and energy levels strongly dependent on their transition metal center.[22, 23] While porphyrin-based dye molecules have long had efficiencies <10%, in recent years new molecule designs have been developed which have efficiencies over 12%.[4] These new molecules keep the porphyrin ring intact, but add ligands which retard recombination and enhance charge transfer.

The dominant transition in porphyrins and phthalocyanines when exposed to light is a metal to ligand charge transfer (MLCT) in which a valence electron from the metal ion delocalizes over the N cage surrounding the metal. Assuming the electron and hole do not recombine, the electron is then removed from the ring by a linker to the acceptor and the hole in the metal ion filled by the donor. Other transitions at about the same energy also involve the π system in the N cage, such as π-π^* transitions and ligand to metal charge transfer, whose excitation strength is dependent on the degree to which the metal and ligand wave functions are mixed.[24]

Excluding the porphyrins and phthalocyanines whose metal ions have full or nearly full d shells, the orbital ordering and electronic structure of these molecules is not well understood. This is particularly true when the metal ion is Fe^{2+}, which has a number of possible spin states. The electronic structure of the metal ion is further complicated by the square planar symmetry of the surrounding molecule, which splits the d levels into five different levels (two of which are degenerate) that are then further split into a large manifold by electron-electron interactions. These difficulties will be discussed further in Chapter 4.

1.4 Scope of the Thesis

This work discusses X-ray absorption measurements performed on multiple solar cell dyes in order to better understand their electronic structure and the effects of systematically changing the transition metal in each dye. In particular the effects of replacing Ru by Fe in polypyridyl complexes and porphyrins and the differences in the crystal fields among Fe, Co, and Ni porphyrins and phthalocyanines will be covered. Knowledge of the effects of the transition metal and the surrounding molecular structure on the energy levels of the dye molecule is important for design of future sensitizers such as donor-π-acceptor complexes. The ultimate goal is to design solar cell sensitizers from the ground up to have specific properties.

Chapter 2

Experimental Techniques

2.1 X-ray Absorption Spectroscopy

Introduction to X-ray Absorption Spectroscopy

X-ray absorption spectroscopy (XAS) determines the unoccupied electronic structure of molecules or crystals in the presence of a core hole. Absorption of X-rays of order 100-1000 eV excites an electron from a core level (commonly 1s or 2p) into an unoccupied orbital or band. These transitions occur at specific, distinct energies, which makes the technique element and bond selective. Additionally, XAS allows for simultaneous independent measurements of the surface and bulk of a given sample through electron yield and fluorescence yield, respectively. Figure 2.1 compares XAS to other common electronic spectroscopy techniques, ultraviolet and X-ray photoelectron spectroscopy and UV-vis spectroscopy.

Figure 2.2 shows the basic processes which occur in XAS. A photon excites an electron from a core level (typically 1s or 2p) to an unoccupied state, leaving a hole in the core. The core hole can be filled in one of two ways: an electron in an occupied state can drop into the hole while electrons are emitted from the atom, or an electron can drop into the hole and emit a photon. The former process is detected in electron yield measurements and the latter

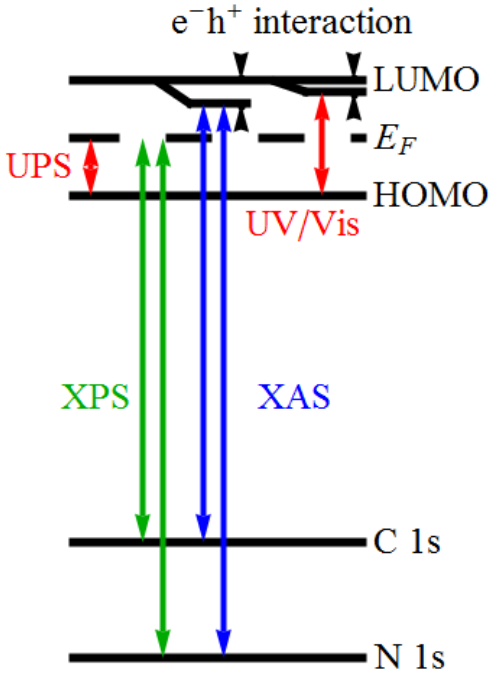

Figure 2.1: *Comparison of transitions in UPS, XPS, XAS, and UV-vis spectroscopies.*

While the photoelectron spectroscopies provide information on the binding energies of valence and core levels and UV-vis spectroscopy gives information on band or HOMO-LUMO gaps, X-ray absorption spectroscopy provides information on unoccupied energy levels. Since the transitions are from a well-defined core level, the unoccupied energy levels can be determined unambiguously, unlike in UV-vis spectroscopy, which might have many degenerate transitions. The creation of a core hole reduces the transition energy slightly due to the electron-hole interaction.

in fluorescence or photon yield measurements. The most important distinction between total electron yield (TEY) and fluorescence yield (FY) measurements is that electron yield measurements are sensitive to the surface of a sample while fluorescence yield measurements are sensitive to the bulk of the sample. This distinction comes about because of the differences in escape depth between electrons and photons.

While photons in the soft X-ray region have penetration depths of up to several μm, electrons have an escape depth of only a few nanometers, which limits electron yield measurements to the first few layers of a sample. Photons however have an escape depth on the

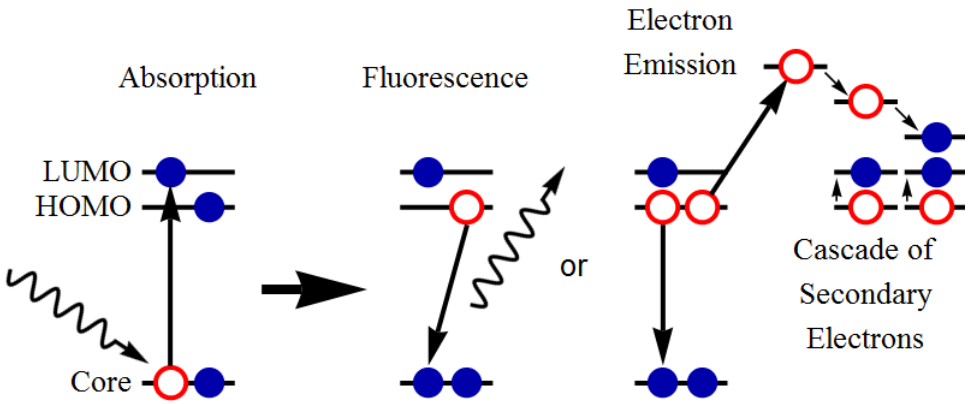

Figure 2.2: *X-ray absorption and fluorescence or electron emission processes.*

After absorbing an X-ray, a core level electron is excited into an unoccupied state. The resulting core hole is then quickly filled by another electron, releasing either a photon (fluorescence) or causing emission of a cascade of lower energy electrons.

order of 100 nm, which means that the majority of the fluorescence yield signal comes from deep in the sample instead of the surface.[25] Fluorescence emission is however much less common than electron emission by a factor of $\sim$ 100-1000 for low Z elements since many electrons can come from one excitation due to inelastic scattering while fluorescence yields only a single photon.[25] Fluorescence detection does however have the benefit of avoiding issues with the surface of an insulating sample charging, which can negatively affect electron yield measurements.

Figure 2.3 shows series of both TEY and FY spectra taken simultaneously for a sample of an organic molecule that is damaged by radiation during measurement. A set of sharp peaks indicating evolution of N_2 trapped in the bulk of the sample as a result of radiation damage processes is visible in the FY spectra but absent in the TEY spectra since any N_2 near the surface would escape into vacuum. Measurement of the bulk properties of the materials in this work is less relevant than measurement of the surface properties since samples are, when possible, thin films, and practical applications for these dye molecules would in principle

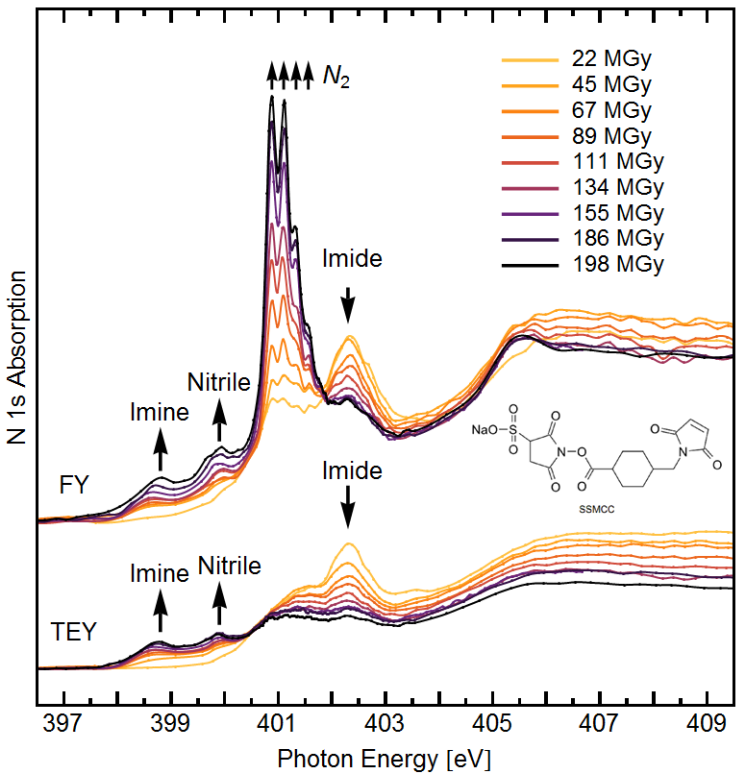

Figure 2.3: *Comparison of TEY (surface sensitive) and FY (bulk sensitive) measurements taken simultaneously.*

The bulk-sensitive FY spectra of SSMCC reveal generation of N_2 during irradiation, which is trapped in voids below the surface. In the simultaneous surface-sensitive TEY spectra, on the other hand, N_2 is not visible because it will desorb into vacuum.[26] The two complementary detection methods reveal differences in orientation, oxidation state, or sample composition between the surface of a sample and the bulk.

involve at most a few monolayers of the absorber molecules on the surface of nanoparticles or nanorods of TiO_2 or another acceptor material. Additionally, no significant differences were found between the TEY and FY spectra in this work when such measurements were possible, so all spectra are, unless stated otherwise, taken in TEY detection mode.

X-ray absorption spectroscopy is used in this work because it is a powerful tool for determining the electronic structure of dye molecules. UV-visible spectroscopy is of course directly relevant to the transitions that occur in normal solar cell operation, but it does not

reveal any information about electronic structure. In fact many different types of transitions (e.g., MLCT, LMCT, and π-π^* transitions) in different parts of the molecule occur at similar energies, which complicates identification of energy levels. X-ray absorption spectroscopy is, however, element- and bond-selective because it uses transitions from atomic core levels into unoccupied orbitals. This selectivity removes the complication of competing transitions. Additionally, XAS is polarization-dependent because the transitions studied are dipole transitions. The polarization dependence of the spectra is useful for determining the orientation of molecules on a surface and in particular can be used to identify the symmetry of transitions into d levels, which will be discussed further in Chapter 4.

X-ray absorption spectroscopy requires a tunable, high intensity X-ray source such as an undulator beamline at a synchrotron. The measurements in this work were performed on the U2 VLS-PGM at the Synchrotron Radiation Center and at the Bio-NEXAFS end station on Beamline 8.0 at the Advanced Light Source at Lawrence Berkeley National Laboratory.

Elements of X-ray Absorption Spectra

The transitions from core level to unoccupied orbitals are the focus of XAS, but are not the only transitions present in the spectra. The background of any given spectrum is composed of transitions from valence or other higher-lying energy levels into vacuum/continuum states. The background from valence excitations is flat below the lowest soft X-ray transition (often the C 1s edge) in the sample and so does not interfere with the spectra to a significant degree. However, once above the lowest edge the background includes the contributions from excitations of those core electrons into vacuum or continuum states, which are frequently several times stronger than the pre-edge background. The same addition occurs at each successive edge. Over the next $\sim$ 100 eV the post-edge region will return to being flat, but will provide a much greater background for the next edge than was present for the lower absorption edge. Figure 2.4 is a cartoon showing the changes from one absorption edge to

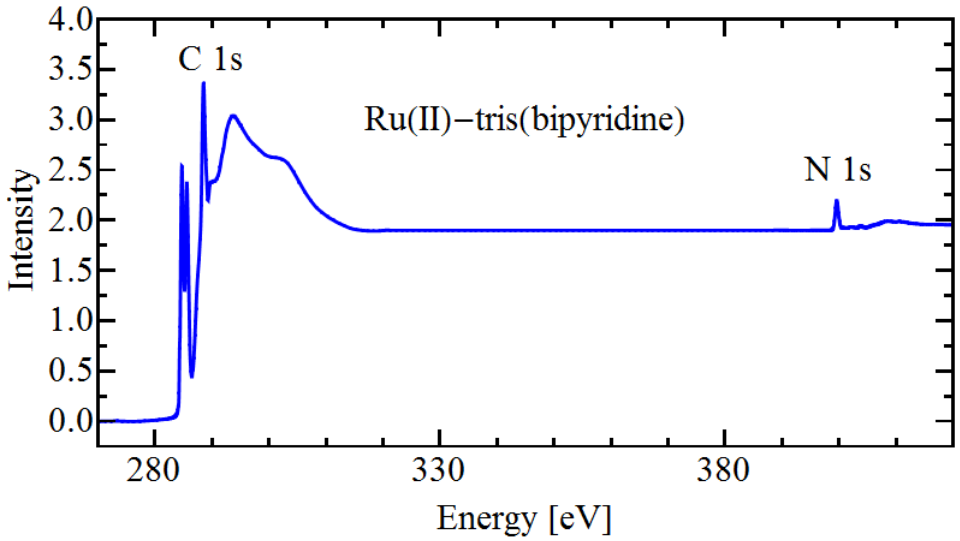

Figure 2.4: *Extended spectrum of a transition metal dye.*

Valence excitations make up the background below the C 1s region, which has features many times greater than the finite pre-edge background (the substrate also contributes to the background if the film is not continuous). Above the C 1s region the spectrum levels off to a new background which contains the valence excitations as well as electrons excited out of the C 1s core level. The N 1s region sits on this much larger background, so that its features are much smaller relative to the background than the C 1s region's features were to its pre-edge background. This full spectrum covering both absorption edges would span ~ 150 eV, so it is rarely useful to take an extended spectrum covering more than one absorption edge.

the next.

This trend is particularly noticeable when moving from the C 1s edge to the higher N 1s edge (energy ranges for common absorption edges and those in this work can be found in Table 2.1). The C 1s edge usually has signal several times greater than the background on which it sits, largely due to carbon's prevalence in organic molecules. The N 1s edge sits on this background, but due to the very low abundance of N relative to C in organic molecules, the N 1s signal is generally only a few percent above the background. The relatively low signal of the N 1s edge also makes the spectra much more susceptible to drifts in the C 1s background. Very thin samples are especially vulnerable to background instabilities because

Absorption Edge	Energy Range (eV)
C 1s	280-320
N 1s	390-420
O 1s	525-555
Mn 2p	630-660
Fe 2p	695-735
Co 2p	770-805
Ni 2p	840-870

Table 2.1: Energy ranges for common absorption edges.

of their lower signal compared to thick samples.

It should be noted that many factors influence the height of peaks X-ray absorption spectra, particularly the shape and energy density of the final state orbitals (see Section 2.2 for the equations and quantities governing the X-ray absorption cross section). One should thus not generally expect that transitions into two different orbitals, even if they are near in energy, would have a 1:1 correspondence between them. For example, transitions from the N 1s core level into the nitrile π^* orbitals (after their degeneracy is broken by a nearby π system) have very different intensities despite a separation of <1 eV between the peaks (see Fig. 6c in Ref. [27]). Likewise one should not expect a peak corresponding to a transition into an imine π^* orbital to have the same characteristics as a transition into an amide π^* orbital or a nitrile π^* orbital.

Figure 2.5 shows a typical N 1s NEXAFS spectrum with its major components labeled. The region at lower energy than the first transition peak is called the pre-edge region. This region contains the background from valence transitions and lower energy core level transitions and is in most cases flat. The lowest energy peaks in a spectrum correspond to transitions into π^* orbitals (provided π bonds are present in the molecule). These peaks are commonly very sharp (FWHM of $\sim$ 1 eV) and exhibit strong polarization because they are highly directional, making them usually the best choice for determining the orientation of molecules on a surface. Each peak belongs to a different π^* orbital, and they are narrow

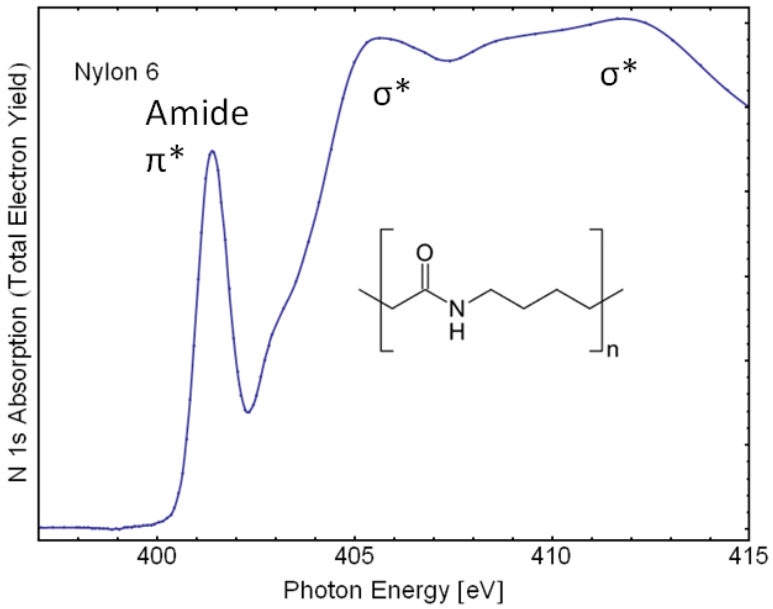

Figure 2.5: *Example N 1s absorption spectrum of a polymer.*

X-ray absorption spectra can be divided generally into three regions, from low to high photon energy: the π^* region, σ^* region, and the step edge containing continuum excitations. The excitations into the continuum cut off here because it is typically featureless. Transitions into π^* orbitals occur at the lowest photon energies in a spectrum, and they produce sharp, intense intense peaks that are often well-separated in energy, which are useful properties. The σ^* region at higher energy consists of broader peaks which sit on the background leading into the step-edge, which makes them more difficult to isolate.

enough that energy differences as small as a few tenths of an eV due to different orbital symmetries or binding energies can be detected.

Above the π^* region is the onset of σ^* peaks and the continuum excitations. The σ^* peaks are typically very broad (FWHM of several eV) and have significant overlap, and since they sit on top of the broad step function produced by continuum excitations are significantly more difficult to isolate compared to the π^* peaks. While they also show polarization dependence like π^* orbitals, their width and the greater spatial extent of σ^* orbitals makes them less useful for determining molecular orientations. In some cases, e.g., C-H bonds, the core-to-σ^* transitions can be sharp and of similar energy to π^* transitions. It should be noted also

that there is in many cases not a well defined boundary between the π^* and σ^* regions, and that the two regions may overlap.

Above the σ^* region the spectrum flattens out again, as photon energies are high enough that no more bound states remain and core electrons are simply emitted from the atoms. This portion of the spectrum is called the post-edge region or continuum step. Since excitations into the continuum are independent of the polarization of the incoming X-rays, it is useful to normalize spectra at the post-edge, which will be discussed in Section 2.5. It is common to extend a spectrum well above the σ^* region to ensure that the continuum step flattens out for normalization purposes.

An additional complication in the spectra arises when the core level is changed from an s to a p level, that of the spin-orbit splitting of p levels into $p_{3/2}$ and $p_{1/2}$ components with different binding energies. Electrons in both levels can undergo transitions into the same orbitals, but the transitions will be separated by the difference in binding energy between the two levels. Since the binding energy of electrons in the $p_{3/2}$ level is lower than those in the $p_{1/2}$ level, transitions from the $p_{3/2}$ level into unoccupied orbitals occur at a lower photon energy than transitions from the $p_{1/2}$ level. Additionally, since twice as many electrons are in the $p_{3/2}$ level as are in the $p_{1/2}$ level, the peaks corresponding to transitions of $p_{3/2}$ electrons are about twice as intense as those for $p_{1/2}$ electrons.

In cases where the binding energy difference is small enough that the $p_{3/2}$ and $p_{1/2}$ regions of the spectrum overlap (common among lower Z elements than the 3d transition metals), the $p_{1/2}$ contribution must be removed. The basis of this process is given in Ref. [28]. Fortunately, for the molecules and edges in this work, the difference in binding energies between $2p_{3/2}$ and $2p_{1/2}$ is sufficiently large that the two regions do not overlap. The binding energies for the $2p_{3/2}$ and $2p_{1/2}$ levels relevant to this work are given in Table 2.2 (binding energies are from [29]). Since the $2p_{3/2}$ and $2p_{1/2}$ regions in 3d transition metals are well separated, and the $2p_{1/2}$ region has both lower intensity and resolution, this work focuses

Transition Metal	$2p_{3/2}$	$2p_{1/2}$
Mn	638.7	649.9
Fe	706.8	719.9
Co	778.1	793.2
Ni	852.7	870.0

Table 2.2: $2p_{3/2}$ and $2p_{1/2}$ binding energies for elements in this work. Binding energies are from [29].

only on the $2p_{3/2}$ region.

2.2 Theory of Core Level Excitation Spectra

A thorough treatment of the theory of core level excitation spectra is given in *NEXAFS Spectroscopy* by J. Stöhr [25] and *Core Level Spectroscopy of Solids* by F. de Groot and A. Kotani.[30] In this work only a brief summary of the theory related to the transition matrix elements, the intensity and width of transitions, and their polarization dependence will be given.

X-ray Absorption Cross-section

The X-ray absorption cross-section is calculated from Fermi's "Golden Rule" for a transition from an initial state i to final state f consisting of a photoelectron with energy ϵ and an ion in state j [31],

$$\sigma_{ij}(\epsilon) = \frac{4\pi^2 \alpha a_0^2}{3g_i}(\epsilon + I_{ij})\,|M_{if}|^2 \tag{2.1}$$

where α is the fine structure constant ($\sim 1/137$), a_0 is the Bohr radius (5.29×10^{-9}cm), g_i is the degeneracy of the initial state, and I_{ij} is the ionization energy in Rydbergs. The matrix element M_{if} is given by

$$|M_{if}|^2 = \frac{4}{(\epsilon + I_{ij})^2} \sum_{i,f} |\langle f| \sum_{\mu} \exp(i\boldsymbol{k}_\nu \cdot \boldsymbol{r}_\mu)\, \nabla_\mu |i\rangle|^2 \tag{2.2}$$

For photon energies on the order of hundreds of eV, the exponential term in 2.2 can be reduced to the dipole approximation

$$\exp\left(i\boldsymbol{k}_\nu \cdot \boldsymbol{r}_\mu\right) = 1 + i\boldsymbol{k}_\nu \cdot \boldsymbol{r}_\mu \tag{2.3}$$

Since the second term is imaginary only the unity term is relevant, so the dipole approximation reduces 2.2 to the following [31]:

$$|M_{if}|^2 = \frac{4}{\left(\epsilon + I_{ij}\right)^2} \sum_{i,f} |\langle f| \sum_\mu \nabla_\mu |i\rangle|^2 = \sum_{i,f} |\langle f| \sum_\mu \boldsymbol{r}_\mu |i\rangle|^2 \tag{2.4}$$

Polarization Dependence

In most cases, however, the full description of the X-ray absorption cross section is not needed for interpreting spectra, particularly when studying the polarization dependence of a transition. Instead just the dependence of the transition intensity on the dipole matrix element is sufficient:

$$I_{if} \;\propto\; |\langle f|\boldsymbol{A}\left(\boldsymbol{r}\right) \cdot \boldsymbol{p}|i\rangle|^2 \tag{2.5}$$

This proportionality involves the polarization of the incident X-rays and the symmetry of the initial and final states. For the common case where the initial state is an s level, 2.5 reduces to simply

$$I_{if} \;\propto\; cos^2\delta \tag{2.6}$$

where δ is the angle between the electric field vector of the incident X-rays and the orbital vector of the final state.[25] It is not possible to know δ without prior knowledge of the orientation of the molecules. However, if one assumes that over a large sampling area there are many domains with random azimuthal orientation but consistent polar tilt, the dependence on δ can be transformed into a dependence on θ, the incident angle of the X-rays, and α, the polar tilt angle of the final state orbital.

The relationship in 2.6 illustrates the usefulness of 1s core level spectra for identifying the orientation of molecules on a surface. Because the s core level is spherically symmetric, only

the final state orbital vector and electric field vector determine the intensity of the transition. In the case of an s initial state, the final state will be a p-like orbital, typically a π^* orbital, which are well-defined and yield sharp, distinct peaks in the spectra. In aromatic molecules such as pyridine,[32] thiophene,[33] or phthalocyanines,[22] the π^* orbitals are orthogonal to the molecular plane, so for example maximum intensity for the transition to the π^* orbital occurring at normal incidence indicates that the molecules stand on edge on the surface.

Electron and Fluorescence Yields

An important quantity to consider in X-ray absorption spectroscopy is the mean free path of the incident photons, as it is one factor which influences how much signal comes from the adsorbate vs. from the substrate. The photon mean free path is the inverse of the X-ray absorption coefficient $\mu_x(h\nu)$, which is related to the X-ray absorption cross-section and is given by

$$\mu_x(h\nu) = n_v \sigma_x(h\nu) \tag{2.7}$$

where n_v is the volume density of the adsorbate.[25] Values for both the absorption cross sections and coefficients for common materials have been compiled in Refs. [34] and [35]. The mean free path of the incident photons is many orders of magnitude longer than those of the photoelectrons generated by the excitations, but inelastic scattering processes can generate a large number of lower energy secondary electrons which can escape the surface, increasing the effective escape depth of electrons to many times the mean free path of a single photoelectron. Typical effective escape depths are on the order of 1-10 nm and tend to be longer in insulators than metals or semiconductors.[25, 36]

Assuming a thick sample, the absorption coefficient in 2.7 will depend on the X-ray incidence angle θ (measured from the surface) according to

$$\mu_x(\theta, h\nu) = \frac{\mu_x(h\nu)}{sin\theta} \tag{2.8}$$

This modification then allows for the calculation of the number of photoelectrons created at a depth z within interval dz

$$N_e = I_0 A_0 \mu_x (\theta, h\nu) \, \mathrm{e}^{-\mu_x(\theta,h\nu)z} dz \tag{2.9}$$

where I_0 is the incident photon flux density and A_0 is the area exposed to the beam. The number of photoelectrons in 2.9 contributes a fraction dI_t of the TEY given by

$$dI_t = \frac{\Omega}{4\pi} N_e \mathrm{e}^{-z/L} h\nu M \tag{2.10}$$

where Ω is the solid angle into which the electrons are emitted, L is the effective electron escape depth (i.e., the effective electron scattering length projected onto the surface normal), and $h\nu M$ is a total gain function that accounts for the additional secondary electrons created by inelastic scattering processes with M being a material constant for conversion efficiency into low-energy electrons.[25] Assuming a thick sample, integrating 2.10 over the sample thickness gives

$$I_t (\theta, h\nu) = \frac{\Omega}{4\pi} I_0 A_0 \frac{\mu_x (\theta, h\nu)}{\mu_x (\theta, h\nu) + 1/L} h\nu M \tag{2.11}$$

The above equations approximate the TEY for thick samples where the influence of the substrate is minimal. For samples a few monolayers at most, the substrate contributions to the TEY can no longer be ignored. However, since this work does not use such thin samples, the case of monolayer samples will not be covered here.

Fluorescence yield is somewhat easier to describe due to the lack of inelastic scattering interactions for fluorescent photons, but the longer mean free path of fluorescent photons means that an adsorbate layer must be much thicker to avoid substrate contributions to the FY. Assuming a sufficiently thick sample ($>$ 100 nm) that substrate contributions to the FY are negligible. In this case a sufficiently thick sample is again assumed, so by a similar derivation as for the TEY, we have

$$dI_f = \frac{\Omega}{4\pi} I_0 A_0 \mu_x (\theta, h\nu) \, \omega_f \mathrm{e}^{-\mu_x(\theta,h\nu)z} \mathrm{e}^{-z/D\left(\epsilon_f\right)} dz \tag{2.12}$$

where ω_f is the strongest component of the FY with energy ϵ_f, and $D(\epsilon_f)$ is the effective X-ray escape depth at energy ϵ_f, measured along the surface normal. $D(\epsilon_f)$ is related to the X-ray absorption coefficient by $D(\epsilon_f) = cos\delta/\mu_x(\epsilon_f)$ where δ is the detection angle from the surface normal.[25]

Integrating 2.12 over the sample thickness yields

$$I_f(\theta, h\nu) = \frac{\Omega}{4\pi} I_0 A_0 \frac{\mu_x(\theta, h\nu)\,\omega_f}{\mu_x(\theta, h\nu) + 1/D(\epsilon_f)} \tag{2.13}$$

which parallels 2.11 without the gain factor $h\nu M$ which accounts for generation of additional secondary electrons, as those inelastic scattering process are negligible for FY. In the case of a sample thin enough that the substrate's contribution to the FY signal cannot be neglected, the adsorbate signal will sit on a large background coming mostly from the substrate FY. In such a case 2.13 will describe the FY from the substrate, and the FY from the thin adsorbate layer will be given by

$$I_f(h\nu) = \frac{\Omega}{4\pi} I_0 A_0 \omega_x(h\nu)\,\rho\omega_f \tag{2.14}$$

which is typically many orders of magnitude smaller than the other background contributions.[25] Without some means of suppressing the background (e.g., by means of filters, special detectors, or monochromators), FY detection is impractical for thin samples. Al filters for example are commonly used with microchannel plate detectors to assist FY detection.

2.3 Ultrahigh Vacuum System and Measurement Apparatus

The photon energies in X-ray absorption measurements are typically in the 100-2000 eV range. These energies are sufficient to ionize molecules in air and thus have very short mean free paths. X-ray absorption measurements must then be performed in ultrahigh vacuum (UHV) conditions to maintain high photon flux over the length of a beamline, which is

typically tens of meters. Exact operating pressures are largely determined by the synchrotron ring's operating pressure (low 10^{-10} to 10^{-11} torr), but depending on the distance from the ring and amount of differential pumping present, adequate chamber pressures can be up to the high 10^{-9} torr region. Specially constructed cells with very thin windows are capable of sustaining large pressure differences, which allow for measurements of gaseous or liquid media, though these will not be discussed here.

All measurements in this work were performed in UHV conditions, typically $<10^{-9}$ torr. This pressure was maintained during measurements by an ion pump and titanium sublimation pump (TSP). A load lock for sample introduction and a crucible for *in situ* evaporation are kept under vacuum by a turbopump that is typically isolated from the measurement chamber.

Fig. 2.6 is a simple schematic of the measurement apparatus. Samples are mounted on a manipulator with 5 degrees of freedom (x, y, and z motion with polar and azimuthal rotation), which is connected to a picoammeter. A Cu ring held at a +500 V bias potential is a few centimeters upstream of the manipulator to increase the electron yield from the sample. Upstream of the Cu ring is a Ni mesh which has been coated *in situ* with Au which intercepts $\sim 10\%$ of the incoming photons and is connected to a second picoammeter. The Au mesh is used to correct for changes in photon flux due to fluctuations in the beam or grating transmission because Au has no transitions at the relevant energies in this work. The mesh also has a ring less than 1 cm in upstream of it which is held at a +45 V bias potential to increase its electron yield. Further upstream of the Au-coated mesh is a Ni mesh of similar design which is used for energy calibration purposes. Microchannel plates mounted near the sample detect fluorescent photons.

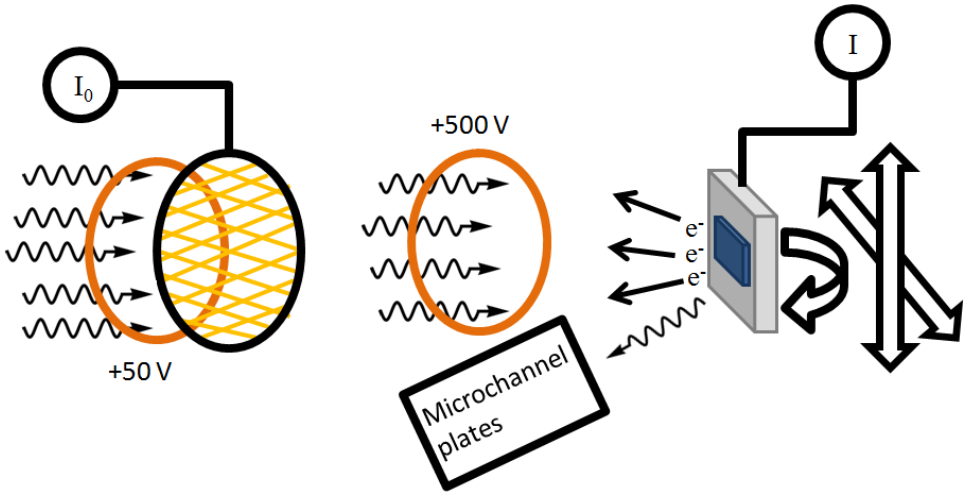

Figure 2.6: *Cartoon of XAS measurement apparatus.*

XAS measurements typically record three quantities as a function of photon energy: current to the sample, current to an upstream mesh, and fluorescent photon count from microchannel plates. Cu rings at a positive bias voltage are kept upstream of both the mesh and sample to increase electron yield. The mesh intercepts $\sim 10\%$ of the incoming photons and is ideally coated by evaporation *in situ* with a metal that has no absorption features at the relevant energy ranges (typically Au is a suitable metal).

2.4 Sample Preparation

Samples for the XAS measurements performed in this work were prepared in one of two ways: by drop casting from solution or by *in situ* sublimation. Both methods have advantages and disadvantages which will be detailed in the following sections. Occasionally a third preparation method, simply pressing a powder into carbon tape, was used, but this preparation method has many drawbacks which make it unsuitable for any but the most basic diagnostic use. In general drop cast samples sacrifice quality for time while samples prepared by *in situ* sublimation are of higher quality but sacrifice time.

Solution Preparation Methods

Preparation of samples by drop casting is used to make initial measurements on samples before more potentially destructive preparation methods such as sublimation are used. In some cases sublimation is not possible and drop casting is the only available preparation option, which is typically the case for smaller organic molecules or molecules which are stored in solution. Drop cast samples are prepared by dissolving or suspending a powder in some solvent (typically ethanol) and depositing a few drops of that solution onto a Si or Au substrate.

This method typically produces either thick, disordered films or nonuniform distribution of nucleated particles. In either case, the molecules are randomly oriented within the film, and the thickness of the film is sufficient that the effects of interactions with the substrate can be ignored. The quality of these samples in terms of peak height and resolution in their spectra is lower than for other preparation methods, but the drop cast samples serve as a good comparison to evaluate the quality of samples produced by other methods. Additionally, drop cast samples can be produced more quickly than by other methods of preparation. Details on specific drop cast samples will be given in later sections.

In Situ Sublimation

The preferred method for producing samples is *in situ* sublimation. This method uses a Knudsen cell (Fig. 2.7), which is a small Ta crucible through which current is run to heat a small amount of powder. Since this process occurs in vacuum, the powder sublimes out of the crucible and onto a room temperature substrate <1 cm away. The sublimed molecules then attach to the room temperature substrate and self-orient in layers. The temperature of the crucible is monitored by a thermocouple at its base.

In situ sublimation provides much greater control over the thickness of the samples

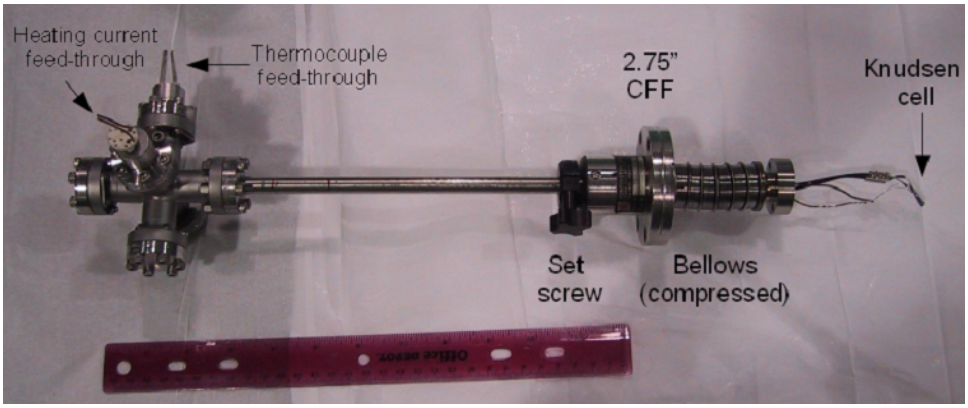

Figure 2.7: *Knudsen cell for* in situ *sublimation.*

The crucible is Ta foil which is heated by running a current through wires connected at its base, and the temperature is monitored by a thermocouple connected at the same point. When fully inserted into the vacuum chamber, the crucible sits < 1 cm from the substrate. The cell is kept under vacuum by a turbopump when not in use.

produced, creates well ordered samples, and provides the highest quality samples in terms of the relative intensities of spectral peaks. Additionally, since the samples are prepared in vacuum and at relatively high temperatures, oxidation of the molecules can in some cases be avoided or reversed, which is particularly important for molecules containing Fe.[22]

The downside of *in situ* sublimation as a preparation method is that it risks destroying the molecule if the temperature is too high. In some cases the molecule completely dissociates, leaving nothing on the substrate. This is typical of lighter molecules or molecules with smaller ligands such as polypyridyl-based molecules. Transition metal porphyrins and phthalocyanines decompose at high evaporation temperatures in a characteristic way that leaves nitrile fragments on the substrate with little to no trace of the metal center (see Chapter 3 for details). The method is also time consuming,

2.5 Methodology

Data Taking and Basic Analysis

Samples to be measured are attached to small aluminum holders using conductive carbon tape and loaded into the load lock on the chamber, where they are pumped on by a roughing pump and turbopump. The pumping process generally takes 2-3 hours to reach a similar vacuum to the measurement chamber, depending on the volatility of the samples. The samples can then be transferred onto the manipulator in the measurement chamber.

During measurement, the currents through the sample and the Au mesh are measured as a function of photon energy. If applicable, the count rate from microchannel plates measuring FY is also measured. These currents are proportional to the strength of the transitions at that energy. Photon flux is controlled by entrance and exit slits in the beamline, which are kept as narrow as possible along with changing spots on the sample after each spectrum to mitigate radiation damage to the samples. Spectra typically take 5-15 minutes depending on absorption edge and desired resolution. Calibration spectra are taken near in time to spectra of samples and each time a grating change is required.

The data processing procedure uses the recorded currents from the sample and the Au mesh in order to construct the spectra. The first step in data processing is dividing the sample current by the mesh current, which removes variations in photon flux from noise or monochromator transmission based on photon energy. This divided spectrum has a linear background in the pre-edge region, from which a straight line fit is subtracted. After the linear background is subtracted, the spectrum should in principle flatten out in the post-edge region. It should be noted that normalization to the pre-edge and subtraction of the linear background leaves the y axis as a measure of the signal-to-background ratio, which varies from one absorption edge to another, as mentioned in an earlier section. Figure 2.8 shows an example of these data processing steps for the N 1s edge of a phthalocyanine very similar

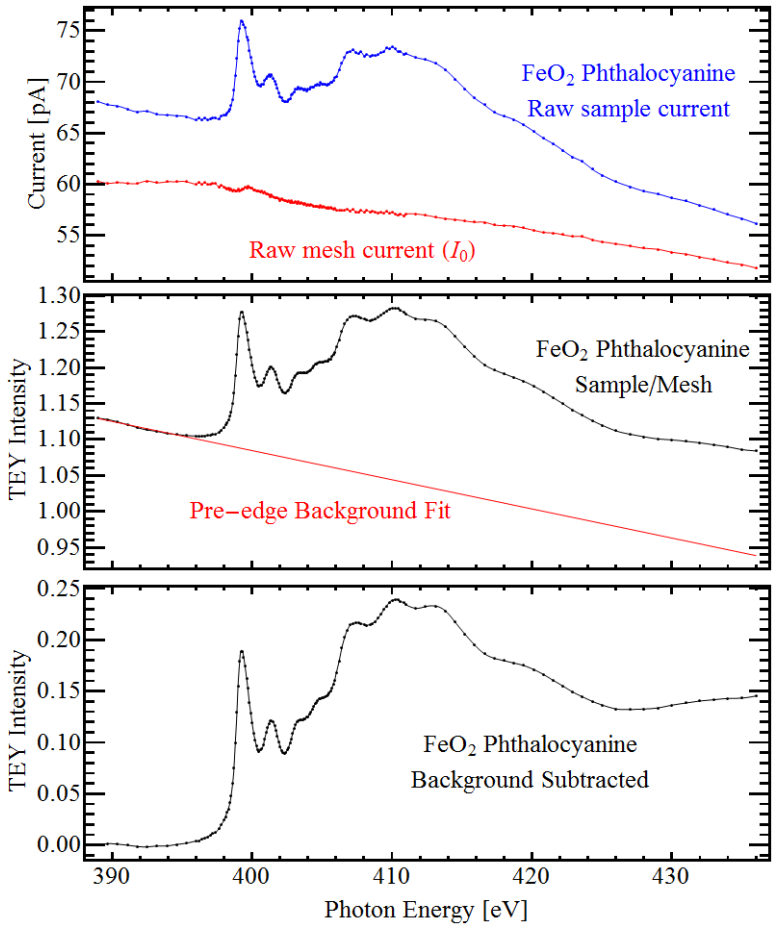

Figure 2.8: *Initial steps in processing of spectra.*

Top: Raw TEY signal from the sample and an upstream mesh, typically varying from pA to nA. Both are subject to the same change in flux with photon energy. Middle: The spectrum produced after dividing the signal from the sample by that from the mesh. The beamline drift is removed, but a linear background remains. The red line is a fit to the pre-edge background. Bottom: The spectrum after subtraction of the pre-edge background, which is now flattened.

to those in this work.

Calibration

Due to shifts in photon energy because of minor irreproducibility of grating position, it is necessary to calibrate all spectra using a convenient standard with well defined transition

Reference Compound	Absorption Edge	Transition Energy [eV]	Calibrated Absorption Edges
Highly Oriented Pyrolitic Graphite [37, 38]	C 1s	285.35 (C=C π^*)	C 1s
TiO_2 (Rutile) (Calibrated using N_2 [39])	Ti 2p	458.0 (Lowest 2p-to-3d)	N, O 1s
Ni mesh [40]	Ni 2p	852.6 (Ni 2p-to-3d)	Fe, Co, Ni, Cu, Zn 2p

Table 2.3: Commonly used calibration references.

energies. The best choices for calibration standards are molecules or crystals with transition energies near the absorption edge in question. For example, the C 1s edge is best calibrated using highly oriented pyrolitic graphite, which has a well defined C 1s to C=C π^* transition at 285.35 eV. Several common calibration standards and the absorption edges for which they are used are listed in Table 2.3. Because the monochromator is a plane grating, the calibration is linear in wavelength, i.e., $\lambda_a = \lambda_m + \Delta\lambda$, where λ_a is the wavelength corresponding to the actual energy, λ_m is the wavelength corresponding to the measured energy, and $\Delta\lambda$ is the required shift in wavelength for calibration. The shift in wavelength $\Delta\lambda$ is determined using the appropriate reference compound, since the actual transition energy (thus λ_a) for that compound is known from literature. This shift is then applied to the spectra for the relevant sample.

Since the photon energy rather than wavelength is the quantity that is actually recorded, it is useful to derive a calibration formula in terms of the energies involved rather than wavelengths. Taking $\Delta\lambda = \lambda\prime_a - \lambda\prime_m$ where the prime indicates that both values are for a specific transition in the reference compound, we have

$$\lambda_a = \lambda_m + \lambda'_a - \lambda'_m \tag{2.15}$$

Since $\lambda = hc/E$, then

$$\frac{1}{E_a} = \frac{1}{E_m} + \frac{1}{E'_a} - \frac{1}{E'_m} \tag{2.16}$$

which gives for the calibrated energy

$$E_a = \left(\frac{1}{E_m} + \frac{1}{E'_a} - \frac{1}{E'_m} \right)^{-1} = \frac{E_m E'_a E'_m}{E'_a E'_m + E_m E'_m - E_m E'_a} \tag{2.17}$$

where the measured and accepted from literature energies of a specific transition (E'_m and E'_a, respectively) are used to shift the spectrum of a sample appropriately.

Normalization for Polarization Dependence Experiments

For an isolated spectrum, the data processing is finished once the spectrum has had its linear background subtracted and energy calibrated. The resulting spectrum then has accurate transition energies and can be used to identify bonds if the sample is unknown or to contribute to an understanding of the electronic structure of the sample in conjunction with other types of spectroscopy. However, if the aim is to identify molecular orientation by studying the polarization dependence of specific orbitals, then additional processing is required, namely normalization of multiple spectra.

While all spectra are normalized at the pre-edge as a matter of standard procedure, pre-edge normalization does not account for the difference in exposed area due to rotation of the sample. For TEY measurements, the difference in effective path length of the incident photons has negligible effect on the signal. Likewise the shallow escape depth of the emitted electrons means that the primary increase to TEY signal is simply the larger exposed area, which in principle scales with $1/cos\theta$. The larger exposed area causes an increase in the intensity of the whole spectrum rather than any specific transitions, so only a constant scaling factor is needed to renormalize spectra taken at different angles of incidence. Any sufficiently flat portion of the spectra can also be used for a normalization region, but it is best to renormalize the spectra at an energy well above the absorption edge, where any tails from high energy transitions have flattened out and only transitions into continuum

states are present. After normalization at the step edge, transitions scale only based on the strength of the transition, which is dependent on molecular orientation.

In some cases the step edge is not consistent enough among the spectra to serve as a good region for renormalization. This typically occurs when the sample is very thin, on the order of a monolayer or less, or when the sample is prone to charging. In those cases the step edge varies beyond what one would expect from simply a greater exposed area, or the spectrum has a nonlinear background. The better choice for a normalization region for such samples is to find the point in each spectrum where there is a crossover between orthogonal orbitals (typically between the π^* and σ^* regions). Such a normalization risks misrepresenting the angular dependence of the transitions because the chosen point of normalization will in general sit on one or more tails from nearby transitions or potentially sit on a small transition masked by the larger tails, causing the normalization point to change beyond what would be expected based on just the larger exposed area. This technique is best used for simple molecules with fewer, well separated peaks where the risk of sitting on a nearby tail is minimized.

Au Double Division

A common but correctable source of error is contamination of the Au mesh, typically by hydrocarbons or nitrogen-containing molecules. This contamination shows up as peaks in the mesh spectrum which, when the sample spectrum is divided by the mesh spectrum, will produce dips below the baseline. While these dips are very small and have a negligible effect on the spectra of samples with good signal, very thin samples have low enough signal that the dips can no longer be ignored. The best solution to contamination of the mesh is to evaporate a fresh layer of Au onto the mesh, but when doing so is not practical then it is possible to remove the effects of mesh contamination by a double division process. Double division requires taking a spectrum of a clean Au sample at the same absorption edge and

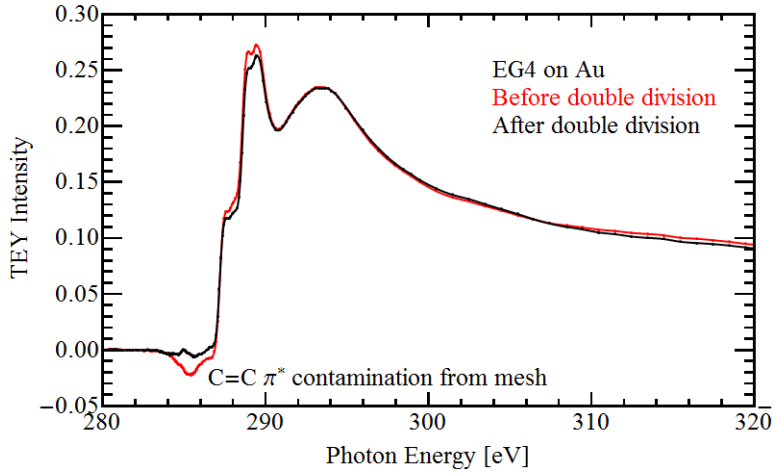

Figure 2.9: *Effect of double division by clean Au.*

This spectrum of an EG4-terminated alkanethiol SAM on Au was taken when the upstream Au mesh had been contaminated with hydrocarbons (red spectrum), which is apparent from a dip below the baseline at 285 eV, characteristic of transitions into the C=C π^* orbital. For thick samples this small amount of contamination would be negligible, but for monolayers it cannot be ignored. The black spectrum is the same spectrum after double division by a clean Au sample. The C=C π^* contamination is almost completely removed.

dividing it by the contaminated mesh. The divided spectrum of the original sample is then divided by that of the clean Au sample, with the end result that the signal from the sample is divided by the signal from the clean Au, i.e.,

$$\frac{I_{Sample}}{I_0} \cdot \frac{I_0'}{I_{Au}} = \frac{I_{Sample}}{I_{Au}} \tag{2.18}$$

where I_{Sample} is the signal from the sample, I_0 is the signal from the mesh taken simultaneously with I_{Sample}, I_{Au} is the signal from the clean Au, and I_0' is the signal from the mesh taken simultaneously with I_{Au} which should be identical to I_0. Because the mesh contamination is a significant contribution to the divided spectra, it is imperative that all spectra are exactly aligned to each other to properly cancel out the contamination on the mesh. Figure 2.9 shows an example of how double division by clean Au can remove the effects of C contamination on the mesh from the spectra.

Chapter 3

Ruthenium Substitution by Iron

This work is published in P. S. Johnson, P. L. Cook, I. Zegkinoglou, J. M. García-Lastra, A. Rubio, R. E. Ruther, R. J. Hamers, F. J. Himpsel, "Electronic Structure of Ru- vs. Fe-Based Dye Molecules," *J. Chem. Phys.* **138**, 044709 (2013).[41]

3.1 Introduction

Dye-sensitized solar cells frequently use metal-organic dye molecules containing the rare metal ruthenium,[42] which hampers large-scale applications in photovoltaic power plants. On the other hand, similar types of charge transfer reactions are carried out in biological systems by heme-based molecules containing iron as the active redox center. Since Fe is located just above Ru in the periodic table, the question arises whether it is possible to use abundant Fe instead of the rare Ru for dye-sensitized solar cells.[22] A similar question has come up in the context of Fe- versus Ru-based catalysts.[43]

Many different metal-organic dye molecules have been used for photovoltaics[44, 42, 45, 4], but most of them are characterized by a metal atom surrounded by a cage of N atoms. The cage can be two-dimensional (in porphyrins and phthalocyanines) or three-dimensional

(in polypyridyl structures). Systematic work on the electronic structure of two-dimensional dyes can be found in Refs. [44, 23, 46, 47, 48, 49]. For three-dimensional complexes the electronic structure[50, 51, 52, 53, 54, 55] and charge transfer[56, 57, 58, 59, 60, 61, 62] have been investigated using many spectroscopic[63, 64, 65, 66, 67, 68, 69, 66] and theoretical[70, 71, 72, 73, 74, 75, 76, 77, 78] methods.

Despite the analogy between Fe and Ru in the periodic table, there are several subtle differences in their electronic structure. For example, Fe is significantly less electronegative than Ru (1.83 versus 2.2) and thus more prone to transfer electron charge to ligands. Both Fe and Ru exhibit a wide range of oxidation states (from -2 to +6 for Fe and from -2 to +8 for Ru), but Fe prefers the +3 oxidation state while Ru prefers +2 and +4, with +2 representing the typical oxidation state of Ru in dye molecules. A special feature of neutral Ru is the transfer of an outer s-electron to the d-shell, which leads to a different configuration of the active d-electrons. This is less important in dye molecules, where Fe and Ru are oxidized to +2 (d^6) or +3 (d^5).

The 3d valence electrons of Fe differ from the 4d electrons of Ru in several aspects. The smaller spatial extent of the Fe 3d vs. Ru 4d wave functions leads to a smaller bond length between Fe and N (see Section 3.4 for two-dimensional molecules and Ref. [79] for three-dimensional molecules). Superficially, this suggests a larger overlap between the metal d-electrons and the adjacent N 2p electrons for Fe. On the other hand, the N cage is fairly stiff, particularly in planar dye molecules. It is not flexible enough to completely accommodate the difference in the ionic radii. Therefore the overlap is smaller for Fe, and likewise the hybridization between the metal d electrons and the N 2p electrons.

Like the hybridization, the crystal field splitting decreases substantially from the 4d to the 3d manifold. The lower crystal field splitting in Fe makes it possible to promote electrons from the filled t_{2g} to the empty e_g states in order to have parallel spins.[80] As a consequence, Ru tends to be in the low spin configuration while Fe can also occur in the

high spin configuration. For example, the gap between the t_{2g}- and e_g-derived states is 2.9 eV for RuCO octaethyl porphyrin and 0.8 eV for FeCl octaethyl porphyrin according to our calculations.

An additional splitting is caused by the spin-orbit interaction, which can be quantified by the parameter ζ' defined in Refs. [81] and [82], which is 0.13 eV for the 4d electrons[81] in atomic Ru^{2+} and 0.05 eV for the 3d electrons[82] in atomic Fe^{2+}. The different strength of the spin-orbit interaction affects the optical transitions in the visible and UV, particularly luminescence and circular dichroism. When compared to the interaction between the transition dipoles on the ligands, the spin-orbit interaction dominates in $Ru(phen)_3^{2+}$ while being small in $Fe(phen)_3^{2+}$ (see Table 1 in Ref. [78]). That changes the sequence of the lowest excited orbitals from $^3A_2 < ^1A_2 < ^1E$ for Ru to $^1E < ^3A_2 < ^1A_2$ for Fe. The effect of the spin-orbit interaction on the electronic structure has been studied in detail for the Fe-, Ru-, and Os-tris(bipyridine) series which covers the 3d, 4d, and 5d shells.[50, 83, 84, 85] Here we restrict ourselves to the Fe-Ru comparison, but extend the scope to a broader class of dye molecules, i.e. tris(phenanthroline) and octaethyl porphyrin (OEP) in addition to tris(bipyridine).

The spin-orbit splitting affects the highest occupied molecular orbital (HOMO), which tends to have metal d character, while the lowest unoccupied molecular orbital (LUMO) has usually N 2p character in the metal-organic dye molecules discussed here.[50, 23] In a dye-sensitized solar cell the HOMO is relevant to refilling the hole, which may occur from the donor or the acceptor (as undesirable back electron transfer). The LUMO mediates the extraction of excited electrons via injection into an oxide acceptor, such as TiO_2. This part of the electron-hole separation involves very little voltage loss, but the lack of a strong driving potential makes it slow. A rapid refilling of the hole via the donor is required to minimize back electron transfer from the acceptor, and that entails a substantial loss of open circuit voltage.[42, 4] This has been a particular problem with Fe-based dyes.

The most glaring chemical difference between Fe and Ru is the resistance of Ru against

oxidation, which is related to its higher electronegativity. This property is important for practical purposes (lifetime of a solar cell and necessity of careful encapsulation). For example, Fe^{2+}-phthalocyanine has been found to oxidize in air to Fe^{3+} (Ref. [22]), while Ru^{2+}-phthalocyanines remain stable.[52, 86] Fe^{2+}-porphyrin appears to be even more difficult to stabilize. We were unable to desorb Cl from FeCl-OEP. In biomolecules, such as the heme, the central Fe atom is protected from oxidation by a three-dimensional cage of N (or S) atoms with approximately octahedral symmetry. This suggests searching for dye molecules containing Fe in similar octahedral cages, but without the protein backbone which is fragile and prone to radiation damage.[87, 27] This avenue will be pursued further in a separate publication.[88] Overall, this research is part of a program to measure the energy levels relevant to the performance of solar cells.[89] Such results provide the input for designing optimized combinations of materials for solar cells.

With this goal in mind we have investigated the differences in the electronic structure of Fe- and Ru-based dye molecules, combining X-ray absorption spectroscopy at the N 1s and C 1s edges with density functional theory (DFT). Thereby we address the LUMO, which can be accessed by the same absorption edge (N 1s-to-2p) for both Fe and Ru complexes (for previous work see Refs. [50, 67, 53, 57]). Addressing the HOMO requires two different absorption edges, i.e., Fe 2p-to-3d at 0.7 keV (see Refs. [63, 68, 64, 61, 69, 66]) and Ru 2p-to-4d at 2.8 keV (see Ref. [62, 65, 57]). Various core level absorption edges have been studied by ultrafast core level pump-probe techniques.[63, 64, 61, 62, 65, 66, 67]

The N 1s absorption edge is of particular interest, because the immediate neighbors of the metal atom are N atoms in the dyes studied here. Their π^* orbitals tend to dominate the LUMO,[23] although occasionally one of the unoccupied metal d-orbitals drops below the lowest π^* level or hybridizes with it.[51] The transition energy from the N 1s core level to the LUMO is sensitive to the charge transfer between the metal atom and the surrounding N cage, as demonstrated for a series of OEPs with 3d metals at the center.[23] We find a

similar charge transfer shift in a variety of Fe- and Ru-based dye molecules.

The key result can be summarized as follows: 1) There is a systematic downward shift of the N 1s-to-π^* transition when replacing Ru by Fe in tris(bipyridines) and tris(phenanthrolines), while OEPs exhibit a more subtle behavior. 2) The origin of this shift can be traced to a chemical shift of the N 1s core level, caused by electron charge transfer from the metal to the surrounding nitrogens. 3) This charge transfer is larger for Fe than Ru, due to the lower electronegativity of Fe.

3.2 Experimental

Materials

Ruthenium(II) tris(bipyridine) $Ru(bpy)_3^{2+}$, iron(II) tris(bipyridine) $Fe(bpy)_3^{2+}$, ruthenium(II) tris(phenanthroline) $Ru(phen)_3^{2+}$, iron(II) tris(phenanthroline) $Fe(phen)_3^{2+}$, more commonly known as the redox indicator ferroin, ruthenium(II) carbonyl octaethyl porphine RuCO-OEP, iron(III) chloride octaethyl porphine FeCl-OEP, H_2 octaethyl porphine H_2-OEP, bathophenanthroline, and dimethyl phenanthroline were purchased from Sigma-Aldrich and used as received. Carboxylated bipyridine (a.k.a. biisonicotinic acid) was deposited on a smooth layer of ZnO nanoparticles. $Ru(bpy)_3^{2+}$, $Fe(bpy)_3^{2+}$, $Ru(phen)_3^{2+}$, bathophenanthroline, and dimethyl phenanthroline were dissolved in ethanol and drop cast on Au-coated Si wafers. $Fe(phen)_3^{2+}$ was purchased in aqueous solution and drop cast on Au-coated Si.

The best quality spectra (with the narrowest peaks and largest peak-to-valley ratios) were obtained from *in-situ* sublimed samples. However, sublimation was not suitable for all dye molecules, as some of them decomposed before reaching sufficient vapor pressure (Fig. 3.1). Typical decay products were nitriles, which give rise to a characteristic π^* peak at 399.9 eV (Ref. [27]). Drop casting was also used. Spectra from such samples showed only weak dependence on the solvent, as long as pure solvents without aqueous contamination

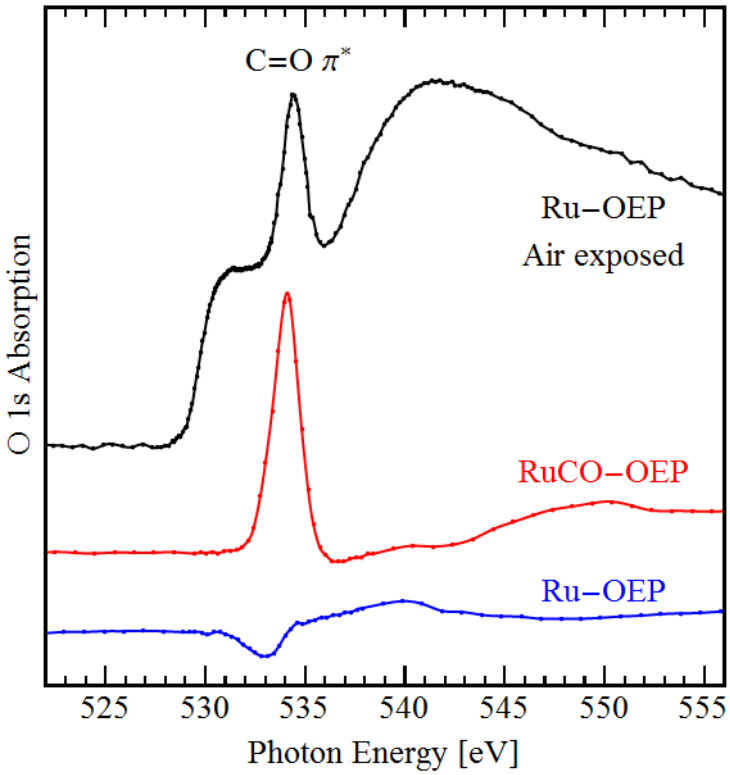

Figure 3.1: *Removal of the CO ligand from RuCO-OEP by sublimation at high temperature.*

O 1s spectrum of RuCO-OEP sublimed at 253±5 °C (center), compared to that of Ru-OEP sublimed at 415±5 °C (bottom), where the CO ligand is thermally desorbed. Correspondingly, the characteristic π^* transition of the axial CO ligand disappears. It reappears after exposure to air (top).

were used.

Thermal desorption was used to remove the axial CO ligand from RuCO-OEP at about 400 °C, well above the typical OEP sublimation temperature of 250 °C (Fig. 3.1). However this requires that the axial ligand be less strongly bound than the porphyrin ring. For FeCl-OEP, the porphyrin ring breaks before Cl is removed (see Fig. 3.2).

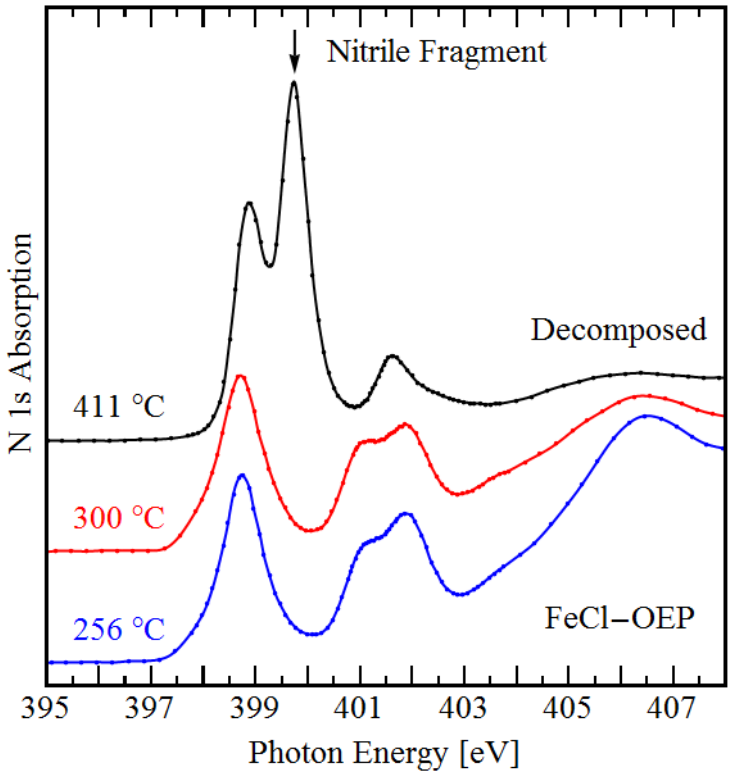

Figure 3.2: *Decomposition of FeCl-OEP by high temperature sublimation.*

Preparation of a well-ordered thin film of FeCl-OEP dye molecules by *in-situ* sublimation (bottom and center). Care needs to be taken to keep the sublimation temperature below the decomposition temperature. At higher temperatures (411±5 °C, top), nitrile fragments can be detected at the N 1s edge by their characteristic π^* peak at 399.9 eV (see Fig. 6 b,c in Ref. [27]).

X-ray Absorption Measurements

X-ray absorption measurements were performed at two undulator beamlines: Beamline 8.0 of the ALS and the VLS-PGM beamline at the SRC. At the ALS it was possible to simultaneously acquire surface-sensitive total electron yield (TEY) spectra and bulk-sensitive total fluorescence yield (TFY) spectra. Details of the experimental setup have been reported elsewhere.[27, 26] For measuring the small energy shifts at the N 1s edge, it was necessary to ensure that the photon energy was stable. Therefore analogous spectra of Fe- and Ru-based

molecules were taken right after each other. The absolute photon energy calibration was checked frequently by measuring the C 1s edge of graphite at grazing incidence, the Ti 2p edge of rutile TiO_2, and the Ni 2p edge of a Ni mesh. Details about the energy calibration and resolution can be found in Ref. [27].

Density Functional Theory Calculations

Density Functional Theory (DFT) calculations were performed by Juan Maria García-Lastra of the Department of Energy Conversion and Storage at the Technical University of Denmark.

The DFT calculations were carried out by means of the Amsterdam density functional (ADF) code.[90] All atoms were described through basis sets of TZP quality (triple-ζ STO plus one polarization function) given in the program database, including all the core electrons in the calculation (i.e. with no frozen core approximation). The exchange-correlation energy was computed according to the local density approximation (LDA) by means of the Vosko-Wilk-Nussair[91] (VWN) functional. The first step of the calculations consists of obtaining the structures of the different OEPs in their ground state. In a second step the N 1s-to-LUMO transition was calculated using the ΔSCF method. We have also performed DFT calculations using the transition state (TS) theory proposed by Slater. The details of the ΔSCF and TS methods are described in Ref. [23].

3.3 Results

N 1s Absorption Spectra

Figure 3.3 compares the N 1s absorption spectra of various bipyridines. For $Ru(bpy)_3^{2+}$ and $Fe(bpy)_3^{2+}$ the bulk-sensitive fluorescence yield spectra are shown (in order to eliminate the contribution from surface oxides), and for metal-free carboxylated bipyridine on ZnO the

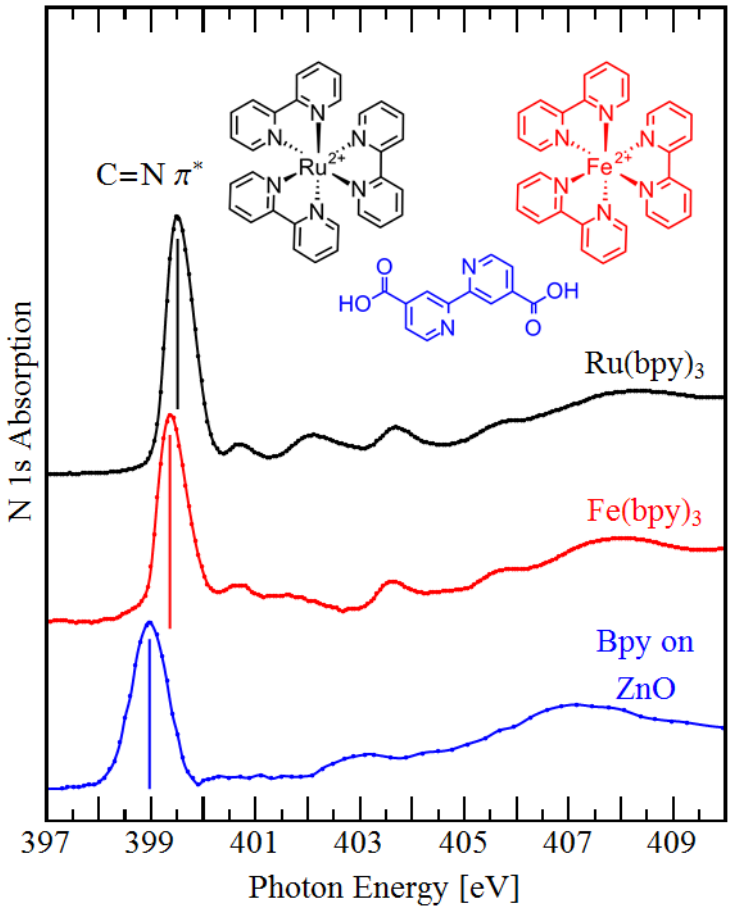

Figure 3.3: *N 1s spectra of bipyridine-based molecules.*

The lowest N 1s-to-π^* transition shifts down by 0.15 eV when replacing Ru by Fe, due to a decrease in the N 1s core level binding energy that is caused by an extra transfer of negative charge from Fe to the N ligands.

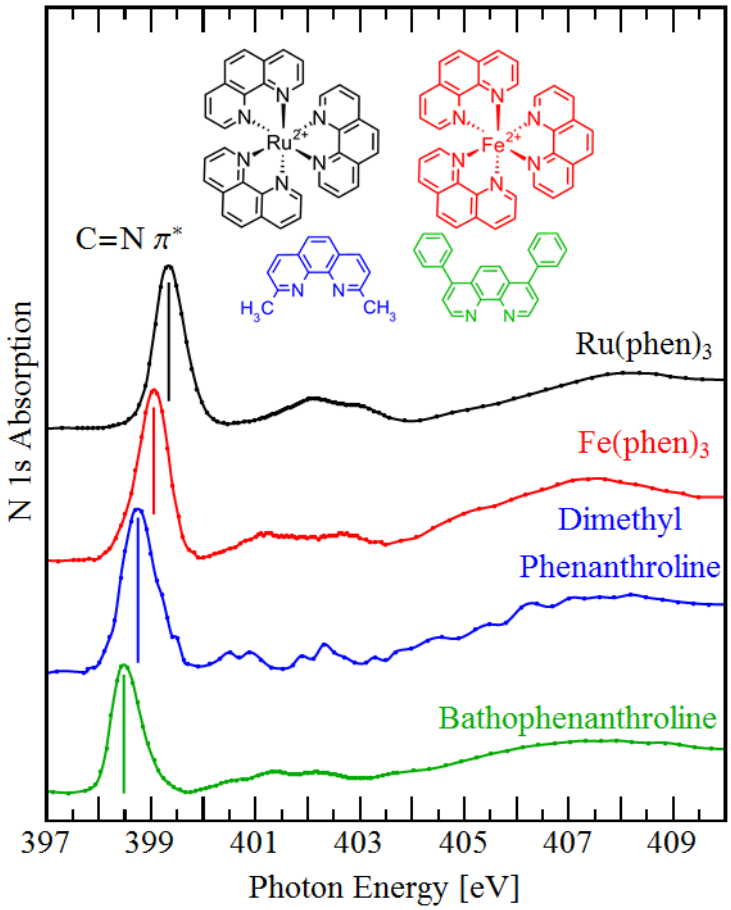

Figure 3.4: *N 1s spectra of phenanthroline-based molecules.*

The lowest N 1s-to-π^* transition shifts down by 0.3 eV when replacing Ru by Fe. Similar to the bipyridine-based molecules, the shift is due to a decrease in the N 1s core level binding energy.

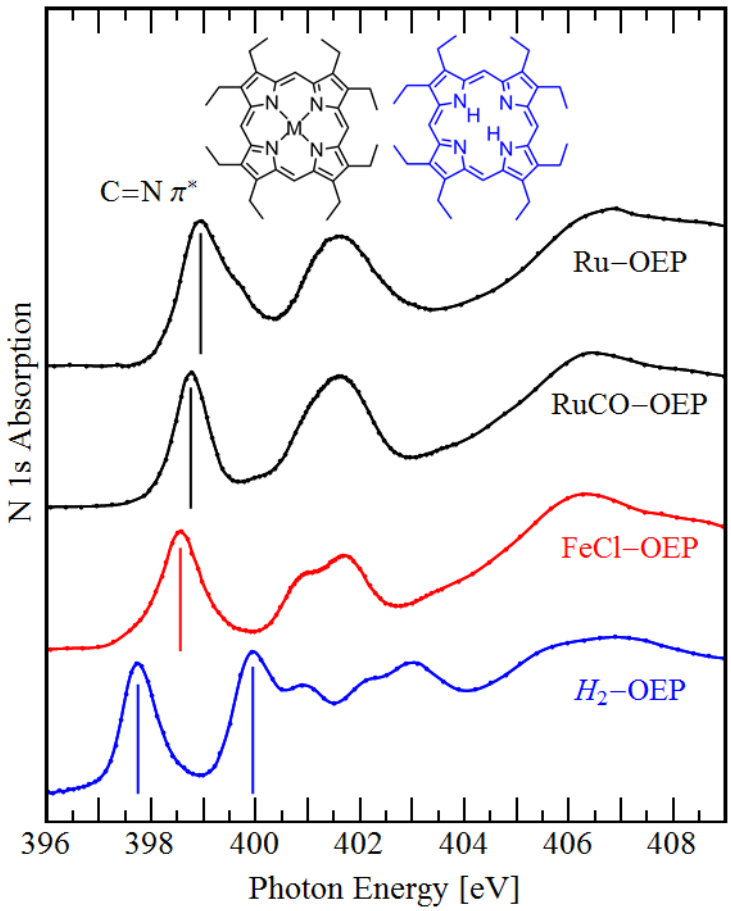

Figure 3.5: *N 1s spectra of OEP-based molecules.*

The lowest N 1s-to-π^* transition shifts down by 0.2 eV going from RuCO-OEP to FeCl-OEP (second and third curves). Removal of the CO ligand from RuCO-OEP increases the transition energy by 0.2 eV (top curve). In H_2-OEP the lowest π^* transition splits because of two inequivalent N atoms (bottom curve).

electron yield spectrum. The dominant peak in all spectra is the transition from the N 1s core level to the lowest π^* orbital below 400 eV. Weaker transitions into higher-lying π^* orbitals are visible in the 400-405 eV range, plus a broad σ^* resonance near 408 eV. When going from Ru- to Fe-tris(bipyridine), the dominant π^* peak shifts down in energy by 0.15 eV. The next three peaks shift in the same direction, indicating a common contribution from a shift of the N 1s core level induced by charge transfer. This is confirmed by the calculations in Section 3.4, where the N 1s core level shifts, while the LUMO stays constant. A common shift of two π^* peaks is also observed at the C 1s edge of the bipyridine-based molecules (see Section 3.3).

Figure 3.4 shows the N 1s absorption spectra for a series of phenanthrolines in the TEY mode, i.e., $Ru(phen)_3^{2+}$, $Fe(phen)_3^{2+}$, together with metal-free dimethyl phenanthroline and bathophenanthroline. The spectra are again dominated by the lowest π^* transition, with weaker π^* and σ^* features at higher energy. Analogous to the bipyridine molecules, a downward energy shift of the lowest π^* peak is observed going from Ru to Fe (here 0.3 eV), together with a further downshift for the metal-free variants. The noisy signal from dimethyl phenanthroline is due to its higher vapor pressure, which causes bursts of molecules to desorb from the substrate during the measurement.

Figure 3.5 is analogous to Figs. 3.3 and 3.4, but for octaethylporphyrin (OEP) molecules. They exhibit a planar cage of four nitrogens around the metal atom instead of three-dimensional cage of six N atoms. The N 1s absorption spectra are given for RuCO-OEP, Ru-OEP, FeCl-OEP, and H_2-OEP, all in the TEY mode. For Ru-OEP the CO ligand was removed by sublimation at a higher temperature, as shown in Fig. 3.2. The metal-OEPs generally exhibit smaller shifts of the lowest π^* peak than the molecules with three-dimensional cages in Figs. 3.3 and 3.4. In the metal-free H_2-OEP the lowest π^* peak is split, because there are two pairs of inequivalent N atoms (one pair bonding to H, the other not). The lower peak (397.75 eV) is due to the H-free N atoms, and the higher peak (399.95 eV) to

Table 3.1: Observed N 1s-to-π^* Transition Energies

Molecule	Transition Energy [eV]
$Ru(bpy)_3^{2+}$	399.51 ($\pm$0.05)
$Fe(bpy)_3^{2+}$	399.36
Bipyridine on ZnO	398.97
$Ru(phen)_3^{2+}$	399.34
$Fe(phen)_3^{2+}$	399.05
Dimethyl Phenanthroline	399.75
Bathophenanthroline	399.48
Ru-OEP	398.95
RuCO-OEP	398.76
FeCl-OEP	398.56
H_2-OEP	397.75, 399.95

the N bonded to H (see the two vertical lines in the bottom curve of Fig. 3.5).

The energies of the lowest N 1s-to-π^* transitions marked by lines in Figs. 3.3-3.5 are summarized in Table 3.1. The origin of the energy shifts will be investigated in Section 3.4.

C 1s Absorption Spectra

Figure 3.6 shows the C 1s fluorescence yield spectra of $Ru(bpy)_3^{2+}$, $Fe(bpy)_3^{2+}$, and the electron yield spectrum of carboxylated bipyridine on ZnO. Compared to the N 1s edge in Fig. 3.3, the shifts of the LUMO transition are in the opposite direction at the C 1s edge. Instead of a 0.15 eV downward shift at the N 1s edge one observes an upward shift of 0.15 eV for C 1s when going from Ru to Fe. A second strong π^* transition is observed at 0.8-0.9 eV higher energy. The two π^* peaks are assigned to transitions into the same π^* orbital, but from inequivalent C atoms. The lower peak is assigned to the three C atoms bonded to other carbons ($C_{3,4,5}$) and the upper peak to the two C atoms bonded to nitrogen ($C_{2,6}$). The latter has higher binding energy due to electronic charge transfer from C to N. The two corresponding C 1s core levels have been observed by XPS[50] with a similar splitting (about 1.0 eV), similar intensity ratio (3:2), and the same assignment. Both π^* transitions

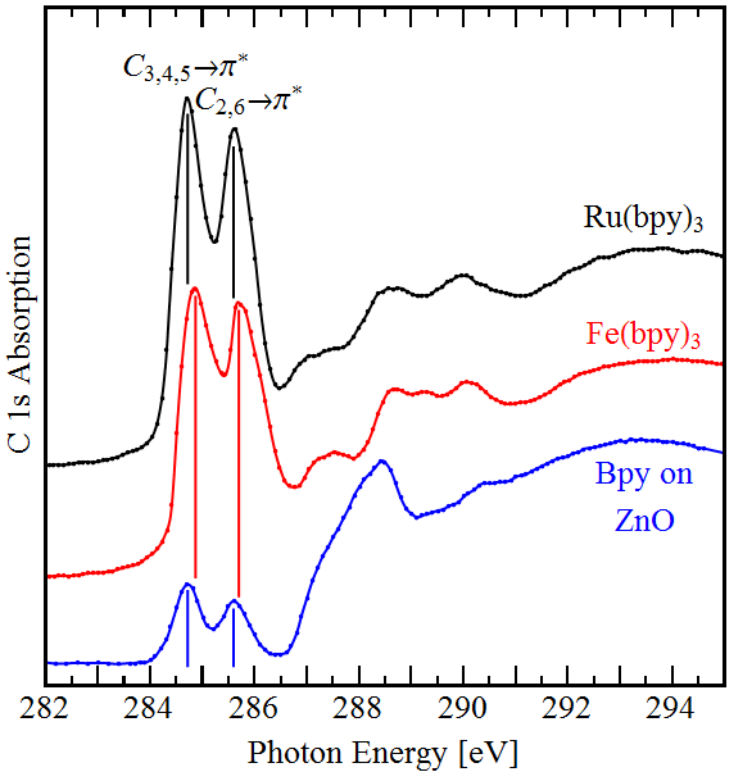

Figure 3.6: *C 1s spectra of bipyridine-based molecules.*

The C 1s-to-π^* transition energy increases by 0.15 eV when replacing Ru by Fe. The second π^* transition at higher energy shifts by the same amount, suggesting a transition into the same π^* orbital from a second set of C atoms with higher binding energy (those binding to N).

shift by a similar amount, indicating a similar charge transfer to both types of C atoms via the common π system. The sign of the shift indicates removal of electronic charge from the π system.

Figure 3.7 shows a similar trend in the C 1s spectra of Ru(phen)$_3^{2+}$, Fe(phen)$_3^{2+}$, dimethyl phenanthroline, and bathophenanthroline. Again there is an upward shift of the LUMO peak when going from Ru to Fe (by 0.05 eV), compared to a downward shift at the N 1s edge in Fig. 3.4 (by 0.3 eV). It is tempting to assign the three strong π^* peaks to transitions from three inequivalent C atoms into the same, delocalized π^* system, as in the tris(bipyridines).

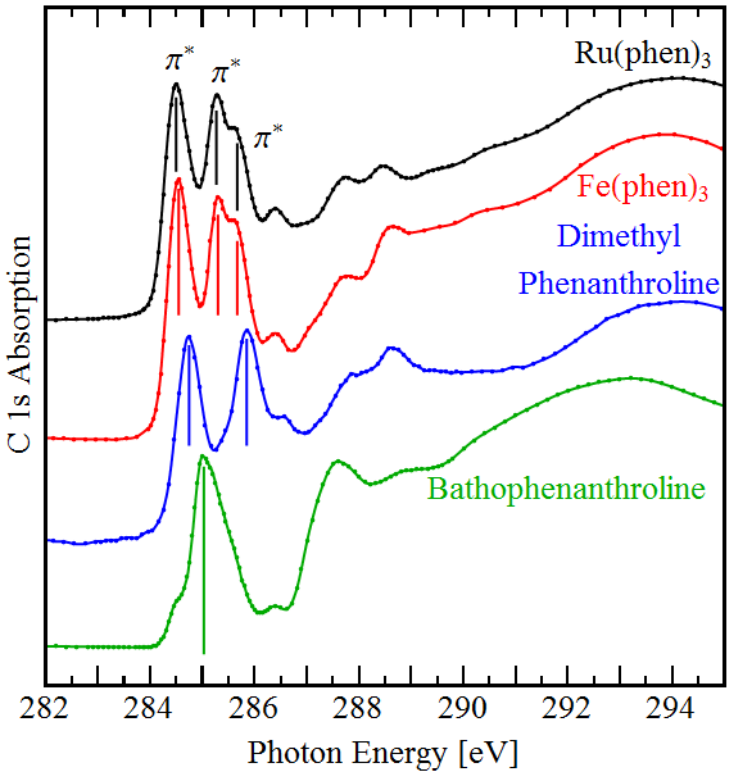

Figure 3.7: *C 1s spectra of phenanthroline-based molecules.*

The C 1s-to-π^* transition energy increases by 0.05 eV when replacing Ru by Fe. The smaller shift compared to the bipyridine-based molecules is likely due to delocalization of the charge transfer over the larger π system of phenanthroline.

In contrast to the tris(bipyridine) dyes, the magnitude of this C 1s shift is significantly smaller, pointing toward a delocalization of the charge transfer over the larger π system of phenanthroline.

In bathophenanthroline the extra phenyl groups are responsible for the dominant C=C π^* feature which obscures the double peaks seen in the other phenanthroline-based molecules. The low-energy shoulder in the bathophenanthroline spectrum lies close to the lowest π^* peaks of the other molecules.

Figure 3.8 shows the C 1s spectra for Ru-OEP, RuCO-OEP, FeCl-OEP, and H_2-OEP. Unlike for the other molecules, the lowest π^* peak shifts upward when going from FeCl-

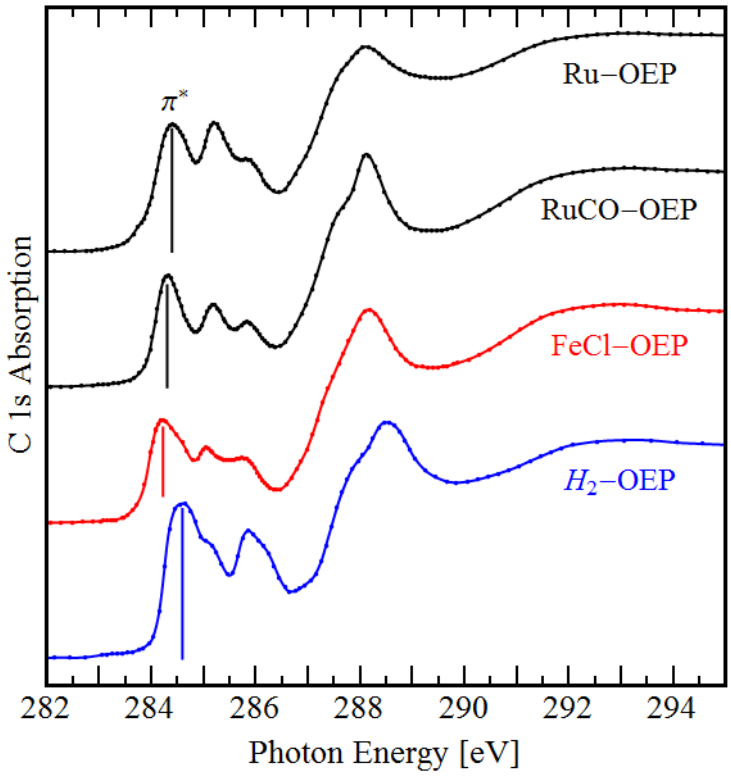

Figure 3.8: *C 1s spectra of OEP-based molecules with a planar N cage.*

The C 1s-to-π^* transition energy decreases by about 0.1 eV when going from Ru- to Fe-based OEPs, opposite to the behavior of the dye molecules with three-dimensional cages in Figs. 3.6 and 3.7.

to RuCO-OEP. It shifts further upward when removing the CO to form Ru-OEP. The magnitude of each of these shifts is about 0.1 eV. The energies of the C 1s transitions marked by lines in Figs. 3.6, 3.7, and 3.8 are summarized in Table 3.2.

Table 3.2: Observed C 1s-to-π^* Transition Energies

Molecule	Transition Energies [eV]
$Ru(bpy)_3$	284.72, 285.60 ($\pm$0.05)
$Fe(bpy)_3$	284.87, 285.70
Bipyridine on ZnO	284.72, 285.60
$Ru(phen)_3$	284.50, 285.27, 285.67
$Fe(phen)_3$	284.55, 285.30, 285.67
Dimethyl Phenanthroline	284.75, 285.85
Bathophenanthroline	285.03
Ru-OEP	284.40
RuCO-OEP	284.31
FeCl-OEP	284.23
H_2-OEP	284.60

3.4 Discussion

Systematic Shift at the N 1s Edge

The key trend at the N 1s absorption edge is a systematic downward shift of the N 1s-to-π^* transition when going from Ru to Fe (and eventually to metal-free dye molecules). Such a shift can be explained by transfer of negative charge from the metal to the neighboring N atoms, as investigated in more detail in previous work on 3d metal OEPs.[23] The smaller electronegativity of Fe compared to Ru increases the transfer of negative charge from Fe to its N ligands, thus decreasing the binding energy of the N 1s electrons. This model is supported by XPS measurements of the N 1s core level and the HOMO for the Fe-, Ru-, Os-tris(bipyridine) series.[50] From Ru to Fe, the N 1s level shifts up by 0.08 eV and the HOMO shifts up by 0.35 eV.[50] This gives an upwards shift of 0.28 eV for the binding energy of the N 1s relative to the HOMO, which parallels the observed upward shift of 0.15 eV for the N 1s-to-π^* transition.

While the N atoms in the tris(bipyridine) and tris(phenanthroline) molecules exhibit a six-fold, approximately octahedral arrangement around the metal,[79] there are only four N atoms surrounding the metal in the OEPs. These structures may be viewed as three-

dimensional and two-dimensional cages, respectively. Aside from the change in the number of N ligands, the cage structure also affects the crystal field that splits the metal d-levels and shifts the N 2p levels. The bonding geometry of the metal atom also affects the oxidation state, which in turn affects the charge transfer to the N ligands. In particular, Fe is in the +2 oxidation state in the three-dimensional cages of the tris(bipyridine) and tris(phenanthroline) molecules, whereas it prefers the +3 oxidation state in the two-dimensional, planar cages of OEP or phthalocyanine molecules. Ru, on the other hand, prefers the +2 oxidation state in OEPs and phthalocyanines.[52, 86] As a result we have only been able to make a direct comparison between Ru^{2+} in RuCO-OEP and Fe^{3+} in FeCl-OEP. Removal of the Cl from FeCl-OEP without breaking the molecule apart has not been possible (compare Fig. 3.2). In order to sort out the contributions from the oxidation state and the axial ligand we have calculated the electronic structure of Ru- and Fe-OEPs for various combinations of oxidation states and axial ligands.

Calculation of the Energy Shift

First-principles DFT calculations of the N 1s-to-π^* transitions were performed for the combinations of metal, oxidation state, and axial ligand that are relevant to our data (RuCO-OEP, FeCO-OEP, RuCl-OEP, FeCl-OEP). The methodology has been tested previously with a series of 3d transition metal OEPs,[23] where the details of the calculations are described. The results are given in Table 3.3. The N 1s-to-π^* transition energy can be decomposed into three contributions, i.e., the N 1s core level energy, the LUMO energy, and the Coulomb interaction between an electron in the LUMO and the N 1s core hole. In previous systematic work it was found that the largest variation within the 3d metal series was caused by a shift of the N 1s level due to varying charge transfer from the transition metal to the N.[50] Here we have to consider two additional effects, the change in the oxidation state and the change from a 3d to a 4d metal. It turns out that these effects have comparable influence on the

shifts.

The calculated shifts in Table 3.3 reveal some trends for the porphyrins. Going from Ru to Fe in the same molecule, the N 1s level moves down, which is opposite to the trend encountered with the three-dimensional cages. But this is consistent with the calculated charge on the N atoms which is less negative with Fe. At a first glance, such a charge transfer seems to be at variance with the lower electronegativity of Fe. The calculation reveals that some of the negative charge donated by Fe is diverted to the axial Cl ligand, which leaves less negative charge on the N. For example, the Cl ligand receives a charge of -0.375 e in FeCl-OEP, while it gets only -0.335 e in RuCl-OEP.

The LUMO and the electron-hole interaction do not change significantly, analogous to the trend found along the 3d series.[23] The fact that the LUMO remains nearly unchanged relative to the vacuum level implies that one should not expect a large difference in the band offset between LUMO and acceptor, at least within the approximate electron affinity model. The band offset is an important factor in the back electron transfer. The change in oxidation state shifts the LUMO by at most 0.01 eV, which is within the uncertainty of the calculation.

The comparison between theory and experiment for the measured N 1s-to-π^* shift between RuCO-OEP and FeCl-OEP comes out qualitatively correct in the ΔSCF calculation: The calculated shift is 0.06 eV toward lower energy, while the experimental shift is 0.2 eV in the same direction. These shifts are close to the theoretical and experimental accuracy limits and should not be taken quantitatively. The ΔSCF method has been recently compared to the more sophisticated time-dependent DFT method and was found to give comparable accuracy.[92]

The HOMO is formed by the metal d_{xy} orbital and the HOMO-1 by the $d_{xz,yz}$ and N $2p_z$ orbitals, but all three are nearly degenerate in energy. The occupancy of the d-orbitals differs from that of Mn-OEP in Ref. [23], because Mn-OEP is in the high spin configuration

with a total spin of 5/2 for the five d electrons of Mn^{2+}. As a result, all the d-levels of Mn are singly occupied. Fe^{2+} in FeCO-OEP and Ru^{2+} in RuCO-OEP contain six d-electrons, and these are in the low spin state with total spin 0. Consequently, the three lowest d-levels of Fe and Ru are doubly occupied, and the two uppermost d-levels are empty. The occupied d-levels are derived from t_{2g} states, and the unoccupied d-levels e_g.

In order to compare the differences between Ru and Fe we have investigated the degree of hybridization between their states and its relation to the bond length. The Fe-N distance in FeCO-OEP is 0.08 Å shorter than the Ru-N distance in RuCO-OEP (both in the same oxidation state). In the three-dimensional cage molecules $Fe(bpy)_3^{2+}$ and $Ru(bpy)_3^{2+}$, the Fe-N bond length is 0.085 Å smaller than the Ru-N bond length.[79] This trend reflects the smaller radius of the 3d wave function in Fe compared to the 4d wave function in Ru. However, the difference is significantly smaller than 0.13 Å, the difference between the ionic radii of Ru and Fe. The porphyrin ring is too stiff to allow relaxation of the N atoms to the unconstrained equilibrium bond length with Fe, which is smaller. As a result, the overlap between the Fe 3d and N 2p orbitals is reduced. This is reflected in the smaller hybridization of the HOMO, i.e. 48% Fe 3d and 10% N 2p in FeCO-OEP versus 31% Ru 4d and 15% N 2p in RuCO-OEP, with the remaining contribution from other orbitals. Note that in both cases the metal atom is displaced from the N plane due to the axial ligand, Fe by 0.15 Å and Ru by 0.19 Å.

Shifts at the C 1s Edge

The shifts at the C 1s edge are smaller than those at the N 1s edge due to the increased distance of the C atoms from the metal. The binding energy of the C 1s core level increases when going from Ru to Fe in the three-dimensional molecules, but it decreases in the two-dimensional OEP. This difference is most likely due to changes in the C 1s binding energy, since different π^* transitions are shifted by the same amount. A smaller contribution might

Table 3.3: Calculated N 1s-to-π^* Transition Energies for Ru- and Fe-OEPs. The results for the N 1s core level and the LUMO are obtained relative to the vacuum level from a transition state calculation (with 1.5 electrons in the N 1s core level), while the N 1s-to-π^* transition is obtained from a ΔSCF calculation. The N charge has been obtained using the Bader analysis.[93]

Molecule	N 1s-to-π^* [eV]	LUMO [eV]	N 1s energy [eV]	N charge (per atom) [e]	Electron-core hole interaction [eV]
RuCO-OEP	402.56	-2.62	-405.20	-0.959	3.16
FeCO-OEP	402.63	-2.65	-405.38	-0.954	3.18
RuCl-OEP	402.53	-2.62	-405.17	-0.970	3.16
FeCl-OEP	402.50	-2.66	-405.24	-0.962	3.17

come from change in the energy of the unoccupied orbitals due to the different structure of the OEPs. Like for the N 1s spectrum of H_2-OEP, the structure of the C 1s spectrum differs from those of the metal OEPs because of the inequivalent N species, which produce inequivalent C species. In all the dye molecules, the C atoms are farther from the metal than the N atoms and therefore less affected by going from Ru to Fe. Therefore, we do not attempt to provide an in-depth explanation of the C 1s shifts. We only comment on the smaller shift of the C 1s-to-π^* transitions from Ru to Fe in tris(phenanthroline) compared to tris(bipyridine) molecules. This could be due to higher delocalization of the LUMO in the larger π system of phenanthroline.

3.5 Conclusions

In summary, we have investigated differences in the electronic structure of Ru- and Fe-based dyes, in order to find out whether it might be possible to replace Ru by Fe in solar cell applications. A consistent trend is observed in the N 1s X-ray absorption spectra of three-dimensional cage molecules, where the N 1s-to-π^* transition shifts down in energy, and the C 1s-to-π^* transition shifts up when going from Ru to Fe. This trend is explained by a charge transfer between the metal and the surrounding N ligands using DFT calculations.

Fe transfers more negative charge to its N ligands than Ru. Smaller and less uniform effects are observed for planar cages. Calculations reveal a delicate balance between several driving forces, such as the oxidation state, the crystal field, the presence of axial ligands, and the delocalization of the π system.

The next step in this quest for inexpensive Fe-based dye molecules will be an investigation of the electronic states at the Fe atom, particularly the 3d valence states. The empty part can be probed by X-ray absorption spectroscopy at the Fe 2p edge, which exhibits a rich manifold of sharp Fe 2p-to-3d transitions.[89, 94] Such a study should be able to address how the cage structure of the Fe atom affects its 3d manifold via the crystal field splitting. That in turn controls the stability of the dye molecules against oxidation, which is one of the major issues with Fe-based molecules.

Another direction would be to test Ru- vs. Fe-based dyes in dye sensitized solar cells or their components. Particularly interesting would be the influence of the observed energy level shifts on the electronic properties, such as internal quantum efficiency and back electron transfer.

Chapter 4

Crystal Fields of Transition Metal Poprhyrins and Phthalocyanines

This work is published in P. S. Johnson, J. M. García-Lastra, C. K. Kennedy, N. J. Jersett, I. Boukahil, F. J. Himpsel, P. L. Cook, "Crystal Fields of Porphyrins and Phthalocyanines from Polarization-Dependent 2p-to-3d Multiplets," *J. Chem. Phys.* **140**, 114706 (2014).[95]

4.1 Introduction

In order to systematically design dye molecules for solar cells with optimized sunlight absorption and charge separation, it is important to control their energy levels together with the driving forces that separate electrons and holes. Typical dye molecules, such as porphyrins and phthalocyanines, contain a central 3d or 4d metal ion surrounded by an organic π system. In previous work we have used a combination of X-ray absorption spectroscopy (XAS) and first principles DFT calculations to systematically investigate their energy level structure,[96, 23] to detect the influence of axial and peripheral ligands on the energy levels,[97] to compare the level structure of Ru- and Fe-based dye molecules,[41] and

to investigate the energy levels in different parts of donor-π-acceptor complexes.[98] There is a substantial amount of literature on the characteristic multiplet structure of the 2p-to-3d transitions in such molecules.[99, 49, 100, 101, 102, 103, 104, 105, 106, 107] For Mn dye molecules specifically, see Refs. [108, 109]; Fe, Refs. [47, 110, 111, 112, 113, 114, 115, 116, 117]; Co, Ref. [118]; Ni, Ref. [119]; Cu, Refs. [120, 121]; Zn, Ref. [122]. TiO-Pcs[20, 97] and VO-Pcs[123, 124] have also been studied as possible dye molecules.

Here we focus on the crystal field generated by the negatively-charged N atoms surrounding the central metal ion of porphyrins and phthalocyanines. Usually, the HOMO is located at the metal atom and the LUMO is delocalized over the N atoms and the surrounding π-system. This results in optical transitions with charge-transfer character, which start the separation of electrons and holes. The crystal field then can either assist charge separation or suppress it. In both cases it is important to know its sign and magnitude to find ways of steering the carriers in the right direction.

The crystal field parameters of π-bonded, square planar transition metal complexes such as phthalocyanines and porphyrins are difficult to obtain from UV-visible absorption spectra, since the d-d electronic transitions are masked by stronger π-π^* transitions, as well as metal-ligand or ligand-metal charge transfer bands.[125, 126, 127] As a result, a search for published values of crystal field parameters from optical spectroscopy did not produce any results for the molecules investigated here. As stated in a review of UV-visible absorption spectra of phthalocyanines and porphyrins[125]: "Despite the large number of spectra that have been measured and analyzed since the 1970s, a complete model that could accurately account for all optical properties of even just the $\pi \rightarrow \pi^*$ and $n \rightarrow \pi^*$ transitions of the phthalocyanine ring is not available."

Our approach is based on the fine structure of the 2p-to-3d core-to-valence transitions of the 3d transition metal series. These transitions are highly dipole selective toward 3d final states, thereby eliminating competing transitions involving π^* orbitals. The multiplet struc-

ture reveals both the crystal field at the transition metal atom and the Coulomb interaction between its 3d electrons. This has been amply demonstrated in previous work,[112, 128, 94] and codes have been developed to calculate the full multiplet structure originating from the crystal field plus the Coulomb/exchange interaction between the 3d valence electrons and the 2p core hole.[128, 129, 94]

In addition, we use the polarization dependence of the multiplet intensities from molecular films oriented by the substrate (compare Refs. [103, 100, 118, 116, 47, 101, 104, 120, 130]). This doubles the experimental information and strongly constrains the crystal field parameters. The extra information is particularly important when going from the frequently-studied octahedral O_h symmetry to planar molecules with lower symmetry, here D_{4h}. These require two additional parameters Ds and Dt in addition to the octahedral crystal field parameter 10Dq, which generate many possible combinations including false minima. Even with the extra polarization information, the high sensitivity of the multiplet structure to small deviations in the crystal field parameters and the assumed ground state requires extra information for a unique fit. We found it highly advantageous to have DFT calculations for several exchange/correlation potentials available to obtain reliable starting values of the crystal field parameters.

As a result of the combined XAS and DFT study we present systematic crystal field parameters for phthalocyanines and octaethylporphyrins involving the transition metals from Mn though Ni. These provide the starting point for designing dye molecules that optimally separate electrons and holes via the crystal field.

4.2 Experimental

Sample preparation and characterization

Iron(II) phthalocyanine (Fe-Pc), cobalt(II) phthalocyanine (Co-Pc), nickel(II) phthalocyanine (Ni-Pc), manganese(III) octaethylporphyrin chloride (MnCl-OEP), cobalt(II) octaethylporphyrin (Co-OEP), and nickel(II) octaethylporphyrin (Ni-OEP) were purchased from Sigma-Aldrich and used as received. In order to obtain the best quality spectra (with the narrowest peaks and largest peak-to-valley ratios), the molecules in this study were outgassed and sublimed in situ onto either Si substrates with native oxide or Au. Sublimation of these molecules also ensured that they were in the appropriate oxidation state by removing adsorbates loosely bound to the metal atom. Sublimation temperatures (to within 10 °C) were 445 °C for Fe-Pc, 460 °C for Co-Pc and Ni-Pc, and 250 °C for Co-OEP and Ni-OEP. Mn-OEP was prepared by sublimation of MnCl-OEP at 455 °C, above the typical OEP evaporation temperature of 250 °C. At this higher temperature, the axial Mn-Cl bond was broken for most of the molecules and Cl desorbed. Sample integrity was monitored by checking N 1s spectra of each sample for a characteristic peak just below 400 eV which corresponds to a broken phthalocyanine or porphyrin ring.[41] No such peaks were observed for the sublimed samples. Typical N 1s spectra are shown in Figure 4.1 and will be discussed in greater detail in a later section.

The polarization dependence of the N 1s spectra of Fe(II)-Pc in Fig. 4.1 provides quantitative information about the orientation of the deposited films.[96, 47, 104, 105, 116, 101] The N 1s edge of transition metal phthalocyanines is influenced by the nature of the central metal atom,[131] but we do not focus on these effects here as they do not strongly affect use of the N 1s edge as a probe of molecular orientation. Well-ordered films were obtained on Si wafers covered with the native oxide, a widely used substrate. In that case the Pc molecules were preferentially oriented with their molecular planes perpendicular the substrate and the

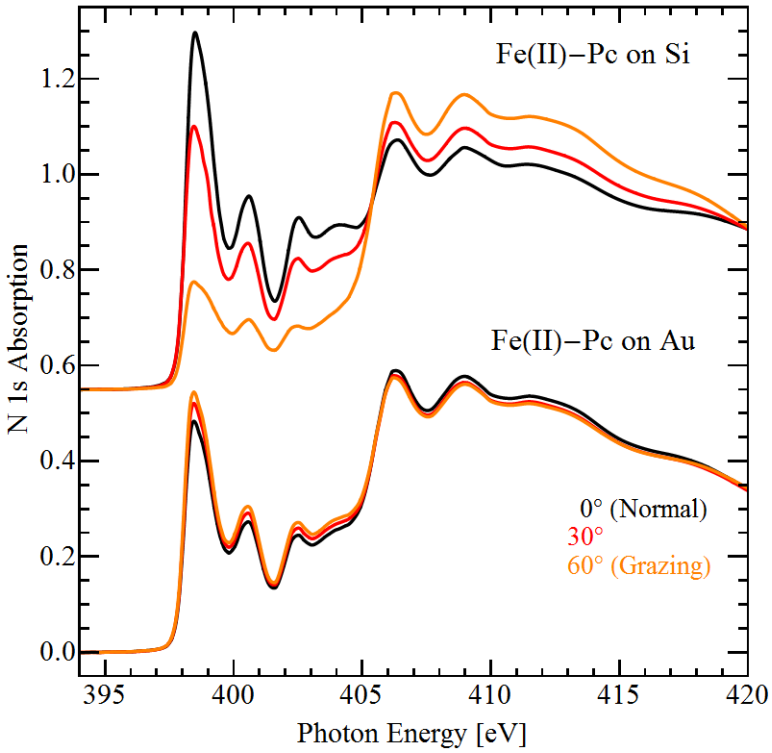

Figure 4.1: *Polarization-dependent N 1s spectra of Fe(II)-Phthalocyanine on Au and oxidized Si substrates.*

N 1s spectra of Fe(II)-Pc sublimed onto oxidized Si and Au substrates. The polarization dependence of the spectra indicates that Fe(II)-Pc stands up on Si and lies flat on Au. The much lower modulation on Au is consistent with a nearly random orientation. Therefore Si substrates were chosen for determining the crystal field parameters of the molecules.

OEP molecules parallel to it. The film thickness played a role in optimizing the polarization dependence. Typically, the best polarization dependence is seen in films a few layers thick, but not thick enough to be visible (compare Ref. [130]). Films with visible color still show polarization dependence in their spectra, but it is reduced compared to thinner samples because of disorder from surface nonuniformity. Polarization-dependent N 1s spectra for Co(II)-Pc, Co(II)-OEP, Ni(II)-Pc, and Ni(II)-OEP can be found in the Supplementary Information. The Supplementary Information also contains plots of the LUMO peak inten-

sity versus $cos^2\theta$. The slope of these curves is a measure of the degree of orientation. For Au substrates the polarization dependence was much weaker, as shown in the bottom half of Fig. 4.1. A likely explanation for the disorder present in the films on air-exposed Au substrates is their inhomogeneous nature. While the initial few layers are well-ordered and lie flat on a clean surface, additional layers see a much rougher surface which causes them to stand on edge.[130] Therefore the silicon substrates with their native oxide were chosen for determining the crystal field parameters. They also more closely resemble substrates in actual devices.

X-ray absorption measurements

X-ray absorption measurements for all molecules were performed at the U2 VLS-PGM beamline at the SRC. Additional measurements of Ni(II)-Pc for higher resolution spectra were performed at Beamline 8.0 at the ALS. All spectra were taken in surface-sensitive total electron detection mode. The energy calibration of the metal 2p spectra was based on published data,[96] and that of the N 1s spectra was obtained from the second order Ni 2p edge of a Ni mesh. Radiation damage was minimized by using the narrowest possible exit slits. The absolute accuracy is about ± 0.2 eV, the relative accuracy for the same edge of different compounds about ± 0.1 eV, and the relative accuracy within a spectrum about ± 0.05 eV.

Density functional theory

Density Functional Theory (DFT) calculations were performed by Juan Maria García-Lastra of the Department of Energy Conversion and Storage at the Technical University of Denmark.

DFT calculations were performed by means of the Amsterdam Density Functional (ADF) code, version 2012.01 (Ref. [90]). All atoms were described through basis sets of TZP quality (triple-ζ STO plus one polarization function) given in the program database, including all

the core electrons in the calculation (i.e. with no frozen core approximation). Spin-polarized calculations were carried out using three levels of approximation for the exchange-correlation potential, namely: i) local density approximation (LDA) employing the Vosko-Wilk-Nusair (VWN) functional[91], ii) general gradient approximation (GGA) using the Perdew-Burke-Ernzerhof (PBE) functional[132], iii) a hybrid scheme mixing GGA and exact Hartree-Fock exchange with the so-called BHandHLYP functional.[90] In a first step we calculated the ground state geometries of all the compounds studied in the present work. The corresponding occupations of the d-orbitals for the ground state of each compound are the following: i) Ni(II)-Pc and Ni(II)-OEP $[(xy)^2\ (xz)^2\ (yz)^2\ (3z^2-r^2)^2\ (x^2-y^2)^0]$; ii) Co(II)-Pc and Co(II)-OEP $[(xy)^2\ (xz)^2\ (yz)^2\ (3z^2-r^2)^1\ (x^2-y^2)^0]$; iii) Fe(II)-Pc $[(xy)^2\ (xz)^1\ (yz)^1\ (3z^2-r^2)^2\ (x^2-y^2)^0]$; iv) Mn(II)-OEP $[(xy)^1\ (xz)^1\ (yz)^1\ (3z^2-r^2)^1\ (x^2-y^2)^1]$. Secondly we used an "Average of Ocupations" (AOC) procedure to evaluate the corresponding crystal field parameters of each system. In the AOC procedure the d-electrons are equally distributed over the five d-orbitals (e. g., for Ni-Pc the occupations were $(xy)^{1.6}\ (xz)^{1.6}\ (yz)^{1.6}\ (3z^2-r^2)^{1.6}\ (x^2-y^2)^{1.6}$), while the geometry of the molecule was fixed to that of the ground state. Crystal field parameters could then be obtained simply by taking the Kohn-Sham energies of the d-orbitals. This AOC technique has been shown to be accurate for the crystal field splitting of many other transition metal complexes.[133, 134]

The crystal field parameters 10Dq, Ds, and Dt can be used to calculate the 3d manifold in the one-electron picture,[80, 97] as shown in Figure 4.2. We do not include the electron occupancy of the orbitals here, because the crystal field is not the only factor determining the total energy. The Coulomb/exchange energy among the 3d electrons is at least as important. There also remain some questions regarding the ground state configurations of Pcs, particularly Fe(II)-Pc.[110, 99, 111, 49, 100, 101, 102, 103, 112, 105, 113, 115] The octahedral crystal field 10Dq splits the 3d level into a doubly-degenerate e_g level and a triply-degenerate t_{2g} level, both of which are then split further by the tetragonal distortion of the

crystal field in planar, four-fold molecules. For Figure 4.2 we have already used the fully-optimized parameters, thereby providing an overview of the results from our work. Since the Coulomb/exchange interaction between the 3d electrons is comparable to the crystal field splitting, care has to be taken not to overinterpret such diagrams. For example, the actual multiplets consist of typically 10-100 lines with varying parentage (see the discussion below). They reflect many-electron states which cannot be represented in a single-electron picture. Nevertheless, the one-electron picture has been used widely as a first approximation to describe 3d-levels in transition metal oxides.

Multiplet calculations and fitting

Before getting into the details of calculating the observed 2p-to-3d multipets, it is worth discussing their connection with the crystal field, both in the ground state and the excited state. The 2p core hole introduces a major perturbation in the 3d electron manifold by its extra positive charge (which lowers all the 3d levels) and by its Coulomb/exchange interactions with the 3d electrons. In addition, an extra electron is generated by the optical absorption process, which interacts with all the 3d electrons. Despite these radical changes in the 3d manifold, the crystal field is not affected much, because it is caused by charges on the neighboring N atoms. In fact, the absorption of visible light in a solar cell also generates an extra electron, which makes the crystal field obtained from X-ray absorption spectroscopy more realistic than the ground state crystal field, as far as photovoltaics are concerned.

Fits of the 2p-to-3d absorption spectra are performed using the CTM4XAS atomic multiplet code.[94] Generally, a uniform reduction of the calculated crystal field parameters and Slater integrals for the Coulomb/exchange interaction provides a fairly direct route to a best fit. This is an indication that DFT calculations tend to obtain the correct ratio of the various interactions, but have difficulties describing the screening quantitatively.

Specifically, the observed $2p_{3/2}$ to 3d multiplets are calculated from the three crystal field

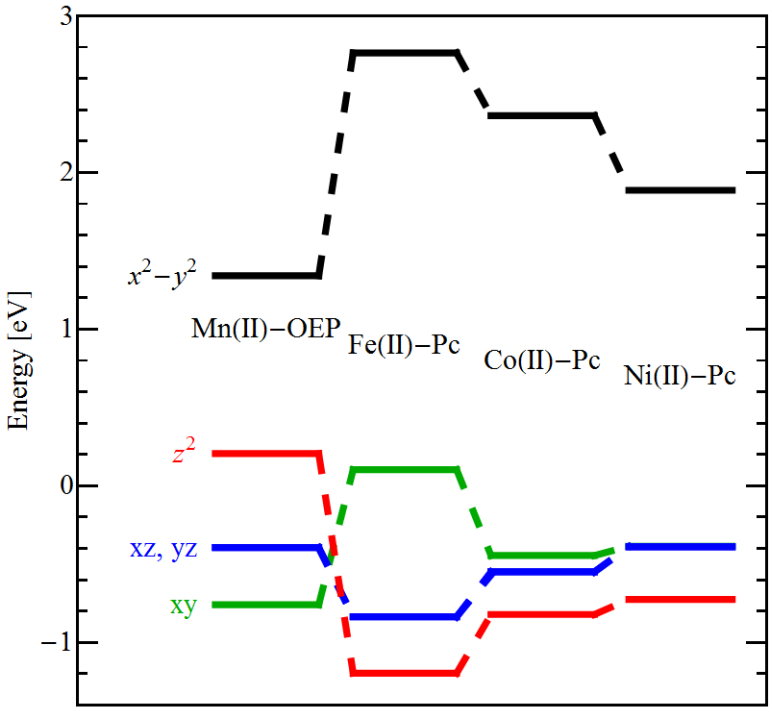

Figure 4.2: *One-electron energy levels for Mn(II)-OEP, Fe(II)-Pc, Co(II)-Pc, and Ni(II)-Pc, obtained from the optimized crystal field parameters in Table 4.2.*

The energy levels in this figure are obtained from standard crystal field theory calculations (see p.47 in [80]). While one must also take into account the electron-electron interaction for determining the total energy and the ground state, the estimate for the energy level structure provided by just the crystal field is suitable for testing the accuracy of the crystal field parameters. This can be checked by verifying that the symmetry of the transitions matches the symmetry of the levels in this one-electron picture when molecular orientation is taken into account.

Table 4.1: Crystal field parameters for Fe-Pc produced by several different functionals.

Functionals	10Dq	Dt	Ds
LDA	3.65	0.329	0.608
PBE	2.94	0.257	0.597
BHandHLYP	2.54	0.237	0.446

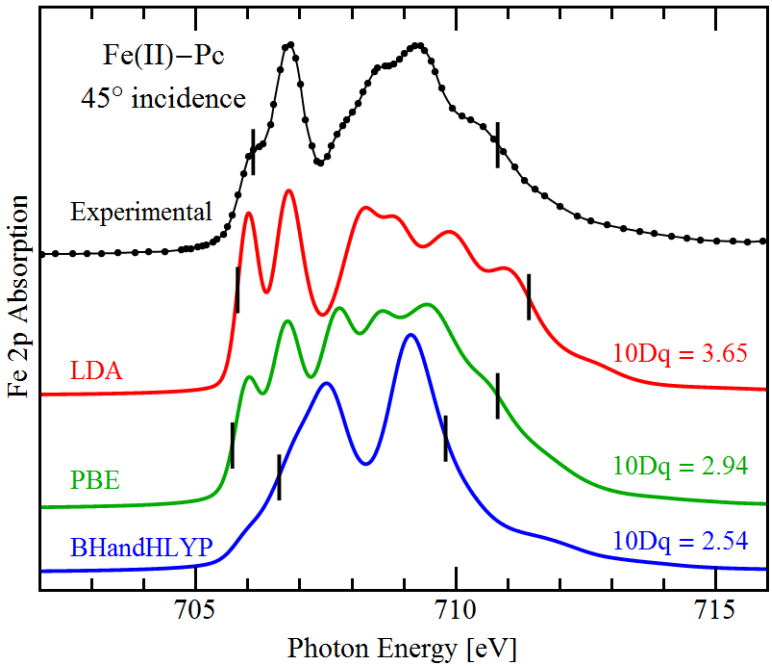

Figure 4.3: *Comparison of the experimental spectrum of Fe(II)-Pc at 45° incidence and calculated spectra using several different functionals (see Table 4.1 for details).*

Black lines indicate the FWHM of the $2p_{3/2}$ region and show how 10Dq influences the overall width by splitting the 3d-level. The PBE functional provides the most accurate width and is used as the starting point for optimizing the crystal field parameters.

parameters in D_{4h} symmetry, 10Dq, Ds, and Dt, together with atomic Slater integrals using CTM4XAS,[94] which is based on Cowan's atomic multiplet code[135] with modifications by Butler[136], Thole et al.[112], and Ogasawara et al.[137] incorporating charge transfer and crystal field effects. As an example, the Fe(II)-Pc spectra corresponding to the crystal fields obtained from the three DFT functionals are shown in Figure 4.3. The corresponding parameters are given in Table 4.1. The Slater parameter was set to 1 for all spectra.

There are substantial differences between the functionals, which can be traced to different values of the dominant crystal field parameter 10Dq. As the crystal field increases, the full width half maximum of the $2p_{3/2}$ manifold increases, which is indicated by tick marks in Fig. 4.3. Comparing the widths of the calculated spectra with the experimental width, the PBE functional comes closest to the data, an observation that holds for the other molecules as well. To obtain optimal fits, the PBE crystal field parameters need to be reduced slightly. This was corrected by uniformly reducing all crystal field parameters for each molecule (typically between 5% and 30%). In some cases it was necessary to fine tune the ratios of the crystal field parameters (in particular to move the third peak of the PBE spectrum in Fig. 4.3 to higher energy), but we kept such deviations from the calculated ratios to a minimum.

The rationale for this strategy was that DFT calculations do not account completely for screening which reduces electrostatic interactions. The Slater integrals could be affected by the localization of the 3d states in the presence of the core hole, as discussed previously.[138, 139] The degree of covalency together with the appearance of ligand holes may also be a factor. Therefore we investigated the rescaling of the Slater parameters and the crystal field parameters independently of each other. The corresponding figures are included in the Supplementary Information. These figures also establish the margins of error for the crystal field and Slater parameters.

More generally, a core level transition represents a highly excited state, which raises the question of how much the presence of the core hole distorts the ground state electronic structure of the valence electrons. The presence of the core hole is included in the multiplet calculations,[135] but the localization of the 3d-electrons induced by the 2p core hole will affect the Slater parameters. The crystal field is affected less by the core hole, since it originates from neighboring N atoms, not the metal itself. It would be desirable to have crystal field parameters available from UV-visible spectroscopy, where the core hole is absent.

These are difficult to obtain due to the dominance of transitions involving π levels.[125, 126, 127] There are optical data available for octahedral Mn complexes that do not contain π orbitals. A comparison with core level absorption[138] shows a reduction of 10Dq by about 0.2 eV in the presence of a core hole.

In order to model the polarization dependence of the spectra, it is important to appropriately scale the oscillator strengths of the in-plane and out-of-plane transitions produced by the multiplet calculations. The Pc and OEP molecules were found to have orientations roughly orthogonal to each other on oxidized Si substrates. Therefore we calculated the polarization dependence for two different orientations of the planar molecules: one for lying on edge, the other for lying flat. For molecules lying on edge, the intensity of the spectrum at a given energy is

$$I_{\perp} = \frac{1}{2}\left[Zcos^2\theta + R\left(2 - cos^2\theta\right)\right] \tag{4.1}$$

where Z is the oscillator strength of the out-of-plane transitions, R is the oscillator strength of the in-plane transitions (note that for our purposes R and L polarizations are identical), and θ is the angle of incidence measured from normal to the substrate. For molecules lying flat one obtains:

$$I_{\parallel} = Z\left(1 - cos^2\theta\right) + Rcos^2\theta \tag{4.2}$$

with the same assignments. In each case it is assumed that the molecules are azimuthally disordered but with no tilt from either normal or parallel to the surface, respectively.

The difference between the two situations can be rationalized by considering the available transitions at normal (0°) and extreme grazing (90°) X-ray incidence. At normal incidence, both in-plane and out-of-plane transitions are allowed for azimuthally disordered molecules lying on edge, while molecules lying flat exhibit only in-plane transitions. At grazing incidence the allowed transitions are only in-plane for molecules lying on edge and out-of-plane transitions for molecules lying flat. Between these extreme cases the oscillator strengths have the $cos^2\theta$ dependence of optical dipole transitions

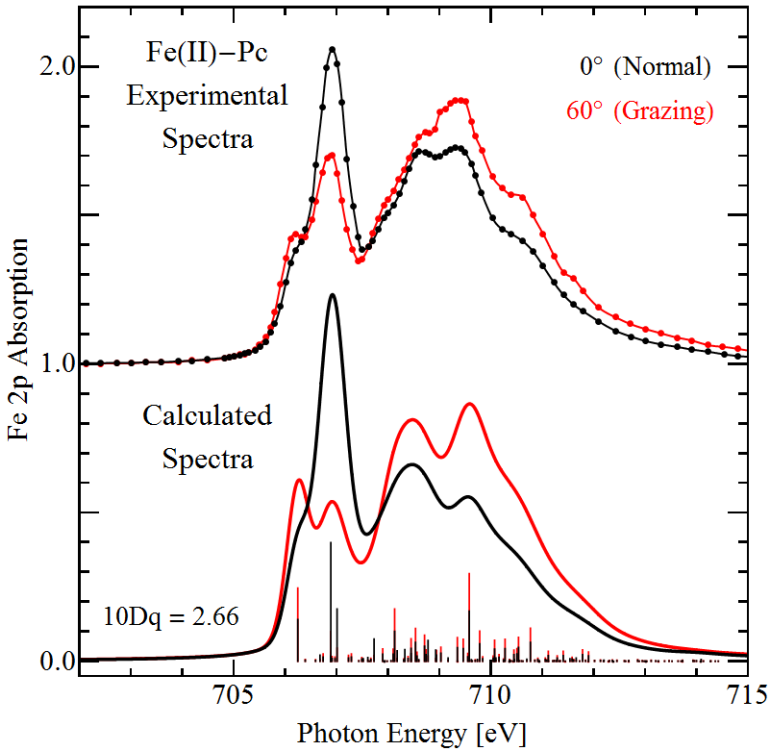

Figure 4.4: *Comparison of experimental and calculated spectra for Fe(II)-Pc at normal and grazing incidence.*

The peak energies are reproduced in the calculated spectra, but the experimental polarization dependence is smaller due to imperfect orientation. Features seen strongly at normal incidence have out-of-plane symmetry, and those stronger at grazing incidence in-plane symmetry.

4.3 Results

The calculated spectra in Figs. 4.4-4.8 come from multiplet calculations using crystal field parameters determined by DFT calculations. Polarization dependence calculations for the Pcs and OEPs have been applied to the transition intensities calculated by CTM4XAS to account for the ordering of the molecules and their orientation on the substrate. Each transition is simulated by a Voigt profile with area equal to the oscillator strength calculated by CTM4XAS and linearly increasing broadening going to higher energies. The calculated

spectra assume that the molecules are perfectly ordered and oriented exactly normal (for Pcs) or parallel (for OEPs) to the surface. They will thus exhibit stronger polarization dependence than the experimental spectra, which are somewhat disordered and tilted from normal or parallel orientations. The lines under the calculated spectra indicating transition oscillator strengths are scaled for their respective angles of incidence. The strong calculated polarization dependence shows that for a perfectly ordered film aligned perpendicular (for Pcs) or parallel (for OEPs) to the substrate, a much more dramatic effect could be observed. The crystal field parameters used for the calculated spectra in Figs. 4.4-4.7 are listed in Table 4.2.

The metal 2p absorption edges determine the crystal field, and the polarization dependence of the spectra is particularly important for uniquely determining the crystal field parameters. Figure 4.4 compares Fe $2p_{3/2}$ absorption spectra for Fe(II)-Pc with atomic multiplet calculations for two polarizations (red and black). The Fe $2p_{1/2}$ region is omitted because its features are not as well defined. Overall, theory and experiment exhibit similar multiplet structures with comparable polarization dependence. The peak near 707 eV is strongest at normal incidence, which indicates that the corresponding 3d orbitals have an out-of-plane orientation, because the Pc molecules lie on edge according to the N 1s data in the Supplementary Information. A secondary peak on the lower energy side of the main peak has opposite polarization dependence and thus corresponds to an orbital with in-plane symmetry. The higher energy peaks likewise have opposite polarization dependence corresponding to 3d orbitals with in-plane orientation. The modulation of the spectra in this region is reduced compared to the modulation at lower energies. The symmetries of the transitions in these spectra are consistent with a previously reported spin 1 ground state[110, 99, 111, 49, 100, 101, 102, 103, 112, 105, 113, 115] which leaves the $d_{xz,yz}$, and d_{xy} orbitals partially filled, thus transitions into each are allowed. While there remain questions over the electron occupancy of the ground state of the Fe^{2+} ion in Fe(II)-Pc, the polariza-

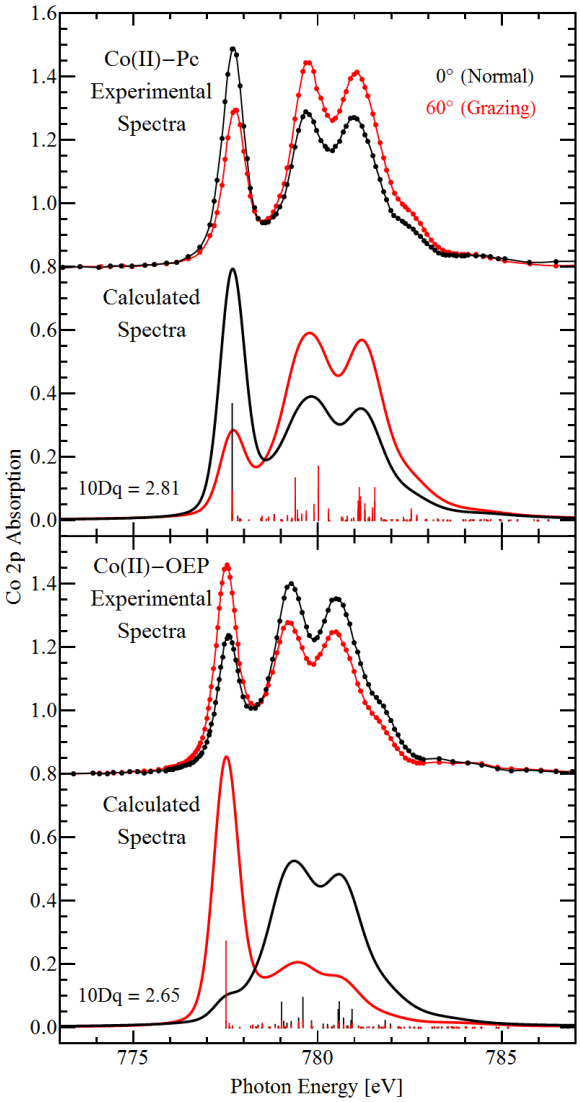

Figure 4.5: *Experimental and calculated Co 2p absorption spectra for Co(II)-Pc and Co(II)-OEP.*

Pc and OEP films have opposite polarization dependence, indicating that Pcs preferentially stand on edge while OEPs lie flat. Compared to Fe(II)-Pc, the lower number of unoccupied 3d states reduces the number of strong transitions in the multiplet.

tion dependence seen in these spectra potentially offers clues to the available orbitals in the excited state.

The same polarization dependence pattern can be seen in the Co $2p_{3/2}$ spectra of Co(II)-

Pc in Figure 4.5 (top panel). Again the low-energy peak is strong at normal incidence, and the higher-lying peaks are strong at grazing incidence. The total number of transitions in Co-Pc spectra is lower than for Fe-Pc because of the extra d electron in the Co^{2+} ground state. Thus fewer unoccupied levels are available for the excited electron, notably the loss of the lower energy shoulder on the dominant peak and fewer transitions in the higher energy region. The ground state of Co^{2+} in these molecules is spin $\frac{1}{2}$.[99, 118, 49, 100, 105, 102, 103] Co 2p spectra of Co(II)-OEP are also shown in the bottom panel of Figure 4.5. They have similar multiplet structure to Co(II)-Pc but opposite polarization dependence. This is in line with the opposite orientation of OEP compared to Pc molecules observed at the N 1s edge in the Supplementary Information. OEP lies flat on the SiO_2 substrate rather than on edge.

In the Ni $2p_{3/2}$ spectra of Figure 4.6 the multiplet is reduced to a single, dominant line with weak features at higher energy (compare Fig. 4.7 for a higher resolution spectrum measured at the ALS). This continues the trend towards fewer available empty levels when going from Fe to Co and Ni. In Ni, only the highest-lying e_g level remains unoccupied and thus dominates the spectra. The polarization dependence of this peak is opposite to that of the low-energy peak of the Fe 2p and Co 2p spectra in Fig. 4 and Fig. 5. This is because the out-of-plane d_{xz} and d_{yz} orbitals have now become filled[99, 119, 49, 100] (thus Ni^{2+} has a spin 0 ground state), leaving only the in-plane $d_{x^2-y^2}$ orbital available for the excited 3d electron (see Fig. 4.2). The dominant Ni 2p transition thus corresponds to the higher energy transitions in the Fe 2p and Co 2p spectra. The orientation of the molecules has not changed according to the N 1s spectra in the Supplementary Information, as expected. Ni-Pc and Ni-OEP spectra have again opposite polarization dependence, which is consistent with their opposite orientation. The high-resolution spectrum in Fig. 4.7 shows a clearly-resolved doublet above the main peak for Ni-Pc, which is just a single peak at 855.5 eV in Ni-OEP (Fig. 4.6) and in the multiplet calculation. This is in agreement with previous

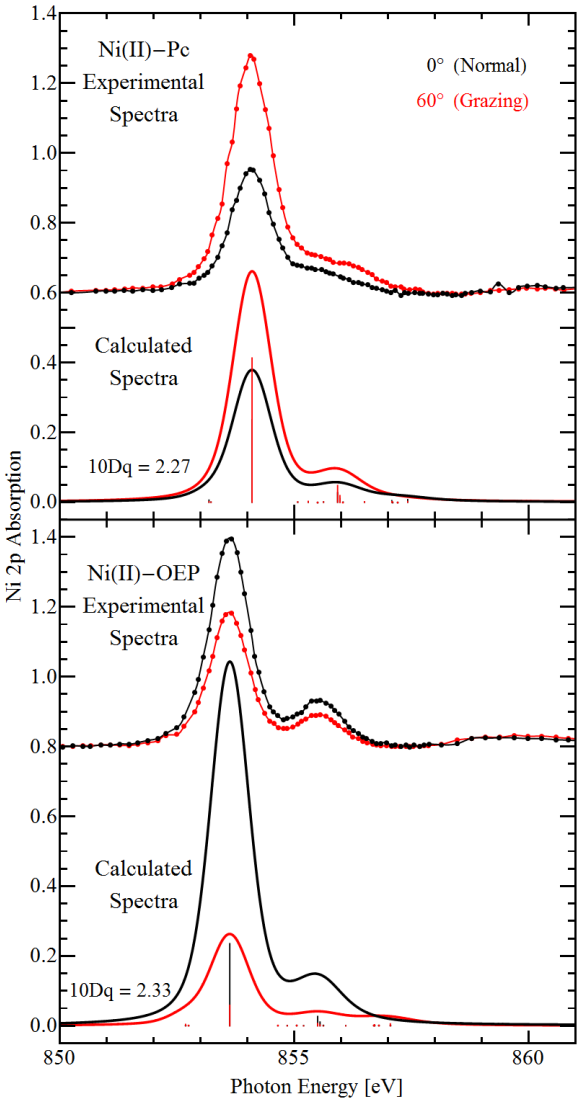

Figure 4.6: *Experimental and calculated Ni 2p absorption spectra for Ni(II)-Pc and Ni(II)-OEP.*

As with Co(II)-Pc and Co(II)-OEP, the Pc and OEP have opposite polarization dependence. For Ni(II)-Pc and Ni(II)-OEP all levels except for the highest lying e_g level are occupied, such that all transitions have the same polarization dependence. They correspond to the higher energy transitions in Figures 4.4 and 4.5.

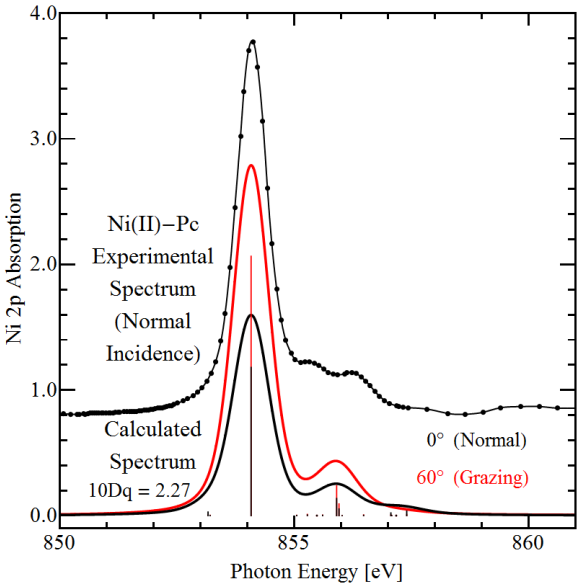

Figure 4.7: *Higher resolution spectrum from a thicker sample of Ni(II)-Pc, which showed lower polarization dependence.*

The calculation shows a single peak above the main peak (as in Ni-OEP), which is split in the experimental spectrum.

work.[119, 96] The splitting is not unexpected, given the more complex structure of a Pc with its two inequivalent rings of N atoms surrounding the metal. A possible reason for the absence of the splitting in the multiplet calculation is the omission of ligand hole transitions.

To extend the systematics of the crystal field splitting towards the left of the 3d transition metal series we have also investigated the Mn 2p edge of Mn(II)-Pc, even though we were not able to obtain oriented films from either Mn-Pc or Mn-OEP. Figure 8 shows the experimental and calculated spectra for a sample of Mn(II)-OEP that did not exhibit polarization dependence, which shows that the molecules have no preferential orientation on the surface, likely due to the thickness of the samples as well as some possible decomposition from the higher sublimation temperature. As with the other OEPs, the calculated red and black spectra in Fig. 4.8 represent normal and grazing incidence, assuming a perfectly ordered sample with all Mn(II)-OEP molecules lying flat on the substrate. In addition, a spectrum calculated for

Table 4.2: Crystal field parameters produced by DFT calculations and experimental fitting (see Figs. 4.4-4.8 for the corresponding spectra). (PBE) indicates the calculated parameters before rescaling.

	10Dq (±0.05)	Dt (±0.005)	Ds (±0.005)	Slater integral prefactor (±0.05)
Mn-OEP	2.10	0.139	0.110	0.72
(PBE)	2.59	0.232	0.443	
Fe-Pc	2.66	0.232	0.700	0.9
(PBE)	2.94	0.257	0.597	
Co-Pc	2.96	0.276	0.496	0.95
(PBE)	3.12	0.290	0.522	
Co-OEP	2.65	0.247	0.444	0.85
(PBE)	2.91	0.281	0.422	
Ni-Pc	2.27	0.224	0.374	0.75
(PBE)	3.03	0.298	0.498	
Ni-OEP	2.33	0.230	0.383	0.77
(PBE)	2.85	0.261	0.333	

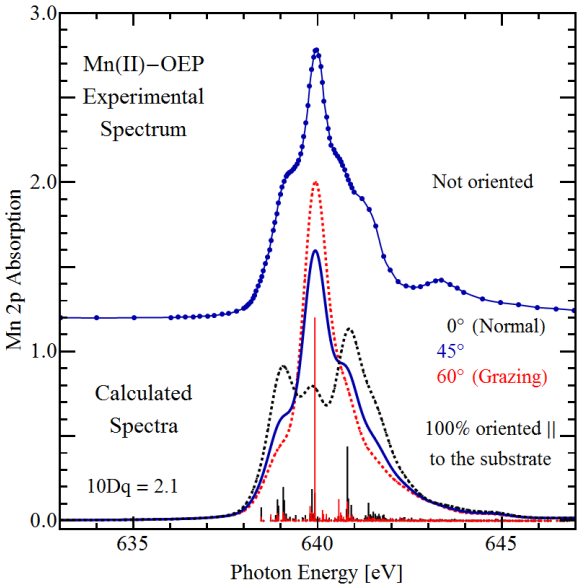

Figure 4.8: *Experimental and calculated spectra for Mn(II)-OEP.*

The data are from a thick sample, in which the molecules are no longer ordered. Such a disordered situation is comparable to a spectrum calculated for a 45° incident angle when averaging over the angular dependence. Dramatic changes in the shape of the calculated spectra with the polarization angle might explain the large variation of relative peak heights observed in Mn-OEP from differently prepared samples.

45° incidence is shown in blue, which corresponds to randomly-oriented molecules. It proves to be the best match to the experimental spectrum. The dramatic difference between the spectra at normal and grazing incidence is particularly noteworthy, as it could potentially be mistaken for mixing with other oxidation states of Mn. This is of particular concern for Fe- and Mn-based molecules, which occur in both the 2+ and 3+ oxidation states.[96] For example, the oriented Mn(II) spectrum calculated for normal incidence resembles the spectrum of Mn(III) in random orientation (compare Refs. [140, 96, 108, 138]).

The crystal field parameters obtained for Mn(II)-Pc in Table 4.2 produce a cystal field splitting in Figure 4.2 that differs substantially from those of Fe, Co, and Ni. This indicates that the 3d electron chemistry changes near the middle of the 3d transition metal series. A possible cause might be the drop in electronegativity from Fe to Mn, which stabilizes higher oxidation states for Mn. Indeed, the 3d metals to the left of Mn in the periodic table are only found in oxidation states higher than the 2+ oxidation state investigated here. While a comparable analysis of the crystal field has not been performed for Cr- and V-based porphyrins[124, 123] and phthalocyanines, there are crystal field parameters available for TiO(IV)-phthalocyanines.[20, 97] To be in the stable 4+ oxidation state, Ti-based phthalocyanines require additional axial ligands. Those affect the ordering of the $x^2 - y^2$ and z^2 levels, depending on the detailed arrangements of the axial ligands (see Fig. 7 in Ref. [97]).

4.4 Conclusions

This work investigates the trend of the crystal field splitting along the row of 3d transition metal phthalocyanines and porphyrins, in order to systematically improve dye molecules for solar cells. Polarization-dependent X-ray absorption spectroscopy, DFT, and multiplet calculations are used to determine the crystal field parameters 10Dq, Ds, and Dt. The

detection of the polarization dependence of the 2p-to-3d multiplets is found to be very valuable for an unambiguous determination of the crystal field parameters. It provides both a scaling factor for calculated crystal field parameters and the symmetry of the transitions. Several DFT functionals were tested, and the PBE functional was found to be closest to the optimum fit. The PBE crystal field parameters still must be reduced somewhat, typically 5%-30%. Nevertheless, the DFT calculations are essential for producing accurate ratios of the crystal field parameters and thereby greatly reducing ambiguities in choosing starting values for the fit parameters. Additionally, DFT calculations are needed for an accurate picture of ground state electron occupancy, which determines the partially-filled or empty states that are available for optical transitions.

This analysis reveals systematic trends in the splitting of the 3d levels for transition metal phthalocyanines and porphyrins in the 2+ oxidation state. The cross-over to transition metals with higher oxidations states to the left of Mn is discussed as well. Understanding the systematics of the crystal field in such metal-organic dye molecules is essential for steering photoexcited electrons in the right direction for optimal charge separation in solar cells.

Chapter 5

Conclusion and Future Directions

Solar power has great potential to alleviate the growing energy crisis and is seeing more widespread use and investment with each year. Efforts at improving cost efficiency are focused on reducing the price of high end solar cells and improving the efficiency of low end solar cells. This latter goal is accomplished by combining spectroscopy, theoretical analysis, synthesis, and practical testing to accelerate development. Spectroscopy and theoretical analysis are necessary for determining the electronic structure of the dye, donor, and acceptor, which determine the photovoltage and photocurrent of the cell, and ultrafast pump-probe spectroscopy can determine excited state lifetimes and relaxation rates.

While no single spectroscopic technique can provide a full picture of the electronic structure of the solar cell's components, X-ray absorption spectroscopy reveals molecular orientation and unoccupied energy levels, which are particularly important for the dye and acceptor to direct charge movement. The sensitivity of X-ray absorption spectroscopy to the orientation of both the molecule and orbitals involved in relevant transitions provides a critical additional piece of information in characterizing the electronic structure of transition metal dyes. Combining the information gained from X-ray absorption spectroscopy with first-principles calculations should allow for better informed predictions of dye and acceptor

designs which would improve solar cell performance.

The focus of this work has been on the effects of replacing low abundance and thus expensive ruthenium with iron as the transition metal in solar cell dyes and on understanding the electronic structure of the transition metals in common solar cell dyes through crystal field parameters. Both of these objectives are crucial to designing better solar cells in terms of both efficiency and cost of materials. We find that the replacement of Ru by Fe in several common dye molecules causes a downward shift of several tenths of an eV in the N 1s-to-LUMO transition energy and a smaller upward shift in the C 1s-to-LUMO transition energy. The shifts are due to greater transfer of negative charge from Fe to the N ligands than from Ru, consistent with DFT calculations.

The crystal fields of porphyrin and phthalocyanine based transition metal dyes were determined using a combination of DFT and multiplet calculations and X-ray absorption spectra. The polarization dependence of X-ray absorption spectroscopy is instrumental in uniquely determining the crystal field parameters from calculations, as it provides the extra information needed to identify the symmetry of the transition metal d levels. It was found that the calculated crystal field parameters need to be uniformly scaled down by 5-30% to accurately describe the crystal fields of the transition metal dyes.

Future directions in this work are focused on developing a thorough understanding of the properties which influence dye performance, including transition metal center, oxidation state, surrounding cage structure, axial ligands, and bonding to donor and acceptor molecules. By combining this theoretical understanding with diagnostic tools and new methods of synthesis, our aim is to more rapidly develop and test new solar cell dyes. Current prospects are studying the differences in electronic structure between two- and three-dimensional cages, donor-π-acceptor complexes which combine the three functional parts of a dye-sensitized cell in one molecule, and perovskites, a dye structure which has made recent leaps in efficiency.

Appendix A

Complete List of Projects and Publications

In addition to the work on solar cell dye electronic structure discussed in this thesis, I have had several other major projects leading to first-author publications. Stemming from radiation damage effects noticed in [87], we identified a universal radiation damage mechanism in amide molecules and proteins [27] whereby the oxygen is removed from the amide bond and, in order to repair the broken bonds, either a nitrile or imine bond was formed.

Using that work as a base, we then moved to imides, a more complicated group, in [26]. For imides, a similar radiation damage mechanism to that of amides was identified, but with additional steps dependent on the larger structure of the molecule. Additionally, I determined the critical dose for the various processes by measuring the changes in spectral peak intensities with total radiation dose.

Another set of projects came from collaborations with researchers in the departments of materials science and chemical and biological engineering. These collaborations focused on characterization of self-assembled monolayers (SAMs) on graphene or Au substrates. The orientation of a SAM is crucial to their function, and the surface sensitive, polarization-

dependent nature of XAS makes it a powerful tool for determining this orientation.

In one project, the SAMs were composed of azobenzene groups tethered to a graphene (or carbon nanotube) substrate, each with a different terminal group.[141] *The chromophores were synthesized and attached by Myungwoong Kim and Changshui Huang of Padma Gopalan's group in the Department of Materials Science and Engineering at the University of Wisconsin-Madison. The graphene was synthesized by Nathaniel S. Safron of Michael S. Arnold's group in the same department. Calculations for comparison with the experimental results were performed by Bryan M. Wong in the Departments of Chemistry and Materials Science and Engineering at Drexel University.* The azobenzene portion of the molecules will switch between *cis* and *trans* structures when exposed to UV or visible light, respectively. This switching behavior can be influenced by unintended attachment of the azobenzene to the substrate based on its terminal group, so it is important to know whether the molecules are oriented such that this is not an issue. We found that three different terminal groups had no significant differences in effect on the orientation of the azobenzene group, so choice of the terminal group can be made based on intended function rather than concerns over whether they will allow the switching behavior.

The other major collaboration has been with members of the department of chemical and biological engineering, focused on characterizing the conformation of oligo(ethylene) glycol (OEG) SAMs, the results of which have been accepted by *Langmuir*. *The SAMs were prepared by Mohit Goel of Nicholas L. Abbott's group in the Department of Chemical and Biological Engineering at the University of Wisconsin-Madison.* EG4-terminated alkenathiol SAMs on Au are of particular interest for biological engineering because of their potential for use as a test bed for biological experiments due to resisting nonspecific protein adsorption. Their resistance is however dependent on their conformation, which is not well known and depends on the humidity of their environment. In order to ultimately identify how their conformation changes with humidity, we first determined the unknown conformation of the

EG4 SAMs on Au in a dry environment by comparison to references with known conformations. By analyzing the polarization-dependent XAS spectra of each, we determined that the EG4 SAM on Au was a roughly 1:1 mixture of helical and all-trans conformations. The next step in the project requires use of a specially constructed vapor cell to be able to alter the relative humidity of the SAM's environment during measurement.

Complete list of publications written or contributed to during this thesis:

1. P. L. Cook, P. S. Johnson, X. Liu, A. Chin, F. J. Himpsel, "Radiation damage in biomimetic dye molecules for solar cells," *J. Chem. Phys.* **131**, 214702 (2009).

2. P. S. Johnson, P. L. Cook, X. Liu, W. Yang, Y. Bai, N. L. Abbott, F. J. Himpsel, "Universal mechanism for breaking amide bonds by ionizing radiation," *J. Chem. Phys.* **135**, 044702 (2011).

3. R. González-Moreno, P. L. Cook, I. Zegkinoglou, X. Liu, P. S. Johnson, W. Yang, R. E. Ruther, R. J. Hamers, R. Tena-Zaera, F. J. Himpsel, J. E. Ortega, C. Rogero, "Attachment of Protoporphyrin Dyes to Nanostructured ZnO Surfaces: Characterization by NEXAFS," *J. Phys. Chem. C* **115**, 18195 (2011).

4. P. S. Johnson, P. L. Cook, X. Liu, W. Yang, Y. Bai, N. L. Abbott, F. J. Himpsel, "Imide Photodissociation Investigated by X-ray Absorption Spectroscopy," *J. Phys. Chem. B* **116**, 7048 (2012).

5. I. Zegkinoglou, P. L. Cook, P. S. Johnson, W. Yang, J. Guo, D. Pickup, R. González-Moreno, C. Rogero, R. E. Ruther, M. L. Rigsby, J. E. Ortega, R. J. Hamers, F. J. Himpsel, "Electronic Structure of Diamond Surfaces Functionalized by $Ru(tpy)_2$," *J. Phys. Chem. B* **116**, 13877 (2012).

6. P. C. Snijders, P. S. Johnson, N. P. Guisinger, S. C. Erwin, F. J. Himpsel, "Spectroscopic Evidence for Spin-Polarized Edge States in Graphitic Si Nanowires," *New J. Phys.* **14**, 103004 (2012).

7. F. J. Himpsel, P. L. Cook, G. de la Torre, J. M. García-Lastra, R. González-Moreno, J.

H. Guo, R. J. Hamers, C. X. Kronawitter, P. S. Johnson, J. E. Ortega, D. Pickup, M. E. Ragoussi, C. Rogero, A. Rubio, R. E. Ruther, L. Vayssieres, W. Yang, I. Zegkinoglou, "Design of Solar Cells via Soft X-ray Spectroscopy," *J. Elec. Spec. Rel. Phenom.* **190**, 2 (2013).

8. E. M. Mannebach, J. W. Spalenka, P. S. Johnson, Z. Cai, F. J. Himpsel, P. G. Evans, "High Hole Mobility and Thickness-Dependent Crystal Structure in α,ω-Dihexylsexithiophene Single Monolayer Field-Effect Transistors," *Adv. Funct. Mater.* **23**, 554 (2013).

9. P. S. Johnson, P. L. Cook, I. Zegkinoglou, J. M. García-Lastra, A. Rubio, R. E. Ruther, R. J. Hamers, F. J. Himpsel, "Electronic Structure of Ru- vs. Fe-Based Dye Molecules," *J. Chem. Phys.* **138**, 044709 (2013).

10. I. Zegkinoglou, M.-E. Ragoussi, C. D. Pemmaraju, P. S. Johnson, D. F. Pickup, J. E. Ortega, D. Prendergast, G. de la Torre, F. J. Himpsel "Spectroscopy of Donor-π-Acceptor Porphyrins for Dye-Sensitized Solar Cells," *J. Phys. Chem. C* **117**, 13357 (2013).

11. D. F. Pickup, I. Zegkinoglou, B. Ballesteros, C. R. Ganivet, J. M. García-Lastra, P. L. Cook, P. S. Johnson, C. Rogero, F. M. F. de Groot, A. Rubio, G. de la Torre, J. E. Ortega, F. J. Himpsel, "Influence of Axial and Peripheral Ligands on the Electronic Structure of Titanium Phthalocyanines," *J. Phys. Chem. C* **117**, 4410 (2013).

12. E. Palacios-Lidon, D. F. Pickup, P. S. Johnson, R. E. Ruther, R. Tena-Zaera, R. J. Hamers, J. Colchero, F. J. Himpsel, J. E. Ortega, C. Rogero, "Face-Selective Etching of ZnO during Attachment of Dyes," *J. Phys. Chem. C* **117**, 18414 (2013).

13. P. S. Johnson, C. Huang, M. Kim, N. S. Safron, M. S. Arnold, B. M. Wong, P. Gopalan, F. J. Himpsel, "Orientation of a Monolayer of Dipolar Molecules on Graphene from X-ray Absorption Spectroscopy," *Langmuir* **30**, 2559 (2014).

14. P. S. Johnson, J. M. García-Lastra, C. K. Kennedy, N. J. Jersett, I. Boukahil, F. J. Himpsel, P. L. Cook, "Crystal Fields of Porphyrins and Phthalocyanines from Polarization-

Dependent 2p-to-3d Multiplets," *J. Chem. Phys.* **140**, 114706 (2014).

15. P. S. Johnson, M. Goel, N. L. Abbott, F. J. Himpsel, "Helical vs. All-Trans Conformation of OEG-Terminated Alkanethiol SAMs," *Langmuir*, Accepted (2014).

Bibliography

[1] R. Gelman, M. Meshek, S. Buchanan, and E. Augustine, "2012 renewable energy data book," tech. rep., U.S. Department of Energy, 2012.

[2] G. W. Crabtree and N. S. Lewis, "Solar energy conversion," *Physics Today*, vol. 60, pp. 37–42, 2007.

[3] K. Ardani, D. Seif, R. Margolis, J. Morris, C. Davidson, S. Truitt, and R. Torbert, "Non-hardware ("soft") cost-reduction roadmap for residential and small commercial solar photovoltaics, 2013-2020," tech. rep., National Renewable Energy Laboratory, 2013.

[4] A. Yella, H.-W. Lee, H. N. Tsao, C. Yi, A. K. Chandiran, M. Nazeeruddin, E. W.-G. Diau, C.-Y. Yeh, S. M. Zakeeruddin, and M. Grätzel, "Porphyrin-sensitized solar cells with cobalt (ii/iii)-based redox electrolyte exceed 12 percent efficiency," *Science*, vol. 334, no. 6056, pp. 629–634, 2011.

[5] C. Corrado, S. W. Leow, M. Osborn, E. Chan, B. Balaban, and S. A. Carter, "Optimization of gain and energy conversion efficiency using front-facing photovoltaic cell luminescent solar concentratordesign," *Solar Energy Materials and Solar Cells*, vol. 111, no. 0, pp. 74 – 81, 2013.

[6] B. Norton, P. C. Eames, T. K. Mallick, M. J. Huang, S. J. McCormack, J. D. Mondol, and Y. G. Yohanis, "Enhancing the performance of building integrated photovoltaics," *Solar Energy*, vol. 85, no. 8, pp. 1629 – 1664, 2011. Progress in Solar Energy 1.

[7] D. Chemisana, "Building integrated concentrating photovoltaics: A review," *Renewable and Sustainable Energy Reviews*, vol. 15, no. 1, pp. 603 – 611, 2011.

[8] B. Rezaie, E. Esmailzadeh, and I. Dincer, "Renewable energy options for buildings: Case studies," *Energy and Buildings*, vol. 43, no. 1, pp. 56 – 65, 2011.

[9] B. O'Regan and M. Graätzel, "A low-cost, high-efficiency solar cell based on dye-sensitized colloidal tio$_2$ films," *Nature*, vol. 353, pp. 737–740, 1991.

[10] S. M. Feldt, E. A. Gibson, E. Gabrielsson, L. Sun, G. Boschloo, and A. Hagfeldt, "Design of organic dyes and cobalt polypyridine redox mediators for high-efficiency dye-sensitized solar cells," *Journal of the American Chemical Society*, vol. 132, no. 46, pp. 16714–16724, 2010.

[11] H. Nusbaumer, J.-E. Moser, S. M. Zakeeruddin, M. K. Nazeeruddin, and M. Grätzel, "Coii(dbbip)$_2^{2+}$ complex rivals tri-iodide/iodide redox mediator in dye-sensitized photovoltaic cells," *The Journal of Physical Chemistry B*, vol. 105, no. 43, pp. 10461–10464, 2001.

[12] S. A. Sapp, C. M. Elliott, C. Contado, S. Caramori, and C. A. Bignozzi, "Substituted polypyridine complexes of cobalt(ii/iii) as efficient electron-transfer mediators in dye-sensitized solar cells," *Journal of the American Chemical Society*, vol. 124, no. 37, pp. 11215–11222, 2002.

[13] H. S. Jung and J.-K. Lee, "Dye sensitized solar cells for economically viable photovoltaic systems," *The Journal of Physical Chemistry Letters*, vol. 4, no. 10, pp. 1682–1693, 2013.

[14] B. E. Hardin, H. J. Snaith, and M. D. McGehee, "The renaissance of dye-sensitized solar cells," *Nature Photonics*, vol. 6, pp. 162–169, 2012.

[15] B. A. Gregg, F. Pichot, S. Ferrere, and C. L. Fields, "Interfacial recombination processes in dye-sensitized solar cells and methods to passivate the interfaces," *The Journal of Physical Chemistry B*, vol. 105, no. 7, pp. 1422–1429, 2001.

[16] T. Daeneke, T.-H. Kwon, A. B. Holmes, N. W. Duffy, U. Bach, and L. Spiccia, "High-efficiency dye-sensitized solar cells with ferrocene-based electrolytes," *Nature Chemistry*, vol. 3, pp. 211–215, 2011.

[17] Y. Bai, Q. Yu, N. Cai, Y. Wang, M. Zhang, and P. Wang, "High-efficiency organic dye-sensitized mesoscopic solar cells with a copper redox shuttle," *Chem. Commun.*, vol. 47, pp. 4376–4378, 2011.

[18] H. Tian, Z. Yu, A. Hagfeldt, L. Kloo, and L. Sun, "Organic redox couples and organic counter electrode for efficient organic dye-sensitized solar cells," *Journal of the American Chemical Society*, vol. 133, no. 24, pp. 9413–9422, 2011.

[19] M. Wang, N. Chamberland, L. Breau, J.-E. Moser, R. Humphry-Baker, B. Marsan, S. M. Zakeeruddin, and M. Grätzel, "An organic redox electrolyte to rival triiodide/iodide in dye-sensitized solar cells," *Nature Chemistry*, vol. 2, pp. 385–389, 2010.

[20] Y. Zhang, S. Wang, A. Demasi, I. Reid, L. F. J. Piper, A. Y. Matsuura, J. E. Downes, and K. E. Smith., "Soft x-ray spectroscopy study of electronic structure in the organic semiconductor titanyl phthalocyanine (tio-pc)," *J. Mater. Chem.*, vol. 18, pp. 1792–1798, 2008.

[21] N. Cai, S.-J. Moon, L. Cevey-Ha, T. Moehl, R. Humphry-Baker, P. Wang, S. M. Zakeeruddin, and M. Grätzel, "An organic d-π-a dye for record efficiency solid-state sensitized heterojunction solar cells," *Nano Letters*, vol. 11, no. 4, pp. 1452–1456, 2011.

[22] P. L. Cook, X. Liu, W. Yang, and F. J. Himpsel, "X-ray absorption spectroscopy of biomimetic dye molecules for solar cells," *The Journal of Chemical Physics*, vol. 131, no. 19, p. 194701, 2009.

[23] J. M. García-Lastra, P. L. Cook, F. J. Himpsel, and A. Rubio, "Communication: Systematic shifts of the lowest unoccupied molecular orbital peak in x-ray absorption for a series of 3d metal porphyrins," *The Journal of Chemical Physics*, vol. 133, no. 15, p. 151103, 2010.

[24] R. Kraus, M. Grobosch, and M. Knupfer, "Full electronic excitation spectrum of condensed manganese phthalocyanine," *Chemical Physics Letters*, vol. 469, no. 13, pp. 121 – 124, 2009.

[25] J. Stöhr, *NEXAFS Spectroscopy*. Springer, 1996.

[26] P. S. Johnson, P. L. Cook, X. Liu, W. Yang, Y. Bai, N. L. Abbott, and F. J. Himpsel, "Imide photodissociation investigated by x-ray absorption spectroscopy," *The Journal of Physical Chemistry B*, vol. 116, no. 24, pp. 7048–7054, 2012.

[27] P. S. Johnson, P. L. Cook, X. Liu, W. Yang, Y. Bai, N. L. Abbott, and F. J. Himpsel, "Universal mechanism for breaking amide bonds by ionizing radiation," *The Journal of Chemical Physics*, vol. 135, no. 4, p. 044702, 2011. In prior work[22, 46, 23] a 0.2 eV higher value was used for the Ti 2p reference energy for the N 1s edge. Here we use a more accurate energy calibration via the π^* transitions in N_2.

[28] F. J. Himpsel, B. S. Meyerson, F. R. McFeely, J. F. Morar, A. Taleb-Ibrahimi, and J. A. Yarmoff, *Core Level Spectroscopy at Silicon Surfaces and Interfaces*, p. 203. 1990.

[29] A. C. Thompson, D. T. Attwood, E. M. Gullikson, M. R. Howells, J. B. Kortright, A. L. Robinson, J. H. Underwood, K.-J. Kim, J. Kirz, I. Lindau, P. Panetta, H. Winick, G. P. Williams, and J. H. Scofield, *X-day Data Booklet*. Technical and Electronic Information Department, Larence Berkeley National Laboratory, 2001.

[30] F. de Groot and A. Kotani, *Core Level Spectroscopy of Solids*. CRC Press, 2008.

[31] S. T. Manson, "The calculation of photoionization cross sections: An atomic view," in *Photoemission in Solids I: General Principles* (M. Cardona and L. Ley, eds.), vol. 26, pp. 137–139, Springer-Verlag, 1978.

[32] J. A. Horsley, J. Stöhr, A. P. Hitchcock, D. C. Newbury, A. L. Johnson, and F. Sette, "Resonances in the k shell excitation spectra of benzene and pyridine: Gas phase, solid, and chemisorbed states," *The Journal of Chemical Physics*, vol. 83, no. 12, pp. 6099–6107, 1985.

[33] P. Väterlein, M. Schmelzer, J. Taborski, T. Krause, F. Viczian, M. Bäßler, R. Fink, E. Umbach, and W. Wurth, "Orientation and bonding of thiophene and 2,2-bithiophene on ag(111): a combined near edge extended x-ray absorption fine structure and xα scattered-wave study," *Surface Science*, vol. 452, no. 13, pp. 20 – 32, 2000.

[34] W. Veigele, "Photon cross sections from 0.1 kev to 1 mev for elements z = 1 to z = 94," *Atomic Data and Nuclear Data Tables*, vol. 5, no. 1, pp. 51 – 111, 1973.

[35] B. Henke, P. Lee, T. Tanaka, R. Shimabukuro, and B. Fujikawa, "Low-energy x-ray interaction coefficients: Photoabsorption, scattering, and reflection: E = 1002000 ev z = 194," *Atomic Data and Nuclear Data Tables*, vol. 27, no. 1, pp. 1 – 144, 1982.

[36] R. Jones and D. Woodruff, "Sampling depths in total yield and reflectivity {SEXAFS} studies in the soft x-ray region," *Surface Science*, vol. 114, no. 1, pp. 38 – 46, 1982.

[37] E. J. Mele and J. J. Ritsko, "Fermi-level lowering and the core exciton spectrum of intercalated graphite," *Phys. Rev. Lett.*, vol. 43, pp. 68–71, Jul 1979.

[38] B. Watts and H. Ade, "A simple method for determining linear polarization and energy calibration of focused soft x-ray beams," *Journal of Electron Spectroscopy and Related Phenomena*, vol. 162, no. 2, pp. 49 – 55, 2008.

[39] R. N. Sodhi and C. Brion, "Reference energies for inner shell electron energy-loss spectroscopy," *Journal of Electron Spectroscopy and Related Phenomena*, vol. 34, no. 4, pp. 363 – 372, 1984.

[40] C. T. Chen, N. V. Smith, and F. Sette, "Exchange, spin-orbit, and correlation effects in the soft-x-ray magnetic-circular-dichroism spectrum of nickel," *Phys. Rev. B*, vol. 43, pp. 6785–6787, Mar 1991.

[41] P. S. Johnson, P. L. Cook, I. Zegkinoglou, J. M. García-Lastra, A. Rubio, R. E. Ruther, R. J. Hamers, and F. J. Himpsel, "Electronic structure of fe- vs. ru-based dye molecules," *The Journal of Chemical Physics*, vol. 138, no. 4, pp. –, 2013.

[42] M. Grätzel, "Photoelectrochemical cells," *Nature*, vol. 414, no. 6861, pp. 338–344, 2001.

[43] G. Bauer and K. A. Kirchner, "Well-defined bifunctional iron catalysts for the hydrogenation of ketones: Iron, the new ruthenium," *Angewandte Chemie International Edition*, vol. 50, no. 26, pp. 5798–5800, 2011.

[44] M. G. Walter, A. B. Rudine, and C. C. Wamser, "Porphyrins and phthalocyanines in solar photovoltaic cells," *Journal of Porphyrins and Phthalocyanines*, vol. 14, no. 09, pp. 759–792, 2010.

[45] A. Hagfeldt and M. Grätzel, "Molecular photovoltaics," *Accounts of Chemical Research*, vol. 33, no. 5, pp. 269–277, 2000.

[46] P. L. Cook, W. Yang, X. Liu, J. M. García-Lastra, A. Rubio, and F. J. Himpsel, "Unoccupied states in cu and zn octaethyl-porphyrin and phthalocyanine," *The Journal of Chemical Physics*, vol. 134, no. 20, p. 204707, 2011.

[47] J. Åhlund, K. Nilson, J. Schiessling, L. Kjeldgaard, S. Berner, N. Mårtensson, C. Puglia, B. Brena, M. Nyberg, and Y. Luo, "The electronic structure of iron phthalocyanine probed by photoelectron and x-ray absorption spectroscopies and density functional theory calculations," *The Journal of Chemical Physics*, vol. 125, no. 3, p. 034709, 2006.

[48] M. P. de Jong, R. Friedlein, S. L. Sorensen, G. Öhrwall, W. Osikowicz, C. Tengsted, S. K. M. Jönsson, M. Fahlman, and W. R. Salaneck, "Orbital-specific dynamic charge transfer from fe(ii)-tetraphenylporphyrin molecules to molybdenum disulfide substrates," *Phys. Rev. B*, vol. 72, p. 035448, Jul 2005.

[49] M.-S. Liao and S. Scheiner, "Electronic structure and bonding in metal phthalocyanines, metal=fe, co, ni, cu, zn, mg," *The Journal of Chemical Physics*, vol. 114, no. 22, pp. 9780–9791, 2001.

[50] E. M. J. Johansson, M. Odelius, S. Plogmaker, M. Gorgoi, S. Svensson, H. Siegbahn, and H. Rensmo, "Spinorbit coupling and metalligand interactions in fe(ii), ru(ii), and os(ii) complexes," *The Journal of Physical Chemistry C*, vol. 114, no. 22, pp. 10314–10322, 2010.

[51] E. Johansson, M. Odelius, M. Gorgoi, O. Karis, R. Ovsyannikov, F. Schäfers, S. Svensson, H. Siegbahn, and H. Rensmo, "Valence electronic structure of ruthenium based complexes probed by photoelectron spectroscopy at high kinetic energy (hike) and modeled by dft calculations," *Chemical Physics Letters*, vol. 464, no. 46, pp. 192 – 197, 2008.

[52] G. Liu, A. Klein, A. Thissen, and W. Jaegermann, "Electronic properties and interface characterization of phthalocyanine and ru-polypyridine dyes on tio2 surface," *Surface Science*, vol. 539, no. 13, pp. 37 – 48, 2003.

[53] K. Westermark, H. Rensmo, J. Schnadt, P. Persson, S. Södergren, P. Brühwiler, S. Lunell, and H. Siegbahn, "Electron dynamics within ru-2,2-bipyridine complexesan n1s core level excitation study," *Chemical Physics*, vol. 285, no. 1, pp. 167 – 176, 2002.

[54] H. Rensmo, K. Westermark, S. Södergren, O. Kohle, P. Persson, S. Lunell, and H. Siegbahn, "Xps studies of ru-polypyridine complexes for solar cell applications," *The Journal of Chemical Physics*, vol. 111, no. 6, pp. 2744–2750, 1999.

[55] R. J. Crutchley and A. B. P. Lever, "Comparative chemistry of bipyrazyl and bipyridyl metal complexes: spectroscopy, electrochemistry and photoanation," *Inorganic Chemistry*, vol. 21, no. 6, pp. 2276–2282, 1982.

[56] G. Benkö, P. Myllyperkiö, J. Pan, A. P. Yartsev, and V. Sundström, "Photoinduced electron injection from ru(dcbpy)$_2$(ncs)$_2$ to sno$_2$ and tio$_2$ nanocrystalline films," *Journal of the American Chemical Society*, vol. 125, no. 5, pp. 1118–1119, 2003.

[57] P.-S. Kim, T.-K. Sham, P. Zhang, M.-K. Fung, S.-T. Lee, Y.-F. Hu, and B. W. Yates, "X-ray excited optical luminescence studies of tris-(2,2-bipyridine)ruthenium(ii) at the c, n k-edge and ru l_3, 2-edge," *Journal of the American Chemical Society*, vol. 123, no. 36, pp. 8870–8871, 2001.

[58] A. T. Yeh, C. V. Shank, and J. K. McCusker, "Ultrafast electron localization dynamics following photo-induced charge transfer," *Science*, vol. 289, no. 5481, pp. 935–938, 2000.

[59] N. H. Damrauer, G. Cerullo, A. Yeh, T. R. Boussie, C. V. Shank, and J. K. McCusker, "Femtosecond dynamics of excited-state evolution in [ru(bpy$_3$]^2+," *Science*, vol. 275, no. 5296, pp. 54–57, 1997.

[60] Y. Tachibana, J. E. Moser, M. Grätzel, D. R. Klug, and J. R. Durrant, "Subpicosecond interfacial charge separation in dye-sensitized nanocrystalline titanium dioxide films," *The Journal of Physical Chemistry*, vol. 100, no. 51, pp. 20056–20062, 1996.

[61] C. Bressler, C. Milne, V.-T. Pham, A. ElNahhas, R. M. van der Veen, W. Gawelda, S. Johnson, P. Beaud, D. Grolimund, M. Kaiser, C. N. Borca, G. Ingold, R. Abela, and M. Chergui, "Femtosecond xanes study of the light-induced spin crossover dynamics in an iron(ii) complex," *Science*, vol. 323, no. 5913, pp. 489–492, 2009.

[62] W. Gawelda, M. Johnson, F. M. F. de Groot, R. Abela, C. Bressler, and M. Chergui, "Electronic and molecular structure of photoexcited [ruii(bpy$_3$]^2+ probed by picosecond x-ray absorption spectroscopy," *Journal of the American Chemical Society*, vol. 128, no. 15, pp. 5001–5009, 2006.

[63] N. Huse, H. Cho, K. Hong, L. Jamula, F. M. F. de Groot, T. K. Kim, J. K. McCusker, and R. W. Schoenlein, "Femtosecond soft x-ray spectroscopy of solvated transition-metal complexes: Deciphering the interplay of electronic and structural dynamics," *The Journal of Physical Chemistry Letters*, vol. 2, no. 8, pp. 880–884, 2011.

[64] N. Huse, T. K. Kim, L. Jamula, J. K. McCusker, F. M. F. de Groot, and R. W. Schoenlein, "Photo-induced spin-state conversion in solvated transition metal complexes probed via time-resolved soft x-ray spectroscopy," *Journal of the American Chemical Society*, vol. 132, no. 19, pp. 6809–6816, 2010.

[65] L. X. Chen, "Probing transient molecular structures in photochemical processes using laser-initiated time-resolved x-ray absorption spectroscopy," *Annual Review of Physical Chemistry*, vol. 56, no. 1, pp. 221–254, 2005.

[66] G. Ma, J. He, C.-H. Kang, and S.-H. Tang, "Excited state dynamics studies of iron(iii) phthalocyanine using femtosecond pumpprobe techniques," *Chemical Physics Letters*, vol. 370, no. 12, pp. 293 – 299, 2003.

[67] J. Schnadt, P. A. Brühwiler, L. Patthey, J. N. O'Shea, S. Södergren, M. Odelius, R. Ahuja, O. Karis, M. Bässler, P. Persson, H. Siegbahn, S. Lunell, and N. Mårtensson, "Experimental evidence for sub-3-fs charge transfer from an aromatic adsorbate to a semiconductor," *Nature*, vol. 418, pp. 620–623, 2002.

[68] E. F. Aziz, M. H. Rittmann-Frank, K. M. Lange, S. Bonhommeau, and M. Chergui, "Charge transfer to solvent identified using dark channel fluorescence-yield l-edge spectroscopy," *Nature Chemistry*, vol. 2, pp. 853–857, 2010.

[69] R. K. Hocking, E. C. Wasinger, Y.-L. Yan, F. M. F. deGroot, F. A. Walker, K. O. Hodgson, B. Hedman, and E. I. Solomon, "Fe l-edge x-ray absorption spectroscopy of low-spin heme relative to non-heme fe complexes:? delocalization of fe d-electrons into the porphyrin ligand," *Journal of the American Chemical Society*, vol. 129, no. 1, pp. 113–125, 2007.

[70] M. Abrahamsson, M. Jäger, R. J. Kumar, T. Österman, P. Persson, H.-C. Becker, O. Johansson, and L. Hammarström, "Bistridentate ruthenium(ii)polypyridyl-type complexes with microsecond ^{3}mlct state lifetimes: Sensitizers for rod-like molecular arrays," *Journal of the American Chemical Society*, vol. 130, no. 46, pp. 15533–15542, 2008.

[71] F. De Angelis, S. Fantacci, A. Selloni, M. K. Nazeeruddin, and M. Grätzel, "Time-dependent density functional theory investigations on the excited states of ru(ii)-dye-sensitized tio_2 nanoparticles: the role of sensitizer protonation," *Journal of the American Chemical Society*, vol. 129, no. 46, pp. 14156–14157, 2007.

[72] A. Vlček Jr. and S. Záliš, "Modeling of charge-transfer transitions and excited states in d6 transition metal complexes by dft techniques," *Coordination Chemistry Reviews*, vol. 251, no. 34, pp. 258 – 287, 2007.

[73] P. Persson and M. J. Lundqvist, "Calculated structural and electronic interactions of the ruthenium dye n3 with a titanium dioxide nanocrystal," *The Journal of Physical Chemistry B*, vol. 109, no. 24, pp. 11918–11924, 2005.

[74] J.-F. Guillemoles, V. Barone, L. Joubert, and C. Adamo, "A theoretical investigation of the ground and excited states of selected ru and os polypyridyl molecular dyes," *The Journal of Physical Chemistry A*, vol. 106, no. 46, pp. 11354–11360, 2002.

[75] S. Gorelsky, E. Dodsworth, A. Lever, and A. Vlcek, "Trends in metalligand orbital mixing in generic series of ruthenium n-donor ligand complexeseffect on electronic

spectra and redox properties," *Coordination Chemistry Reviews*, vol. 174, no. 1, pp. 469 – 494, 1998.

[76] G. Calzaferri and R. Rytz, "Electronic transition oscillator strength by the extended hueckel molecular orbital method," *The Journal of Physical Chemistry*, vol. 99, no. 32, pp. 12141–12150, 1995.

[77] A. B. P. Lever, "Electrochemical parametrization of metal complex redox potentials, using the ruthenium(iii)/ruthenium(ii) couple to generate a ligand electrochemical series," *Inorganic Chemistry*, vol. 29, no. 6, pp. 1271–1285, 1990.

[78] M. Král, "The ligand-ligand and spin-orbit interactions in fe$(phen)_3^{+2}$ and ru$(phen)_{+2}^3$ ions," *Theoretica chimica acta*, vol. 55, pp. 333–336, 1980.

[79] K. S. Low, J. M. Cole, X. Zhou, and N. Yufa, "Rationalizing the molecular origins of ru- and fe-based dyes for dye-sensitized solar cells," *Acta Crystallographica Section B*, vol. 68, no. 2, pp. 137–149, 2012.

[80] B. N. Figgis and M. A. Hitchman, *Ligand field theory and its applications*.

[81] M. Blume, A. J. Freeman, and R. E. Watson, "Theory of spin-orbit coupling in atoms. iii," *Phys. Rev.*, vol. 134, pp. A320–A327, Apr 1964.

[82] M. Blume and R. E. Watson, "Theory of spin-orbit coupling in atoms. ii. comparison of theory with experiment," *Proceedings of the Royal Society of London. Series A. Mathematical and Physical Sciences*, vol. 271, no. 1347, pp. 565–578, 1963.

[83] M. Srnec, J. Chalupský, M. Fojta, L. Zendlová, L. Havran, M. Hocek, M. Kývala, and L. Rulíšek, "Effect of spinorbit coupling on reduction potentials of octahedral ruthenium(ii/iii) and osmium(ii/iii) complexes," *Journal of the American Chemical Society*, vol. 130, no. 33, pp. 10947–10954, 2008.

[84] F. Felix, J. Ferguson, H. U. Guedel, and A. Ludi, "The electronic spectrum of tris(2,2'-bipyridine)ruthenium^2+," *Journal of the American Chemical Society*, vol. 102, no. 12, pp. 4096–4102, 1980.

[85] S. Decurtins, F. Felix, J. Ferguson, H. U. Guedel, and A. Ludi, "The electronic spectrum of tris(2,2'-bipyridine)iron^2+ and tris (2,2'-bipyridine)osmium^2+," *Journal of the American Chemical Society*, vol. 102, no. 12, pp. 4102–4106, 1980.

[86] M. K. R. Fischer, I. Lopez-Duarte, M. M. Wienk, M. V. Martinez-Díaz, R. A. J. Janssen, P. Bäuerle, and T. Torres, "Functionalized dendritic oligothiophenes: Ruthenium phthalocyanine complexes and their application in bulk heterojunction solar cells," *Journal of the American Chemical Society*, vol. 131, no. 24, pp. 8669–8676, 2009.

[87] P. L. Cook, P. S. Johnson, X. Liu, A.-L. Chin, and F. J. Himpsel, "Radiation damage in biomimetic dye molecules for solar cells," *The Journal of Chemical Physics*, vol. 131, no. 21, p. 214702, 2009.

[88] P. L. Cook *et al.* to be submitted for publication.

[89] F. Himpsel, P. Cook, G. de la Torre, J. García-Lastra, R. Gonzalez-Moreno, J.-H. Guo, R. Hamers, C. Kronawitter, P. Johnson, J. Ortega, D. Pickup, M.-E. Ragoussi, C. Rogero, A. Rubio, R. Ruther, L. Vayssieres, W. Yang, and I. Zegkinoglou, "Design of solar cell materials via soft x-ray spectroscopy," *Journal of Electron Spectroscopy and Related Phenomena*, 2012.

[90] G. te Velde, F. M. Bickelhaupt, E. J. Baerends, C. Fonseca Guerra, S. J. A. van Gisbergen, J. G. Snijders, and T. Ziegler, "Chemistry with adf," *Journal of Computational Chemistry*, vol. 22, no. 9, pp. 931–967, 2001.

[91] S. H. Vosko, L. Wilk, and M. Nusair, "Accurate spin-dependent electron liquid correlation energies for local spin density calculations: a critical analysis," *Canadian Journal of Physics*, vol. 58, no. 8, pp. 1200–1211, 1980.

[92] T. Kowalczyk, S. R. Yost, and T. V. Voorhis, "Assessment of the delta scf density functional theory approach for electronic excitations in organic dyes," *The Journal of Chemical Physics*, vol. 134, no. 5, p. 054128, 2011.

[93] J. I. Rodríguez, R. F. Bader, P. W. Ayers, C. Michel, A. W. Götz, and C. Bo, "A high performance grid-based algorithm for computing qtaim properties," *Chemical Physics Letters*, vol. 472, no. 13, pp. 149 – 152, 2009.

[94] E. Stavitski and F. M. de Groot, "The ctm4xas program for eels and xas spectral shape analysis of transition metal l edges," *Micron*, vol. 41, no. 7, pp. 687 – 694, 2010.

[95] P. S. Johnson, J. M. García-Lastra, C. K. Kennedy, N. J. Jersett, I. Boukahil, F. J. Himpsel, and P. L. Cook, "Crystal fields of porphyrins and phthalocyanines

from polarization-dependent 2p-to-3d multiplets," *The Journal of Chemical Physics*, vol. 140, no. 11, pp. –, 2014.

[96] P. L. Cook, X. Liu, W. Yang, and F. J. Himpsel, "X-ray absorption spectroscopy of biomimetic dye molecules for solar cells," *The Journal of Chemical Physics*, vol. 131, no. 19, pp. –, 2009.

[97] D. F. Pickup, I. Zegkinoglou, B. Ballesteros, C. R. Ganivet, J. M. García-Lastra, P. L. Cook, P. S. Johnson, C. Rogero, F. de Groot, A. Rubio, G. de la Torre, J. E. Ortega, and F. J. Himpsel, "Influence of axial and peripheral ligands on the electronic structure of titanium phthalocyanines," *The Journal of Physical Chemistry C*, vol. 117, no. 9, pp. 4410–4420, 2013.

[98] I. Zegkinoglou, M.-E. Ragoussi, C. D. Pemmaraju, P. S. Johnson, D. F. Pickup, J. E. Ortega, D. Prendergast, G. de la Torre, and F. J. Himpsel, "Spectroscopy of donor-acceptor porphyrins for dye-sensitized solar cells," *The Journal of Physical Chemistry C*, vol. 117, no. 26, pp. 13357–13364, 2013.

[99] K. Simonov, A. Vinogradov, M. Brzhezinskaya, A. Preobrajenski, A. Generalov, and A. Klyushin, "Features of metal atom 2p excitations and electronic structure of 3d-metal phthalocyanines studied by x-ray absorption and resonant photoemission," *Applied Surface Science*, vol. 267, no. 0, pp. 132 – 135, 2013.

[100] T. Kroll, R. Kraus, R. Schönfelder, V. Y. Aristov, O. V. Molodtsova, P. Hoffmann, and M. Knupfer, "Transition metal phthalocyanines: Insight into the electronic structure from soft x-ray spectroscopy," *The Journal of Chemical Physics*, vol. 137, no. 5, pp. –, 2012.

[101] M. L. M. Rocco, K.-H. Frank, P. Yannoulis, and E.-E. Koch, "Unoccupied electronic structure of phthalocyanine films," *The Journal of Chemical Physics*, vol. 93, no. 9, pp. 6859–6864, 1990.

[102] P. S. Miedema, M. M. van Schooneveld, R. Bogerd, T. C. R. Rocha, M. Hävecker, A. Knop-Gericke, and F. M. F. de Groot, "Oxygen binding to cobalt and iron phthalocyanines as determined from in situ x-ray absorption spectroscopy," *The Journal of Physical Chemistry C*, vol. 115, no. 51, pp. 25422–25428, 2011.

[103] S. Stepanow, P. S. Miedema, A. Mugarza, G. Ceballos, P. Moras, J. C. Cezar, C. Carbone, F. M. F. de Groot, and P. Gambardella, "Mixed-valence behavior and strong

correlation effects of metal phthalocyanines adsorbed on metals," *Phys. Rev. B*, vol. 83, p. 220401, Jun 2011.

[104] S. Ahmadi, M. N. Shariati, S. Yu, and M. Göthelid, "Molecular layers of znpc and fepc on au(111) surface: Charge transfer and chemical interaction," *The Journal of Chemical Physics*, vol. 137, no. 8, pp. –, 2012.

[105] M. G. Betti, P. Gargiani, R. Frisenda, R. Biagi, A. Cossaro, A. Verdini, L. Floreano, and C. Mariani, "Localized and dispersive electronic states at ordered fepc and copc chains on au(110)," *The Journal of Physical Chemistry C*, vol. 114, no. 49, pp. 21638–21644, 2010.

[106] F. Petraki, H. Peisert, F. Latteyer, U. Aygül, A. Vollmer, and T. Chassé, "Impact of the 3d electronic states of cobalt and manganese phthalocyanines on the electronic structure at the interface to ag(111)," *The Journal of Physical Chemistry C*, vol. 115, no. 43, pp. 21334–21340, 2011.

[107] F. M. F. de Groot, J. C. Fuggle, B. T. Thole, and G. A. Sawatzky, "2p x-ray absorption of 3d transition-metal compounds: An atomic multiplet description including the crystal field," *Phys. Rev. B*, vol. 42, pp. 5459–5468, Sep 1990.

[108] M. M. Grush, J. Chen, T. L. Stemmler, S. J. George, C. Y. Ralston, R. T. Stibrany, A. Gelasco, G. Christou, S. M. Gorun, J. E. Penner-Hahn, and S. P. Cramer, "Manganese l-edge x-ray absorption spectroscopy of manganese catalase from lactobacillus plantarum and mixed valence manganese complexes," *Journal of the American Chemical Society*, vol. 118, no. 1, pp. 65–69, 1996.

[109] M. Grobosch, B. Mahns, C. Loose, R. Friedrich, C. Schmidt, J. Kortus, and M. Knupfer, "Identification of the electronic states of manganese phthalocyanine close to the fermi level," *Chemical Physics Letters*, vol. 505, no. 46, pp. 122 – 125, 2011.

[110] P. S. Miedema, S. Stepanow, P. Gambardella, and F. M. F. de Groot, "2p x-ray absorption of iron-phthalocyanine," *Journal of Physics: Conference Series*, vol. 190, no. 1, p. 012143, 2009.

[111] P. S. Miedema and F. M. de Groot, "The iron l edges: Fe 2p x-ray absorption and electron energy loss spectroscopy," *Journal of Electron Spectroscopy and Related Phenomena*, vol. 187, no. 0, pp. 32 – 48, 2013.

[112] B. Thole, G. V. D. Laan, and P. Butler, "Spin-mixed ground state of fe phthalocyanine and the temperature-dependent branching ratio in x-ray absorption spectroscopy," *Chemical Physics Letters*, vol. 149, no. 3, pp. 295 – 299, 1988.

[113] K. Nakamura, Y. Kitaoka, T. Akiyama, T. Ito, M. Weinert, and A. J. Freeman, "Constraint density functional calculations for multiplets in a ligand-field applied to fe-phthalocyanine," *Phys. Rev. B*, vol. 85, p. 235129, Jun 2012.

[114] F. Petraki, H. Peisert, U. Aygl, F. Latteyer, J. Uihlein, A. Vollmer, and T. Chassé, "Electronic structure of fepc and interface properties on ag(111) and au(100)," *The Journal of Physical Chemistry C*, vol. 116, no. 20, pp. 11110–11116, 2012.

[115] M. D. Kuz'min, A. Savoyant, and R. Hayn, "Ligand field parameters and the ground state of fe(ii) phthalocyanine," *The Journal of Chemical Physics*, vol. 138, no. 24, pp. –, 2013.

[116] K. Baberschke, "Magnetic switching of fe-porphyrin molecules adsorbed on surfaces: An xafs and xmcd study," *Journal of Physics: Conference Series*, vol. 190, no. 1, p. 012012, 2009.

[117] A. Labarta, E. Molins, X. Viñas, J. Tejada, A. Caubet, and S. Alvarez, "Electronic structure determination of iron(ii) phthalocyanine via magnetic susceptibility and mssbauer measurements," *The Journal of Chemical Physics*, vol. 80, no. 1, pp. 444–448, 1984.

[118] T. Kroll, V. Y. Aristov, O. V. Molodtsova, Y. A. Ossipyan, D. V. Vyalikh, B. Buchner, and M. Knupfer, "Spin and orbital ground state of co in cobalt phthalocyanine," *The Journal of Physical Chemistry A*, vol. 113, no. 31, pp. 8917–8922, 2009. PMID: 19588993.

[119] S. Krasnikov, A. Preobrajenski, N. Sergeeva, M. Brzhezinskaya, M. Nesterov, A. Cafolla, M. Senge, and A. Vinogradov, "Electronic structure of ni(ii) porphyrins and phthalocyanine studied by soft x-ray absorption spectroscopy," *Chemical Physics*, vol. 332, no. 23, pp. 318 – 324, 2007.

[120] S. Stepanow, A. Mugarza, G. Ceballos, P. Moras, J. C. Cezar, C. Carbone, and P. Gambardella, "Giant spin and orbital moment anisotropies of a cu-phthalocyanine monolayer," *Phys. Rev. B*, vol. 82, p. 014405, Jul 2010.

[121] W. Chen, H. Huang, S. Chen, X. Y. Gao, and A. T. S. Wee, "Low-temperature scanning tunneling microscopy and near-edge x-ray absorption fine structure investigations of molecular orientation of copper(ii) phthalocyanine thin films at organic heterojunction interfaces," *The Journal of Physical Chemistry C*, vol. 112, no. 13, pp. 5036–5042, 2008.

[122] K. A. Nguyen and R. Pachter, "Jahnteller triplet excited state structures and spectra of zinc complexes of porphyrin and phthalocyanine: A density functional theory study," *The Journal of Chemical Physics*, vol. 118, no. 13, 2003.

[123] Y. Zhang, T. Learmonth, S. Wang, A. Y. Matsuura, J. Downes, L. Plucinski, S. Bernardis, C. O'Donnell, and K. E. Smith, "Electronic structure of the organic semiconductor vanadyl phthalocyanine (vo-pc)," *J. Mater. Chem.*, vol. 17, pp. 1276–1283, 2007.

[124] Y. Zhang, S. Wang, T. Learmonth, L. Plucinski, A. Matsuura, S. Bernardis, C. ODonnell, J. E. Downes, and K. E. Smith, "Electronic excitations in vanadium oxide phthalocyanine studied via resonant soft x-ray emission and resonant inelastic x-ray scattering," *Chemical Physics Letters*, vol. 413, no. 13, pp. 95 – 99, 2005.

[125] J. Mack and M. J. Stillman, vol. 16, ch. 103, pp. 44–116. Elsevier Science, 2003.

[126] M. Atanasov, C. A. Daul, M.-M. Rohmer, and T. Venkatachalam, "A {DFT} based ligand field study of the {EPR} spectra of co(ii) and cu(ii) porphyrins," *Chemical Physics Letters*, vol. 427, no. 46, pp. 449 – 454, 2006.

[127] M. J. Stillman and A. J. Thomson, "Assignment of the charge-transfer bands in some metal phthalocyanines. evidence for the s= 1 state of iron (ii) phthalocyanine in solution," *J. Chem. Soc., Faraday Trans. 2*, vol. 70, pp. 790–804, 1974.

[128] F. de Groot, "Multiplet effects in x-ray spectroscopy," *Coordination Chemistry Reviews*, vol. 249, no. 12, pp. 31 – 63, 2005.

[129] H. Ikeno, F. M. F. de Groot, E. Stavitski, and I. Tanaka, "Multiplet calculations of l 2,3 x-ray absorption near-edge structures for 3d transition-metal compounds," *Journal of Physics: Condensed Matter*, vol. 21, no. 10, p. 104208, 2009.

[130] H. Peisert, I. Biswas, M. Knupfer, and T. Chassé, "Orientation and electronic properties of phthalocyanines on polycrystalline substrates," *Physica Status Solidi B*, vol. 246, no. 7, pp. 1529–1545, 2009.

[131] R. De Francesco, M. Stener, and G. Fronzoni, "Theoretical study of near-edge x-ray absorption fine structure spectra of metal phthalocyanines at c and n k-edges," *The Journal of Physical Chemistry A*, vol. 116, no. 11, pp. 2885–2894, 2012.

[132] J. P. Perdew, K. Burke, and M. Ernzerhof, "Generalized gradient approximation made simple," *Phys. Rev. Lett.*, vol. 77, pp. 3865–3868, Oct 1996.

[133] A. Trueba, P. Garcia-Fernandez, J. M. García-Lastra, J. A. Aramburu, M. T. Barriuso, and M. Moreno, "Spectrochemical series and the dependence of racah and 10dq parameters on the metalligand distance: Microscopic origin," *The Journal of Physical Chemistry A*, vol. 115, no. 8, pp. 1423–1432, 2011.

[134] J. M. García-Lastra, J. Y. Buzaré, M. T. Barriuso, J. A. Aramburu, and M. Moreno, "3*d* impurities in normal and inverted perovskites: Differences are not explained by ligand field theory," *Phys. Rev. B*, vol. 75, p. 155101, Apr 2007.

[135] R. D. Cowan, *The Theory of Atomic Structure and Spectra*. University of California Press: Berkeley, CA, 1981.

[136] P. H. Butler, *Point Group Symmetry, Applications, Methods and Tables*. Plenum Press: New York, 1981.

[137] H. Ogasawara, A. Kotani, K. Okada, and B. T. Thole, "Theory of x-ray-absorption spectra in pro_2 and some other rare-earth compounds," *Phys. Rev. B*, vol. 43, pp. 854–859, Jan 1991.

[138] S. P. Cramer, F. M. F. DeGroot, Y. Ma, C. T. Chen, F. Sette, C. A. Kipke, D. M. Eichhorn, M. K. Chan, and W. H. a. Armstrong, "Ligand field strengths and oxidation states from manganese l-edge spectroscopy," *Journal of the American Chemical Society*, vol. 113, no. 21, pp. 7937–7940, 1991.

[139] O. Gunnarson, O. K. Andersen, O. Jepsen, and J. Zaanen, vol. 81 of *Springer Series in Solid-State Sciences*, pp. 82–98. Springer-Verlag, 1988.

[140] B. Gilbert, B. H. Frazer, A. Belz, P. G. Conrad, K. H. Nealson, D. Haskel, J. C. Lang, G. Srajer, and G. De Stasio, "Multiple scattering calculations of bonding and x-ray absorption spectroscopy of manganese oxides," *The Journal of Physical Chemistry A*, vol. 107, no. 16, pp. 2839–2847, 2003.

[141] P. S. Johnson, C. Huang, M. Kim, N. S. Safron, M. S. Arnold, B. M. Wong, P. Gopalan, and F. J. Himpsel, "Orientation of a monolayer of dipolar molecules on graphene from x-ray absorption spectroscopy," *Langmuir*, vol. 30, no. 9, pp. 2559–2565, 2014.